

## 21<sup>st</sup> International IGTE Symposium

on Computational Methods in Electrical Engineering and Multiphysics



## **Proceedings**

Sept. 15 - 18, 2024 Hotel Novapark, Graz, Austria

Alice Reinbacher-Köstinger (editor)

Institute for Fundamentals and Theory in Electrical Engineering



The 21<sup>st</sup> International IGTE Symposium on Computational Methods in Electrical Engineering and Multiphysics was sponsored and supported by:



















### **Imprint**

Organisation: Christian Magele, Alice Reinbacher-Köstinger and Thomas Bauernfeind

Graz University of Technology, Institute of Fundamentals and Theory in

Electrical Engineering (IGTE)

Editor: Alice Reinbacher-Köstinger

Layout: Eniz Mušeljić

Cover: Alice Reinbacher-Köstinger

2025 Verlag der Technischen Universität Graz

www.tugraz-verlag.at

Proceedings of the 21<sup>st</sup> International IGTE Symposium on Computational Methods in Electrical Engineering and Multiphysics, Graz, Novapark, 15-18.9.2024

ISBN (e-book): 978-3-99161-059-5 DOI: 10.3217/978-3-99161-059-5



This work is licensed under the Creative Commons Attribution 4.0 International (CC BY-NC-ND 4.0) license. https://creativecommons.org/licenses/by-nc-nd/4.0/

This CC license does not apply to the cover, third party material (attributed to other sources) and content noted otherwise

### List of Proceedings

Modeling Cylindrical Ground Non-Homogeneity Influence on Two-electrode Grounding System Characteristics  Jovanovic Dejan, Cvetkovic Nenad, Vuckovic Dragan, Zivaljevic Dragana	4
New Design of a Fast Thomson Drive Actuator Based on Permanent Magnets: Multiphysics Simulation  Baida Yevhen I., Lytvynenko Victoria V., Chepeliuk Oleksandr O., Leliuk Mykola A., Clemens Markus, Pantelyat  Michael G	10
Frequency-Dependent Parameter Sensitivity in Undermoded Reverberation Chambers  Kenderes Anett, Gyimóthy Szabolcs, Benkő Péter Tamás	16
Effect of Physical and Geometric Parameters on Eddy Current Sensor Response  Sedira Dounia, Messaoudene Bouchra, Berkas Kaouter, Ferkha Nassira	22
2D Transient Calculation of the Step Voltage Distribution of a PV Power Plant  Jauk Benjamin, Schürhuber Robert, Friedl Katrin	28
Görges Polygon and Differential Leakage Coefficient of Polyphase Windings – Part 1 – Integer Slot Windings – Schmidt Erich, Lackner David A	33
Görges Polygon and Differential Leakage Coefficient of Polyphase Windings – Part 2 – Fractional Slot Windings – Schmidt Erich, Lackner David A	39
Data driven parameter identification of nonlinear magnetic properties in steel sheets  Mušeljić Eniz, Reinbacher-Köstinger Alice, Gschwentner Andreas, Kaltenbacher Manfred	45
Sequential Bayesian Experimental Design for Efficiency Maps using Gaussian Processes  Reinbacher-Köstinger Alice, Dhakal Pawan Kumar, Heidarikani Kourosh, Mušeljić Eniz, Komann Theodor,  Muetze Annette, Ulbrich Stefan, Kaltenbacher Manfred	50
Finite element modeling of eddy currents in a multiconductor system with quasi-2D symmetry  Bakondi Tamás, Gyimóthy Szabolcs, Bilicz Sándor	56
An air-gap element for the isogeometric space-time simulation of electric machines  Reichelt Michael, Merkel Melina, Schöps Sebastian, Steinbach Olaf	57
An effective interface formulation for electromagnetic shielding using the A-formulation in 3D  Schöbinger Markus, Leumüller Michael, Hollaus Karl	58
Relating transmission line overvoltages and lightning location: a machine learning-based procedure  Barmada Sami, Brignone Massimo, Dodge Shayan, Nicora Martino, Procopio Renato, Tucci Mauro	59
Evaluation of a control-oriented single-phase transformer core model  Schwartze Nicolai, Moschik Sonja, Reichhartinger Markus	60
Computational efficient single component Gibbs sampling for electrical tomography  Neumayer Markus, Suppan Thomas, Bretterklieber Thomas, Wegleiter Hannes, Fox Colin	61
Predicting torque characteristics of synchronous reluctance motors using swin transformer  Nagayama Taisuke, Sasaki Hidenori	62
Effective material modelling for laminated iron cores with an A-formulation and circuit coupling  Hanser Valentin, Schöbinger Markus, Hollaus Karl	63
Emulation of photovoltaic arrays under non-uniform environmental conditions  Dimitrijević Marko, Petronijević Milutin	64
Electrical anisotropy of fascicles in a realistic neck model for phrenic nerve stimulation  Wegert Laureen, Ziolkowski Marek, Hunold Alexander, Lange Irene, Kalla Tim, Haueisen Jens	65
Index of Authors	

## Modeling Cylindrical Ground Non-Homogeneity Influence on Two-electrode Grounding System Characteristics

Dejan B. Jovanovic, Nenad N. Cvetkovic, Dragan D. Vuckovic and Dragana U. Zivaljevic Faculty of Electronic Engineering University of Nis, Nis, 18000, Serbia E-mail: nenad.cvetkovic@elfak.ni.ac.rs

Abstract— Very often, ground non-homogeneity can be approximated as vertical cylinder tube (wells, various tubes, pillar foundation etc.). The procedure for modeling influence of such non-homogeneity on grounding system characteristics is presented in the paper. The method based on Method on Moments and Green's function is applicable for quasi-stationary analysis of the grounding systems which includes electrodes positioned inside and outside of the cylindrical domain. Its application is illustrated applying it on the problem of the grounding system formed from ring ground electrode coaxially placed related to cylindrical non-homogeneity and straight wire electrode which position coincide with the non-homogeneity axis.

Index Terms—Cylinder, Green's function, Grounding, Non-homogeneous media.

#### I. INTRODUCTION

Modeling ground non-homogeneity as cylinder or semi-cylinder placed in surrounding ground can be applied for analysis of various grounding problems (wells, various tubes, pillar foundation, roads etc.) [1]-[3]. This paper deals with influence of the ground non-homogeneity, assumed as homogeneous infinitely long vertical cylinder, on two-electrode grounding system, having one electrode placed at the cylinder axis. The applied procedure is based on using the Green's function [2], [4], as well as a standard application of Method of Moment (MoM) [5] and provides determining the resistance of the grounding system and electric scalar potential distribution. The quasi-stationary approach is applied.

#### II. PROBLEM DESCRIPTION

The two-electrode grounding system formed from straight wire vertical electrode and ring ground electrode is analyzed in the paper, Fig. 1.

Straight wire conductor (labeled with 1) having length d and cross-section radii  $a_1$  ( $a_1 <<< d$ ) is placed along the axis of cylindrical homogeneous domain of specific conductivity  $\sigma_1$ . The ring electrode (labeled with 2) of radii  $a_R$ , and wire cross-section radii  $a_2$  ( $a_2 <<< 2a_R\pi$ ) is placed in surrounding homogeneous domain of specific conductivity  $\sigma_2$ . It is placed parallel to the ground surface at the depth h, coaxially to the cylindrical domain. The electrodes are fed by low frequency currents,  $I_{g1}$  and  $I_{g2}$ , respectively. The corresponding Cartesian (x, y, z) coordinate system is assigned. It is assumed (justified for quasi-stationary approach) that leakage current density per unit length is constant, i.e.

$$I_{\text{leak 1}} = I_{\sigma 1}/d$$
, (for conductor 1) and (1a)

$$I_{\text{leak 2}} = I_{g2} / (2a_R \pi)$$
 (for conductor 2). (1b)

The air conductivity  $\sigma_0$  is assumed to be zero, i.e.  $\sigma_0=0$  .

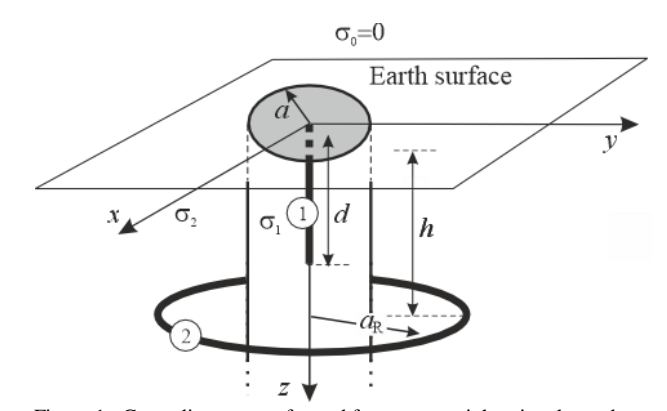


Figure 1: Grounding system formed from one straight wire electrode and ring electrode in the vicinity of cylindrical non-homogeneity.

#### III. GREEN'S FUNCTION

Applied procedure includes Green's function for the potential of the point current source placed inside, i.e. outside infinitely long cylindrically domain. That problem is solved using Laplace, i.e. Poisson equation.

It was realized in [4] (for the inside placed current point source, Fig. 2) and in [1] (for the outside placed current source, Fig. 3) Corresponding forms of Laplace and Poisson equations are

$$\Delta \varphi = -\frac{1}{r\sigma_1} \delta(r - r_0) \delta(\theta - \theta_0) \delta(z - z_0), r < a,$$

$$\Delta \varphi = 0, r > a,$$
(2)

for the point source placed inside non-homogeneity, (Fig. 2), while for the point source outside non-homogeneity (Fig. 3)) is

$$\Delta \varphi = 0, r < a,$$

$$\Delta \varphi = -\frac{1}{r\sigma_2} \delta(r - r_0) \delta(\theta - \theta_0) \delta(z - z_0), r > a.$$
(3)

The solution of differential equations given above, includes modified Bessel functions of first and second kind, which will be explicitly explained in further presentation.

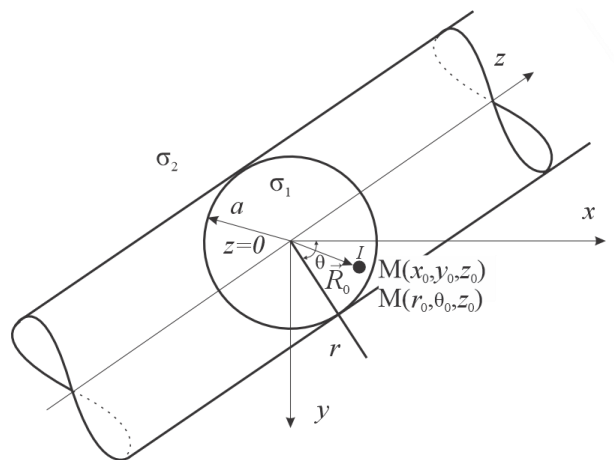


Figure 2: Point current source placed inside infinitely long cylindrically shaped non-homogeneity.

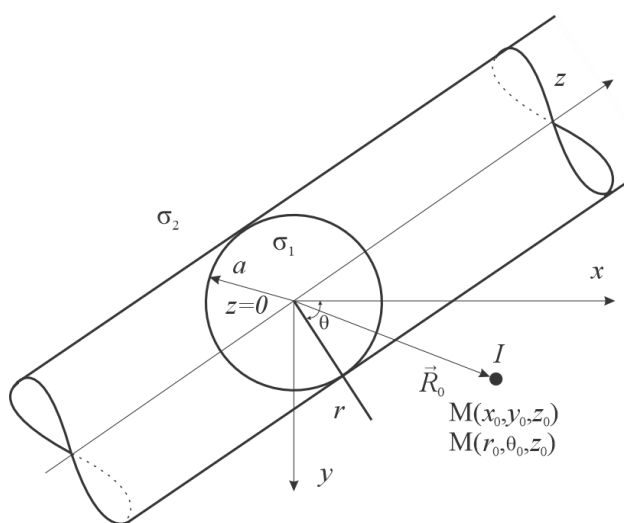


Figure 3: Point current source placed outside infinitely long cylindrically shaped non-homogeneity.

### A. The Current Point Source inside the Cylindrical Domain

The point source of current I placed inside of cylindrical non-homogeneity is observed, Fig. 4. The corresponding Cartesian (x, y, z) and cylindrical coordinate systems  $(r, \theta, z)$  are assigned, where is

$$x = r\cos\theta, y = r\sin\theta, z = z$$
. (2)

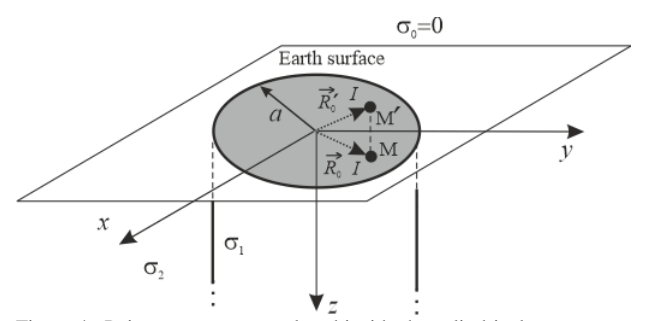


Figure 4: Point current source placed inside the cylindrical non-homogeneity.

As it had been already emphasize, in [4], the Green's function of the point current source placed in infinitely long cylindrically shaped domain is derived solving

Laplace, i.e. Poisson equation. Based on this solution and applying quasi-stationary image theory, it is possible to define potential of the point current source (*I*), placed inside of the cylindrical non-homogeneity from Fig. 4. Image theory application, includes necessity of taking the image source into account. Since for air specific conductivity isv  $\sigma_0 \approx 0$ , the corresponding reflection coefficient  $R_{10}$  is

$$R_{10} = \frac{\sigma_1 - \sigma_0}{\sigma_1 + \sigma_0} \approx 1 \tag{3}$$

and consequently, image point source current is  $R_{10}I \approx I$ .

The positions of the current source (point M) and its image (point M') are defined with field vectors (Fig. 4).

$$\vec{R}_0 = x_0 \hat{x} + y_0 \hat{y} + z_0 \hat{z} = r_0 \hat{r} + z_0 \hat{z}$$
 - point M, i.e. (4a)

$$\vec{R}_0 = x_0 \hat{x} + y_0 \hat{y} - z_0 \hat{z} = r_0 \hat{r} - z_0 \hat{z}$$
 - point M'. (4b)

The observation point is defined by the field vector

$$\vec{R} = x\hat{x} + y\hat{y} + z\hat{z} = r\hat{r} + z\hat{z} . \tag{5}$$

Now, the potential of the point current source from Fig. 2 inside  $(\phi_{11}, r < a)$  and outside  $(\phi_{21}, r > a)$  non-homogeneity, can be expressed as

$$\phi_{11} = \frac{I}{4\pi\sigma_{1}} \frac{1}{\left| \overline{R}_{0} - \overline{R}'_{0} \right|} + \frac{I}{4\pi\sigma_{1}} \frac{1}{\left| \overline{R}_{0} + \overline{R}'_{0} \right|} + \frac{I}{\sigma_{1}\pi^{2}} \sum_{m=0}^{\infty} \left\{ \xi_{m} \cos[m(\phi - \phi_{0})] \times \right\}$$
(6a)

$$\times \int_{0}^{\infty} A_{m}(\lambda) I_{m}(\lambda r) I_{m}(\lambda r_{0}) \cos(\lambda z) \cos(\lambda z_{0}) d\lambda \bigg\}, r < a,$$

and

$$\varphi_{21} = \frac{I}{\sigma_{1}\pi^{2}} \sum_{m=0}^{\infty} \left\{ \xi_{m} \cos[m(\varphi - \varphi_{0})] \times \left\{ \sum_{m=0}^{\infty} B_{m}(\lambda) I_{m}(\lambda r_{0}) K_{m}(\lambda r) \cos(\lambda z) \cos(\lambda z_{0}) d\lambda \right\}, r > a.$$
(6b)

In expressions (6a-b) is  $\xi_0 = 1, \xi_m = 2, m = 1, 2,...$  Based on the boundary conditions for electric field potential and electric flux density, the procedure for determining coefficients  $A_m$  and  $B_m$ , m = 0, 1, 2,... is formed. It is described with following expressions,

$$\Delta_{A_m} = \frac{\sigma_2}{\sigma_1} K'_m(\lambda a) K_m(\lambda a) - K'_m(\lambda a) K_m(\lambda a),$$

$$\Delta_{B_m} = \frac{1}{\lambda a},$$

$$\Delta_m = -\frac{\sigma_2}{\sigma_1} I_m(\lambda a) K'_m(\lambda a) + I'_m(\lambda a) K_m(\lambda a),$$

$$A_m = \frac{\Delta_{A_m}}{\Delta_m}, B_m = \frac{\Delta_{B_m}}{\Delta}.$$
(7)

In previous expressions (7),  $I_m$  and  $K_m$  denote the m-th order modified Bessel functions of the first and second kind, respectively.

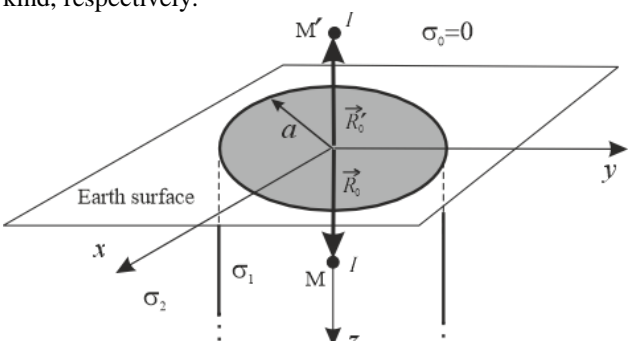


Figure 5: Point current source placed inside the cylindrical non-homogeneity at the *x*-axis.

Since electrode 1 from Fig. 1 is placed along the cylinder axis, for content of this paper, of interest is Green function of the point source placed at *z*-axis of the coordinate system assigned to system from Fig. 4. This particular case is shown in Fig. 5. Now, the positions of the current source (point M) and its image (point M') are defined with field vectors (Fig. 2),

$$\vec{R}_0 = z_0 \hat{z} \text{ (point M)) and}$$
 (8a)

$$\vec{R}_0' = -z_0 \hat{z} \text{ (point M')}. \tag{8b}$$

Now, the potential of the point current source from Fig. 5 inside  $(\varphi_{11}, r < a)$  and outside  $(\varphi_{21}, r > a)$  non-homogeneity, can be expressed as

$$\begin{split} \phi_{11} &= \frac{I}{4\pi\sigma_{1}} \frac{1}{\left|\vec{R} - \vec{R}_{0}\right|} + \frac{I}{4\pi\sigma_{1}} \frac{1}{\left|\vec{R} - \vec{R}_{0}'\right|} + \\ &+ \frac{I}{\sigma_{1}\pi^{2}} \int_{0}^{\infty} A_{0}(\lambda) I_{0}(\lambda r) \left[\cos(\lambda z)\cos(\lambda z_{0})\right] \mathrm{d}\lambda, r < a, \end{split} \tag{9a}$$

and

$$\varphi_{21} = \frac{I}{\sigma_1 \pi^2} \int_0^\infty B_0(\lambda) K_0(\lambda r) \left[ \cos(\lambda z) \cos(\lambda z_0) \right] d\lambda, r > a.$$
 (9b)

The coefficients  $A_0$  and  $B_0$  in (9) now can be determined from the expressions,

$$\begin{split} \Delta_A &= \frac{\sigma_2}{\sigma_1} K_0'(\lambda a) K_0(\lambda a) - K_0'(\lambda a) K_0(\lambda a), \\ \Delta_B &= -I_0(\lambda a) K_0'(\lambda a) + I_0'(\lambda a) K_0(\lambda a) = \frac{1}{\lambda a}, \\ \Delta_0 &= -\frac{\sigma_2}{\sigma_1} I_0(\lambda a) K_0'(\lambda a) + I_0'(\lambda a) K_0(\lambda a), \\ A_0 &= \frac{\Delta_A}{\Delta_0}, B_0 = \frac{\Delta_B}{\Delta_0}. \end{split}$$
 (10)

Labels  $I_m$  and  $K_m$  have been already previously defined as the m-th order modified Bessel functions of the first and second kind, respectively.

Obviously, from expressions (9a-b) one can conclude that potential of the point source from Fig. 5 placed at the

z-axis does not depend on angular coordinate  $\theta$ , which was expected.

Finally, corresponding Green's functions of the poing source placed at *z*-axis of the coordinate system from Fig. 5 can be determined as,

$$G_{i1}(\vec{R}, \vec{R}_0) = \frac{\varphi_{i1}}{I}, i = 1, 2.$$
 (11)

B. The Current Point Source outside the Cylindrical Domain

Analogue to the discussion from previous chapter, the point source of current I placed outside the cylindrical non-homogeneity is observed, Fig. 6. The corresponding Cartesian (x, y, z) and cylindrical coordinate systems  $(r, \theta, z)$  are assigned and connected by relation (2).

As it had been already emphasized in previously presented text, the Green's function of the point current source placed outside infinitely long cylindrically shaped domain is derived solving Laplace, i.e. Poisson equation in [1]. Combining this solution and quasi-stationary image theory the potential of the point current source (I) from Fig. 4 can be determined. As in previous discussion, the corresponding quasi-stationary reflection coefficient  $R_{20}$  is

$$R_{20} = \frac{\sigma_2 - \sigma_0}{\sigma_2 + \sigma_0} \approx 1. \tag{13}$$

Consequently, the image current source is  $R_{20}I \approx I$ .

The positions of the current source (point M) and its image (point M') are defined with field vectors (Fig. 6),

$$\vec{R} = x\hat{x} + y\hat{y} + z\hat{z} = r\hat{r} + z\hat{z}$$
 (point M), i.e. (14a)

$$\vec{R}_0' = x_0 \hat{x} + y_0 \hat{y} - z_0 \hat{z} = r_0 \hat{r} - z_0 \hat{z} \text{ (point M')}.$$
 (14b)

The observation point field vector is defined with (5).

The potential of the point current source from Fig. 6 inside  $(\varphi_{12}, r < a)$  and outside  $(\varphi_{22}, r > a)$  non-homogeneity, can be expressed as

$$\varphi_{12} = \frac{I}{\pi^{2} \sigma_{2}} \left\{ \sum_{m=0}^{\infty} \xi_{m} \cos[m(\theta - \theta_{0})] \times \right. \\
\times \int_{0}^{\infty} A_{m}(\lambda) I_{m}(\lambda r) I_{m}(\lambda r_{0}) \cos(\lambda z) \cos(\lambda z_{0}) d\lambda \right\}, r < a, \tag{15a}$$

and

$$\phi_{22} = \frac{I}{\pi^{2} \sigma_{2}} \left\{ \sum_{m=0}^{\infty} \xi_{m} \cos[m(\theta - \theta_{0})] \times \right.$$

$$\times \int_{0}^{\infty} [B_{m}(\lambda) I_{m}(\lambda r_{0}) K_{m}(\lambda r) + I_{m}(\lambda r) K_{m}(\lambda r_{0})] \times \right.$$

$$\times \left[ \cos(\lambda z) \cos(\lambda z_{0}) \right] d\lambda, r > a. \tag{15b}$$

In expressions (15a-b) is  $\xi_0 = 1, \xi_m = 2, m = 1, 2, \dots$  The coefficients  $A_m$  and  $B_m$ ,  $m = 0, 1, 2, \dots$  in (15) can be determined from the procedure given in [1], derived in the way analogue to that one described in the case of the point source inside cylindrical domain [4]. The expression corresponding to the mentioned procedure are,

$$\Delta_{A_{m}} = \frac{K_{m}(\lambda r_{0})I_{m}(\lambda r_{0})}{\lambda a},$$

$$\Delta_{B_{m}} = I_{m}(\lambda a)I_{m}(\lambda r_{0})I'_{m}(\lambda a)K_{m}(\lambda r_{0})\left(1 - \frac{\sigma_{1}}{\sigma_{2}}\right),$$

$$\Delta = \left[I_{m}(\lambda r_{0})\right]^{2}\left[\frac{\sigma_{1}}{\sigma_{2}}I'_{m}(\lambda a)K_{m}(\lambda a) - I_{m}(\lambda a)K'_{m}(\lambda a)\right],$$

$$A_{m} = \frac{\Delta_{A_{m}}}{\Delta_{m}}, B_{m} = \frac{\Delta_{B_{m}}}{\Delta_{m}}.$$

$$(10)$$

As in (6), in previous expressions (16),  $I_m$  and  $K_m$  denote the m-th order modified Bessel functions of the first and second kind, respectively.

Corresponding Green's functions for the point source from Fig. 6 can be determined as

$$G_{i2}(\vec{R}, \vec{R}_0) = \frac{\Phi_{i2}}{I}, i = 1, 2.$$
 (17)

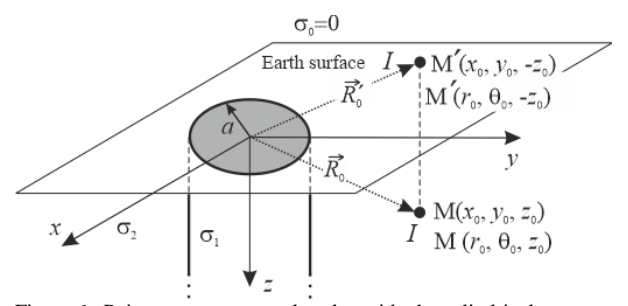


Figure 6: Point current source placed outside the cylindrical non-homogeneity.

#### IV. MOM APPLICATION AND CURRENTS DETERMINING

The current distribution of the system from Fig. 1 can be determined using MoM.

The potential in the vicinity of the grounding system from Fig. 1 can be determined as,

$$\phi_{i}(\vec{R}) = \int_{\text{cond.1}} dI(\vec{R}')G_{i1}(\vec{R}, \vec{R}') + 
+ \oint_{\text{cond.2}} dI(\vec{R}')G_{i2}(\vec{R}, \vec{R}'), i = 1, 2.$$
(18)

In previous expression i=1 defines non-homogeneity, while i=2 corresponds to the surrounding ground, Fig. 1. Field vector  $\vec{R}'$  defines the position of the current element defined at the conductor segment ds' having total leakage current

$$dI(\vec{R}') = I_{leak}(\vec{R}') ds'$$
. (19)

Taking into consideration expressions (1a-b), from expression (18) obtains

$$\phi_{i}(\vec{R}) = \frac{I_{g1}}{d} \int_{\text{cond.1}} G_{i1}(\vec{R}, \vec{R}') \, \mathrm{d} \, s' + 
+ \frac{I_{g2}}{2a_{R}\pi} \oint_{\text{cond.2}} G_{i2}(\vec{R}, \vec{R}') \, \mathrm{d} \, s', i = 1, 2.$$
(20)

Assuming that each electrode surface is approximately equipotential (which is justified for quasi-stationary regime) it is possible to apply MoM and match the values of the potential given by (20) at surface points of conductor 1 ( $\varphi = U_1$ ) and conductor 2 ( $\varphi = U_2$ ). The matching points positions are defined with field vectors  $\vec{R}_1$  (electrode 1) and  $\vec{R}_2$  (electrode 2). Described procedure results in a system of linear equations

$$\begin{split} & \varphi(\vec{R} = \vec{R}_1) \cong U_1 \\ & \varphi(\vec{R} = \vec{R}_2) \cong U_2 \end{split} \tag{21}$$

Solutions of the equation system given above are the fed currents  $I_{\rm g1}$  and  $I_{\rm g2}$ . Knowing their value, it is possible to determine potential of the system from Fig. 1 using expression (20). Also, equation system (21) be expressed in the form

$$U_{1} = R_{11}I_{g1} + R_{12}I_{g2},$$

$$U_{2} = R_{21}I_{g1} + R_{22}I_{g2},$$
(22)

where  $R_{11}$  and  $R_{22}$  are self-resistances of the wire electrode and ring electrode, while  $R_{12}$  and  $R_{21}$  corresponding mutual resistances.

If the electrodes are connected, i.e. they form a unique grounding system, the total grounding resistance can be determined, substituting  $U_1=U_2=U$  in (22), as

$$R_{\rm g} = U/(I_{\rm g1} + I_{\rm g2}) = \frac{R_{11}R_{22} - R_{12}R_{21}}{R_{11} + R_{22} - R_{12} - R_{21}} \ . \tag{23}$$

#### V. NUMERICAL RESULTS

The procedure described in the text above is applied on the system from Fig. 1 for following parameter values chosen based on previous researches [3]. [6], [7]:  $d=1\,\mathrm{m}$ ,  $h=0.7\,\mathrm{m}$ ,  $a=1\,\mathrm{m}$ ,  $a_R=1.5\,\mathrm{m}$ ,  $a_1=0.035\,\mathrm{m}$ ,  $a_2=0.035\,\mathrm{m}$  and  $\sigma_2=0.01\,\mathrm{S/m}$ . The self-, mutual- and total resistance ( $R_{11}$ ,  $R_{22}$ ,  $R_{12}$ ,  $R_{21}$ ,  $R_{g}$ ) of the grounding system from Fig. 1 for different values of ratio  $\sigma_1/\sigma_2$  are given in Tables I, II, III and IV. Dependences of the resistances  $R_{11}$ ,  $R_{22}$ ,  $R_{12}$  and  $R_{g}$  versus ratio  $\sigma_1/\sigma_2$  are shown in Figures 7-10, respectively.

The existing small difference between obtained values for mutual resistances  $R_{12}$  and  $R_{21}$  are the results of approximate character of applied procedure.

TABLE I SELF RESISTANCE  $R_{11}$  VERSUS RATIO  $\sigma_1/\sigma_2$ 

$\sigma_1/\sigma_2$	$R_{11}[\Omega]$
100	7.3799
10	17.038
1	54.056
0.1	381.40
0.01	3641.0

TABLE II  $SELF \ RESISTANCE \ {\it R}_{\rm 22} \ VERSUS \ RATIO \ \sigma_{\rm 1}/\sigma_{\rm 2}$ 

$\sigma_1/\sigma_2$	$R_{22}[\Omega]$
100	6.8226
10	11.329
1	15.129
0.1	15.566
0.01	16.157

 $TABLE~III \\ MUTUAL~RESISTANCES~VERSUS~RATIO~\sigma_1/\sigma_2$ 

$\sigma_1/\sigma_2$	$R_{12}[\Omega]$	$R_{21}[\Omega]$
100	5.9170	5.9217
10	10.8820	10.890
1	14.1280	14.139
0.1	14.8100	14.820
0.01	14.8890	14.880

 $TABLE\ IV$   $Total\ resistance\ versus\ ratio\ \sigma_1/\sigma_2$ 

$\sigma_1/\sigma_2$	$R_{ m g}\left[\Omega ight]$
100	7.1677
10	14.265
1	19.994
0.1	21.530
0.01	21.725



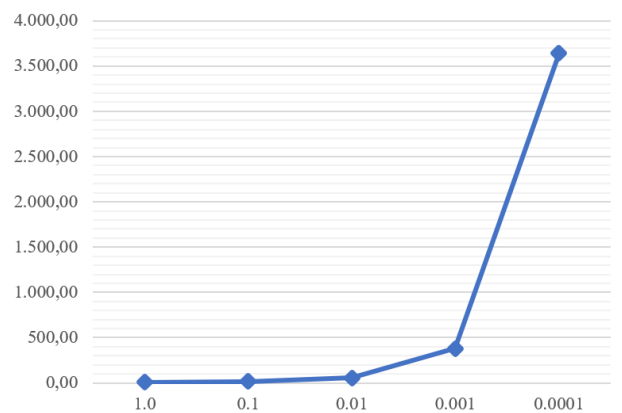


Figure 7: Self resistance  $R_{11}$  of the system from Fig. 1 versus ratio  $\sigma_1/\sigma_2$ .

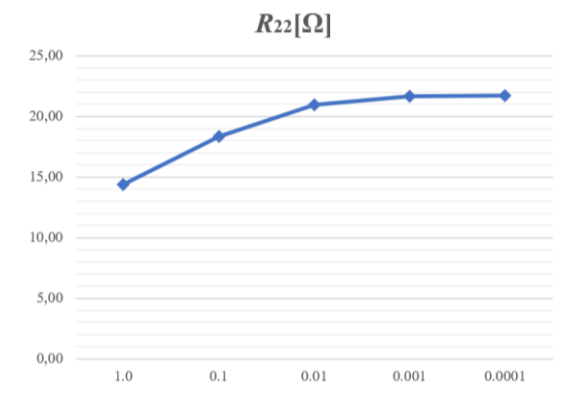


Figure 8: Self resistance  $R_{22}$  of the system from Fig. 1 versus ratio  $\sigma_1/\sigma_2$ .

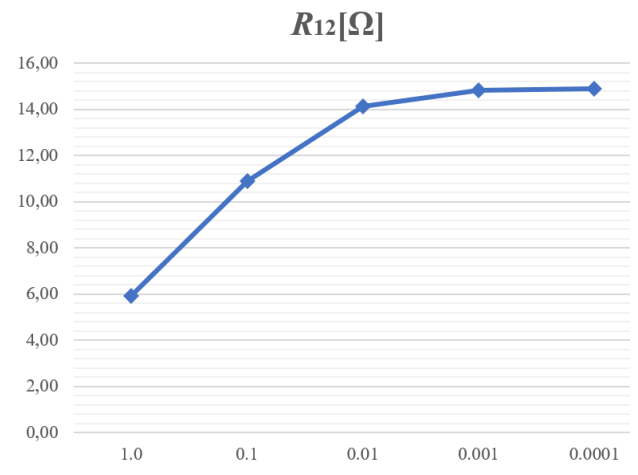


Figure 9: Mutual resistance  $R_{12}$  of the system from Fig. 1 versus ratio  $\sigma_1/\sigma_2$ .

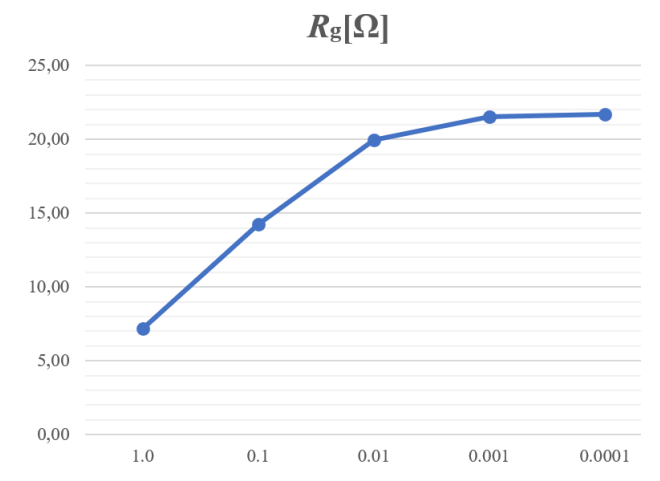


Figure 10: Total resistance  $R_{12}$  of the system from Fig. 1 versus ratio  $\sigma_1/\sigma_2$ .

#### VI. CONCLUSIONS

A semi-analytical procedure for modeling the influence of the cylindrical non-homogeneity influence on the characteristics of two-electrode grounding system is presented in the paper. The described model can be used for approximation of the pillar foundation tubes and other non-homogeneities of similar geometry. The procedure is based on modeling the combined application of the quasistationary image theory and Green's function obtained as solution of Laplace, i.e. Poisson equations.

#### ACKNOWLEDGEMENT

This research was through financial support by the Ministry of Science, Technological Development and Innovation of the Republic of Serbia pursuant to agreements no. 451-03-65/2024-03/200102.

#### REFERENCES

[1] D. D. Vuckovic, N. N. Cvetkovic, D. Krstic, and M. Stojanovic, "Modeling of the road influence on the grounding system in its vicinity," in CD Proceedings of 15th International IGTE Symposium, Graz, Austria, September 16-19, 2012, pp. 294-299.

- [2] D. Vuckovic, N. Cvetkovic, M. Stojanovic, and I. Iatcheva, "Approximate model for ground inhomogeneity with rectangular cross-section: application to analysis of grounding systems," *Electr. Eng.*, vol. 100, pp. 75-82, 2018.
- [3] D. Jovanovic, D. Jovanovic, D. Zivaljević, N. Cvetkovic and Z. Hederic, "Wire grounding electrode near vertical cylindrical non-homogeneity," in Proceedings of 21st International Symposium on Electrical Apparatus & Technologies SIELA, Bourgas, Bulgaria, 2020, pp. 1-4.
- [4] J. Ma and F. P. Dawalibi, "Analysis of grounding systems in soils with cylindrical soil volumes," *IEEE Trans. Power Del.*, vol. 15, pp. 913-918, 2000.
- [5] R. R. Harrington, Field computation by Moment Methods, The Macmillan Company, New York, USA, 1969.
- [6] D. Jovanovic, D. B. Jovanovic, N. N. Cvetkovic, "Ring grounding electrode and coaxial vertical cylindrical ground nonhomogeneity", Proceedings of ICTF 2020-IEICE Information and Communication Technology Forum, Niš, Serbia, 10-12 September 2020, Paper 26.DOI:10.34385/proc.64.ICTF2020\_paper\_28
- [7] D, B. Jovanovic, N. N. Cvetkovic, D. B. Jovanovic, D. D. Vuckovic and Z. Hederic, "Wire grounding electrode placed near cylindrical multi-layered ground non-homogeneity," 22nd International Symposium on Electrical Apparatus and Technologies (SIELA), Bulgaria, 2022, pp. 1-4.

## New Design of a Fast Thomson Drive Actuator Based on Permanent Magnets: Multiphysics Simulation

<sup>1</sup>Yevhen I. Baida, <sup>2</sup>Markus Clemens and <sup>1</sup>Michael G. Pantelyat <sup>1</sup>Department for Electrical Apparatus, National Technical University "Kharkiv Polytechnic Institute", Kyrpychova Str. 2, UA-61002 Kharkiv, Ukraine <sup>2</sup>Chair of Electromagnetic Theory, University of Wuppertal, Rainer-Gruenter-Str. 21, D-42119 Wuppertal, Germany E-mail: m150462@yahoo.com, clemens@uni-wuppertal.de

Abstract—The paper presents a novel mathematical model of a nre design of a fast circuit breaker's drive with a bistable clamp based on highly coercive permanent magnets in which the circuit breaker's drive switches contacts due to the Thompson drive actuator, and the bistability of the mechanism position is ensured by a magnetic system with permanent magnets. The advantage s of this design are: simplicity and reliability; minimum number of moving elements; no electrical energy consumption in bistable positions of the system; high speed. The goal of the paper is to describe the developed mathematical model of the circuit breaker's drive based on the Thompson drive actuator with a bistable magnetic system with permanent magnets and to study the main principles of its operation. The paper solves a multiphysics problem, including the calculation of: static magnetic and transient electromagnetic fields in an inhomogeneous nonlinear medium, taking into account highly coercive permanent magnets and the movement of conducting bodies; electrical circuit taking into account the change in voltage on the capacitor and the back-EMF induced in the coils; dynamics of movement of the armatures of the bistable clamp and drive taking into account changes in mass. Finite element method simulations involve axisymmetric formulations on a deformable mesh. The influence of the disk material, remanent flux density of permanent magnets, storage capacitor capacitance, and coil wire diam eter on the speed of the system has been studied. It is shown that for each specific design there are a number of optimal parameters that ensure the required system speed. Directions for further research are optimization of geometry, parameters of drive coils and capacitors, geometry of the bistable mechanism, volume and remanent flux density of permanent magnets to ensure the required values of speed, contact pressure and dimensions of the device for a specific design of fast circuit breakers.

Index Terms—bistable clamp, highly coercive permanent magnets, multiphysics, Thomson drive actuator.

#### I. INTRODUCTION

In short powerful electrical circuits, short-circuit currents can reach very high values, despite the relatively small rated current. For example, a Schneider Electric circuit breaker with a rated current of 80 A has a breaking capacity  $(I_{cu})$  of 100 kA at a voltage of 220–240 V [1]. However, the actual current switched off by the circuit breaker can and should be significantly reduced by reducing the time from the moment the overcurrent begins to the moment the circuit breaker's contacts begin to diverge (operation time). And the shorter this period of time, the lower the switched-off current, the easier it is to extinguish the electric arc, the smaller the electrodynamic and thermal effect of the current on the line and the circuit breaker. This applies to the greatest extent to DC circuit breakers, in which there is no natural transition of the current through zero, due to which extinguishing the electric arc is difficult, since overcurrents are not limited by the inductive resistance of the line, and the active resistance of the line may be insignificant.

One solution to this problem (reducing the response time) may be to use a Thomson drive actuator [2]-[5] as a circuit breaker's drive mechanism, the advantage of which is the simplicity and reliability of the design, as well as high speed.

However, such devices have a number of significant disadvantages: high speed means significant accelerations and shock loads on structural elements; in addition, it is necessary to fix the position of the contacts and the circuit breaker's mechanism in the on and off positions (bistability condition) in combination with the ability to quickly change the state of the contacts. The problem of reliable fixation of the mechanism position is solved by using bistable mechanical clamps, known for quite a long time [2], [3], [6]. A mathematical model of a drive with optimal control of the speed of movement of the Thomson drive actuator armature and a mechanical bistable clamp is considered in [3] and studied in [7], where the main disadvantages of such a clamp

are shown: design complexity; relatively small stroke; significant (about 6 times greater than the required contact pressure) forces on the circuit breaker body.

A more successful design of a high-speed drive is considered in [8], where the opening of contacts occurs due to the Thompson drive actuator, and fixation of the position of the contacts is achieved due to an electromagnet.

Drives that combine the speed of Thomson drive actuators and the reliability of magnetic systems with permanent magnets [9], [10] are the most promising designs. In [9], the calculation of such a drive consists of two stages: static calculation of magnetic flux and electromagnetic force; calculation of dynamics based on the equations of motion and electrical circuit. The disadvantages of the design include its complexity - two Thomson drive actuator's coils are located inside two magnetic cores; the actuator also has two coils and consists of two magnetic cores with permanent magnets. In addition, the design calculation itself is simplified and not new [11]; it has a number of significant drawbacks, the main one of which is that the braking effect of eddy currents is not taken into account, which is especially significant in high-speed systems.

In contrast to the systems considered, is paper proposes a circuit breaker's drive that commutes its contacts using a Thomson drive actuator, and the bistability of the mechanism's position is ensured by a magnetic system due to the magnetic field of permanent magnets [12]. The advantages of this design are: simplicity and reliability of the design; minimum number of moving elements; no electrical energy consumption in bistable positions of the system; high speed.

Figure 1 shows a diagram of the device with a drive system and the overall dimensions in mm. The coils of the Thomson drive actuator 1, 2 perform the function of switching the device on and off, and can also perform the function of optimal control of the movement of the drive armature and the bistable clamp (changing the speed of the

contacts before closing them).

The armature of Thomson drive actuator 3, made in the form of a disk, is connected to the armature of the bistable clamp 5 by the non-magnetic rod 4. Fixation of armatures 3 and  $\hat{5}$  in the extreme positions (lower and upper) occurs due to the action of highly coercive permanent magnets 6 fixed in a ferromagnetic housing 7. This drive mechanism consumes energy only during actuation. To reduce the speed of contact closure when switched on, a voltage of reverse polarity (relative to coil 1) can be applied to the winding of coil 2, which slows down the speed of movement of the system before the rod touches contacts 8 [12]. The principle of operation of the mechanism: in the "on" position, the contacts 8 are closed, and the required contact pressure is provided by the contact pressure spring 9, the armature 5 is in the lower stable position due to the magnetic flux of the permanent magnet 6.

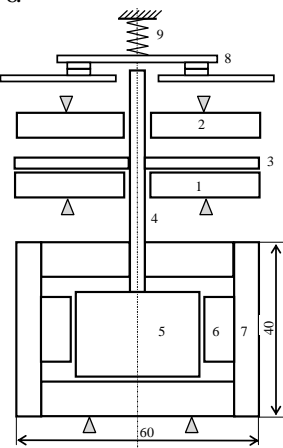


Figure 1. Diagram of a switching device with a Thomson drive actuator and a bistable magnetic clamp: 1, 2 – drive coils; 3 – drive armature (conductive disk); 4 – nonmagnetic rod; 5 – clamp armature, connected by a nonmagnetic rod to the drive armature; 6 – highly coercive permanent magnets located around the perimeter of the clamp armature; 7 – fixed magnetic system; 8 – contact system of the switching device; 9 – contact pressure spring.

If it is necessary to switch contacts, the storage capacitor (not shown in the diagram) is discharged to coil 1, disk 3 with rod 4 moving upward opens the contact circuit, and armature 5, due to the magnetic flux of permanent magnets 6, moves to the upper stable position. To switch on the circuit breaker, it is necessary to apply voltage to coil 2. Such a system can be used for both DC and AC circuit breakers. For a three-phase system, the contacts are opened using a synchronizing shaft.

The novelty of the proposed work lies in a comprehensive study of a new type of circuit breaker's drive, based on a combination of a Thompson drive actuator with a bistable magnetic system based on a ferromagnetic magnetic core with permanent magnets, which makes it possible to fix the position of the circuit breaker's contacts in a simple and reliable way.

The goal of the paper is to describe the developed multiphysics mathematical model of the circuit breaker's drive based on the Thompson drive actuator with a bistable magnetic system with permanent magnets and to study numerically the main principles of its operation.

### II. A MULTIPHYSICS MATHEMATICAL MODEL AND A TECHNIQUE DEVELOPED. ASSUMPTIONS MADE

The mathematical model of the device under study is multiphysics, i.e. the task of sequentially-parallel solution of several problems of different physical nature. The first task is to calculate the static magnetic field in order to determine the initial distribution of the magnetic flux and determine the value of the electromagnetic force of a magnetic system with permanent magnets, which are the initial conditions for solving subsequent problems. The second task is to calculate a transient electromagnetic field in an inhomogeneous conducting nonlinear medium, taking into account the influence of highly coercive permanent magnets. The values of external currents and the speed of movement of the system are determined taking into account the solution of equations for the external electrical circuit and the equations of motion of the moving elements of the system (the armature of the bistable clamp and the disk) taking into account the change in the mass of moving bodies. Assumptions made in the calculation: the coil is a nonconducting object with a uniformly distributed current density across the cross section; the impact is absolutely inelastic and lasts for 0.2 ms; the magnetic core material is isotropic.

The main calculation relationship is a system of equations for a transient electromagnetic field for the k-th subdomain in terms of the magnetic vector potential [13] and the values of the magnetic vector potential at the boundaries of the domains. In its most general form, the system of equations of the electromagnetic field with displacement currents neglected has the form:

$$\sigma_k \cdot \frac{\mathrm{d}\mathbf{A}_k}{\mathrm{d}t} + \cdot \nabla \times \left( \frac{1}{\mu_k} \cdot \left( \nabla \times \mathbf{A}_k - \mathbf{B}_\mathrm{r} \right) \right) = \boldsymbol{\delta}_k , \qquad (1)$$

where  $\sigma_k$  is the conductance of the material of  $\hbar k + \hbar$  subdomain;  $A_k$  is the magnetic vector potential in the  $k+\hbar$  subdomain;  $\mu_k$  is the absolute magnetic permeability of the material of  $\hbar k + \hbar$  subdomain; Br is the remanent magnetic flux density of the material of the permanent magnet;  $\delta_k = (i \cdot N / S) \cdot I_{\varphi}$  is the current density of an external source;  $I_{\varphi}$  is the azimuthal unit vector, directed perpendicular to the plane in which the calculation area is located; i is the current in the coil winding; N is the number of winding turns; S is the area of the coil winding space;  $\mu_k = \mu_k(|B_k|)$ .

System of equations (1) has a different form for each of the calculation subdomains: surrounding space; coil; conductive linear medium; conducting nonlinear medium; permanent magnets. The problem being studied is accordingly steady-state or transient.

In (1), the total derivative is necessary in the case of motion of the region in a magnetic field:

$$\sigma_k \cdot \frac{\mathrm{d} A_k}{\mathrm{d} t} = \sigma_k \cdot \left( \frac{\partial A_k}{\partial t} - \mathbf{v} \times (\nabla \times A_k) \right), \tag{2}$$

where v is the speed of movement of the region.

The initial conditions for the transient problem are the distribution of the magnetic vector potential, obtained from the solution of the steady-state problem taking into account the magnetic field created by permanent magnets.

System of equations (1) must be supplemented with

equations of the external electrical circuit:

$$L \cdot \frac{\mathrm{d}i}{\mathrm{d}t} + R \cdot i + E = \left(U_{C0} - \frac{1}{C} \cdot \int_{t} i \cdot \mathrm{d}t\right) \cdot \eta_{1}, \quad (3)$$

where L is the leakage inductance of the external circuit; R is the active resistance of the drive's coil; C is the capacitance of the storage capacitor,  $U_{\rm C0}$  is the initial voltage on the capacitor,  $\eta_1$  is the unit function that simulates the aperiodic discharge of a capacitor, for which a shunt diode is connected in parallel with the Thomson drive actuator's coil; E is the back-EMF induced in the coil under the influence of a changing electromagnetic field and determined through the angular component of the magnetic vector potential  $A_{\phi}$  in a cylindrical coordinate system based on the formula for magnetic flux reduced to flux linkage [11]:

$$E = \frac{N}{S} \cdot \int_{V} \frac{\partial A_{\varphi}}{\partial t} \cdot dV , \qquad (4)$$

where N is the number of coil tums; S is the cross-sectional area of the coil; V is the coil volume.

The electrical circuit consists of a capacitor connected in parallel to a coil through a thyristor. To ensure an aperiodic discharge, the coil is shunted with a diode. The capacitor is discharged to the coil after a control pulse is applied to the thyristor.

Since the mass of the moving system changes during the movement (the mass of the contacts is added to the mass of the armature of the bistable clamp and the disk during the switching process), the equations of motion in projection onto the directions of movement (z axis) have the following form:

$$\begin{cases}
\frac{\mathrm{d}}{\mathrm{d}t} \cdot \left( m(z(t)) \cdot v(t) \right) = \left[ F_{\mathrm{m}} - F_{r} \right] \cdot \eta_{2}; \\
\frac{\mathrm{d}z(t)}{\mathrm{d}t} = v(t),
\end{cases} \tag{5}$$

where m(z(t)) is the changing mass of the system; v(t) is the systems peed;  $F_{\rm m}$  is the driving force consisting of the electromagnetic force of the Thompson drive actuator and the force acting on the armature of the bistable clamp;  $F_{\rm r}$  is the opposing force, taking into account the weight of the moving system, including at a certain stage the mass of contacts and the force of the contact spring;  $\eta_2$  is the function that prohibits movement of the system beyond permissible limits (stops).

Here:

$$\frac{\mathrm{d}}{\mathrm{d}t} \cdot \left( m(z(t)) \cdot v(t) \right) = \frac{\partial m(z(t))}{\partial z} \cdot v(t)^2 + m(z(t)) \cdot \frac{\mathrm{d}v(t)}{\mathrm{d}t} . \tag{6}$$

#### III. RESULTS OBTAINED AND THEIR ANALYSIS

#### A. Influence of Disk Material on the Speed of the Thomson Drive Actuator

Two materials were used as materials under study: copper and aluminum. The calculation results are shown in Fig. 2-4.

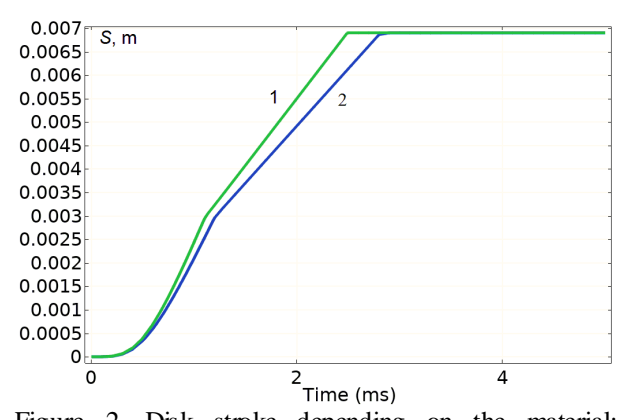


Figure 2. Disk stroke depending on the material: 1 – copper, 2 – aluminum.

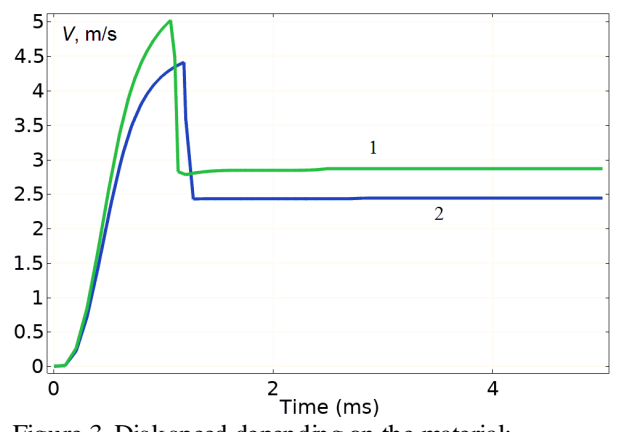


Figure 3. Disk speed depending on the material: 1 – copper, 2 – aluminum

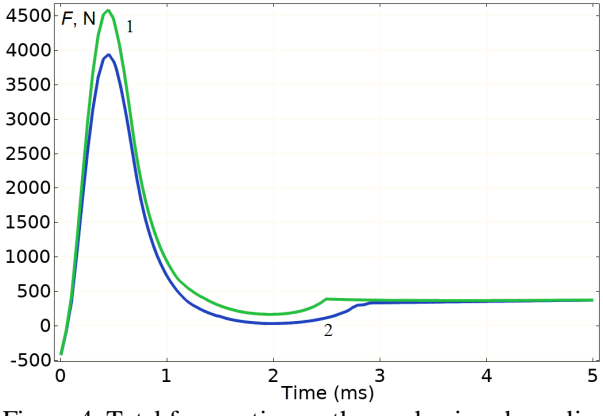


Figure 4. Total force acting on the mechanism depending on the material:

1 – copper, 2 – aluminum.

As follows from the calculation results, the difference for this design is insignificant. This can be explained by the insignificance of the mass of the disk compared to the total moving mass.

All calculations presented below were carried out for a copper disk.

## B. Influence of the Value of the Remanent Magnetic Flux Density of a Permanent Magnet on the Speed of the Thomson Drive Actuator

The value of the remanent magnetic flux density determines the force acting on the mechanism in extreme positions ("on", "off"). For reliable fixation of the

mechanism, it is necessary that this force be greater than the value of the contact pressure, and this force can be changed by selecting the appropriate permanent magnets. Figure 5 shows a series of force values developed by bistable clamps depending on the remanent magnetic flux density of the permanent magnet.

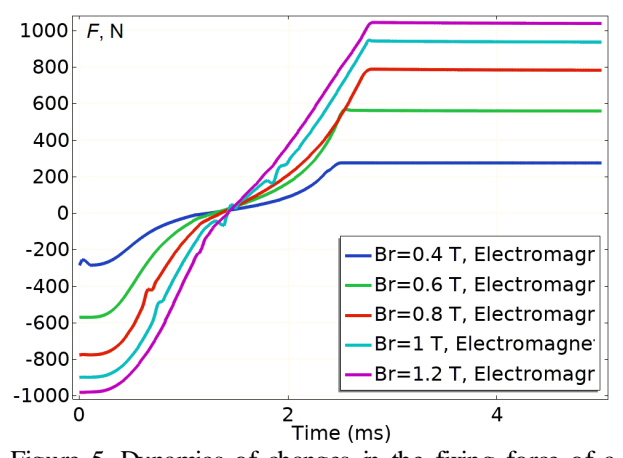


Figure 5. Dynamics of changes in the fixing force of a bistable clamp depending on the value of the remanent magnetic flux density of the permanent magnet.

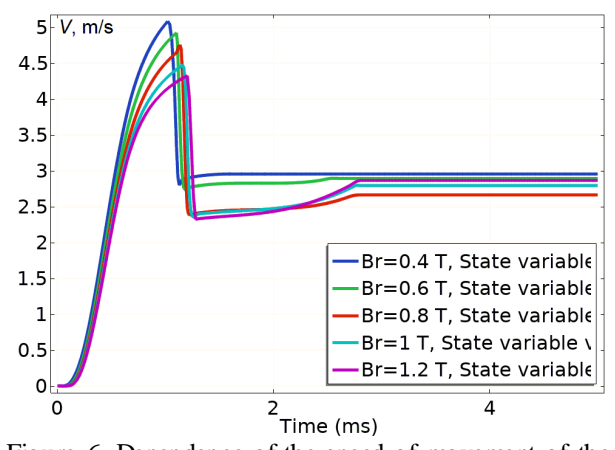


Figure 6. Dependence of the speed of movement of the system on the value of the remanent magnetic flux density of the permanent magnet.

As follows from Fig. 6, the greater the value of the remanent magnetic flux density (the greater the fixing force, see Fig. 5), the longer the time from the start of movement to the opening of the contacts. It should be noted that when the force increases threefold (from  $300\,\mathrm{N}$  to  $1000\,\mathrm{N}$ ), the time increases by only 20%.

Figure 7 shows the influence of the value of the remanent magnetic flux density of permanent magnets on the total force acting on the mechanism.

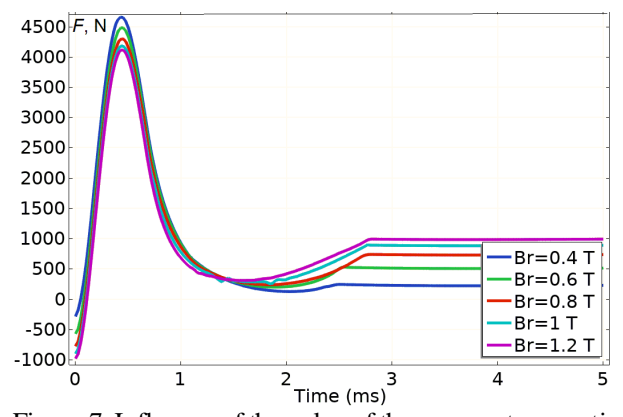


Figure 7. Influence of the value of the remanent magnetic flux density of the permanent magnet on the total force acting on the mechanism.

The influence of remanent magnetic flux density on the total force (the force of the Thomson drive actuator and the magnetic system with permanent magnets) is small (Fig. 7) due to the fact that for given parameters of the electrical circuit (diameter of the coil wire, capacitance of the capacitor), the maximum value of the force is achieved at the moment of time when the armature of the magnetic system of the clamp is near the neutral position and the force of the permanent magnets is low.

#### C. Influence of the Capacitance Value on the Speed of the Thomson Drive Actuator

The value of the capacitance of the storage capacitor determines, on the one hand, the value of electrical energy that tums into mechanical energy of movement, and on the other hand, the time during which this energy is released. In the calculations, the capacitance value varied in the range  $100\text{-}500~\mu\text{F}$  with a step of  $100~\mu\text{F}$ . The calculation results are shown in Fig. 8, 9.

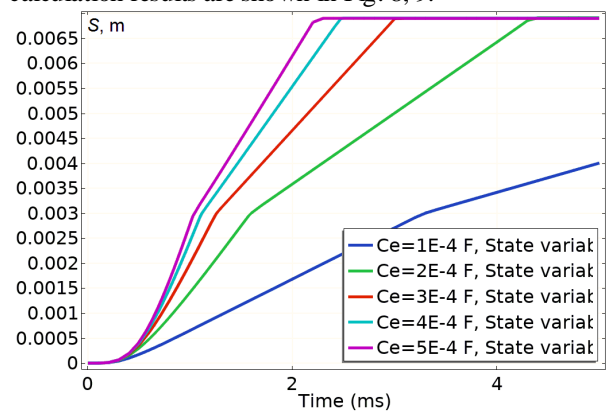


Figure 8. Dynamics of system motion depending on storage capacitor capacitance.

As follows from Fig. 8, the optimal (in terms of speed) capacitance value is  $300\text{-}500~\mu\text{F}$  at a voltage of 600~V (smaller values increase the response time, larger values insignificantly reduce it). With a capacitance of  $100~\mu\text{F}$  there may not be any response.

Figure 9 shows the value of the total force acting on the system.

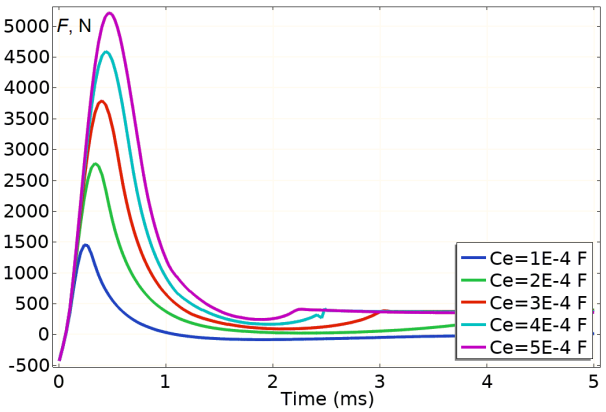


Figure 9. The influence of storage capacitor capacitance on the total force acting on the mechanism.

As expected, the value of the capacitance affects not only the value of the electromagnetic force, but also its impulse.

## D. Influence of the Diameter of the Coil Winding Wire on the Speed of the Thomson Drive Actuator

As mentioned above, the diameter of the wire with which the Thomson drive actuator coil is wound significantly affects the speed, since it determines the number of turns, current density, back-EMF, force impulse and active resistance of the coil. The influence of the diameter of the copper wire with which the coil was wound in the range 0.75-1.75 mm with a step of 0.25 mm is investigated.

Figure 10 shows the result of calculating the stroke of the system.

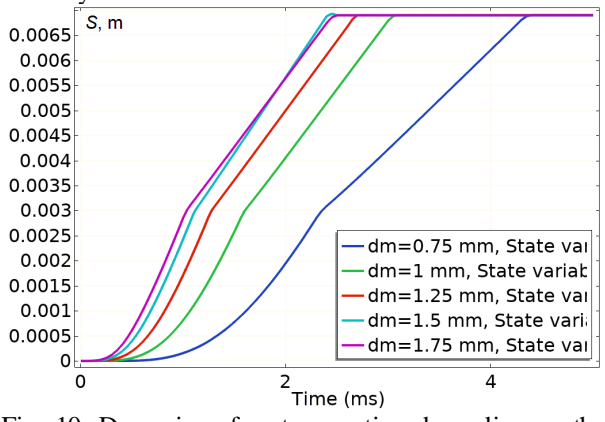


Fig. 10. Dynamics of system motion depending on the diameter of the wire with which the coil is wound.

From Fig. 10 it follows that for the design under study, the optimal (from the point of view of speed) diameter of the wire with which the coil is wound should be 1.25-1.75 mm.

Obviously, one of the parameters affecting the heating of the coil is its current. Figure 11 shows the coil current values when the wire diameter changes.

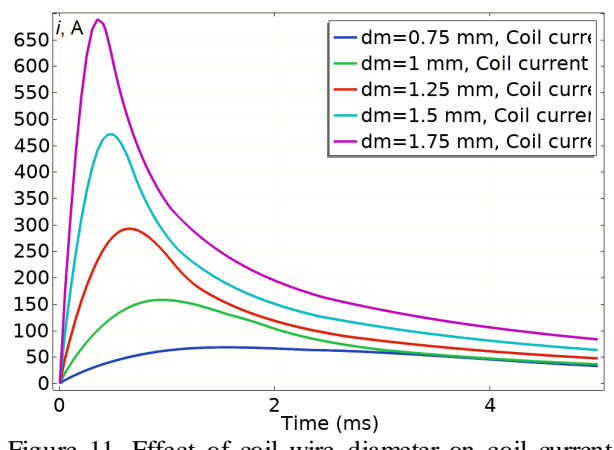


Figure 11. Effect of coil wire diameter on coil current value.

It should be noted that despite the significant current values, the heating of the coil in one cycle is a fraction of a degree due to the short duration of its action.

For illustration, Fig, 12 shows a picture of the magnetic field of the clamp in extreme positions.

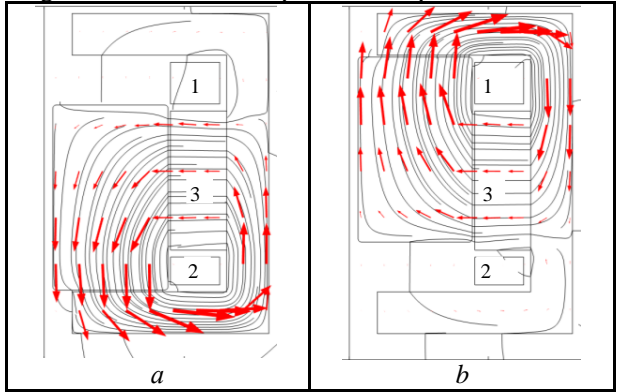


Fig. 12. Magnetic field of the clamp in extreme positions: a – initial, b – final; 1, 2 – either elements for fastening permanent magnets 3 (if the mechanism operates only from the Thomson drive actuator), or coils (if a clamp is used to change the state of the circuit breaker).

As can be seen from Fig. 12, when the armature moves from one extreme position to another, the magnetic field of the permanent magnet changes its direction, which achieves the bistability of the clamp. Here, the maximum values of magnetic flux density in the magnetic core when the remanent magnetic flux density of permanent magnets changed within 0.4-1.2 T are in the range 1.4-2.4 T. Moreover, it should be noted that a change in the position of the clamp armature can occur both under the action of the Thompson drive actuator and due to the redistribution of the magnetic flux by alternately applying voltage of the appropriate polarity to coils 1, 2 (see Fig. 12). In this case, the Thompson drive actuator can only be used to switch off emergency overcurrents. The developed mathematical model makes it possible, in this case, to study the operation of such a system through a slight improvement. Figure 13 shows the distribution of the magnetic field in the magnetic core with a remanent flux density of permanent magnets of 1.2 T.

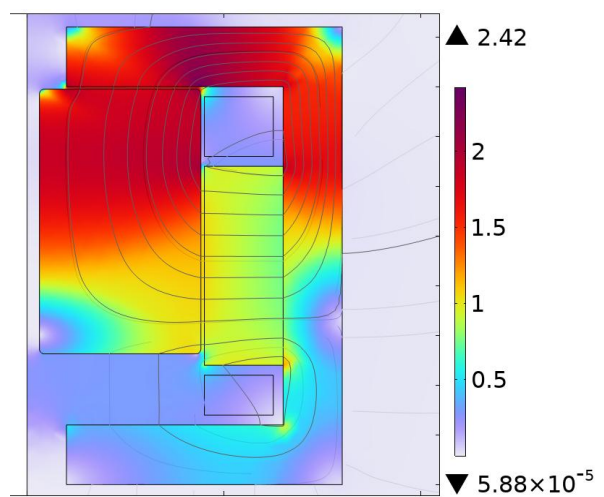


Figure 12. Distribution of magnetic flux density across the cross section of the magnetic core with a residual magnetic flux density of permanent magnets of 1.2 T

#### IV. CONCLUSIONS

- 1. The paper proposes a new design for a circuit breaker's drive, the switching of contacts of which occurs due to the Thompson drive actuator, and the bistability of the position of the mechanism at the extreme points of movement is ensured by a magnetic system with permanent magnets.
- 2. A mathematical model for calculating the proposed drive was developed and tested based on the equations of steady-state and transient electromagnetic fields in a nonlinear moving medium, taking into account its conductivity; equations of an electrical circuit and equations of the dynamics of motion of bodies with changing mass.
- 3. Using the developed mathematical model, the influence of various factors on the dynamics of the drive motion has been studied, namely: the material of the Thompson drive actuator disk; remanent magnetic flux density of permanent magnets; storage capacitor's capacitance values; diameter of the copper wire with which the coils are wound.
- 4. It is shown that the disk material has little effect on the dynamics of the Thompson drive actuator if the moving masses are much greater than the mass of the disk itself; by choosing the value of the remanent magnetic flux density of permanent magnets, it is possible to change the forces in the extreme positions of the drive within a wide range in accordance with the required amount of contact pressure; for each specific system design, there are optimal (from the point of view of speed) values of the discharge capacitance and diameter of the winding wire.

5. The developed mathematical model allows, with a slight improvement, to study the operation of a system in which a change in the position of the clamp armature can occur both under the action of a Thompson drive actuator, and due to the redistribution of the magnetic flux by alternately applying voltage to the corresponding polarity to coils 1, 2 (see Fig. 11). In this case, the Thompson drive actuator can only be used to switch off emergency overcurrents.

#### REFERENCES

- [1] https://www.se.com
- [2] A. Bissal, On the Design of Ultra-Fast Electromechanical Actuators, Licentiate thesis, monograph. Stockholm: Electromagnetic Engineering School of Electrical Engineering, 2013, 68 p.
- [3] W. Wen, Y. Huang, M. Al-Dweikat, Z. Zhang, T. Cheng, S. Gao, and W. Liu, "Research on operating mechanism for ultra-fast 40.5-kV vacuum switches," *IEEE Transactions on Power Delivery*, vol. 30, No. 6, pp. 2553-2560, 2015.
- [4] V.F. Bolyukh and I.S. Schukin, "Investigation of thermal processes in a linear pulse-induction electromechanical converter of cyclic action," *Electrical engineering & electromechanics*, No. 5, pp. 14-22, 2017.
- [5] Ye.I. Baida, "Mathematical modeling of Thomson drive actuator systems," *Electrical engineering & electromechanics*, No. 5, pp. 13-16, 2009 (in Russian).
- [6] G.N. Aleksandrov, V.V. Borysov, V.A. Ivanov, etc., *Theory of Electrical Devices*, Moscow: Higher School, 1985, 312 p. (in Russian).
- [7] Ye.I. Baida and O.G. Volkova, "Mathematical modeling of Thomson drive actuator systems, A mathematical model of a fast drive of a circuit breaker with a Thomson drive actuator and a bistable clamp," *Electrical engineering and power engineering*, No. 1, pp. 30-39, 2018 (in Russian).
- [8] J.-M. Meyer and A. Rufer, "A DC hybrid circuit breaker with ultra-fast contact opening and integrated gate-commutated thyristors (IGCTs)," *IEEE Transactions on Power Delivery*, vol. 21, No. 2, pp. 646–651, April 2006.
- [9] Zh. Wang, L. Sun, S. He, Y. Geng, and Zh. Liu, "A permanent magnetic actuator for 126 kV vacuum circuit breakers," *IEEE Transactions on Magnetics*, vol. 50, No. 3, pp. 129–135, March 2014
- [10] Y. Jeong, H. Lee, Y. Kim and S. Lee, "High-speed AC circuit breaker and high-speed OCR," 22nd International Conference and Exhibition on Electricity Distribution (CIRED 2013), 10-13 June 2013, Stockholm, Sweden, pp. 1215-1218.
  [11] B.V. Klymenko, Forced Electromagnetic Systems, Moscow:
- [11] B.V. Klymenko, Forced Electromagnetic Systems, Moscow: Energoatomizdat, 1989, 160 p. (in Russian).
- [12] Ye.I. Baida, V.V. Lytvynenko, and O.O. Chepeliuk, "Peculiarities of dynamics of a fast-driven induction-dynamic drive with a bistable latch of contacts position of a circuit breaker based on permanent magnets," *Electrical engineering & electromechanics*, No. 1, pp. 3-9, 2020.
- [13] Ye.I. Baida, "A mathematical model of calculation of the dynamics of two-position electromagnetic actuators of medium voltage vacuum circuit breakers," *Journal of scientific* publications of graduate students and doctoral students, No.1, pp. 136-141, 2013 (in Russian).

## Frequency-Dependent Parameter Sensitivity in Undermoded Reverberation Chambers

Anett Kenderes\*†, Szabolcs Gyimóthy\*, and Péter T. Benkő†

\*Department of Broadband Infocommunications and Electromagnetic Theory,
Budapest University of Technology and Economics, Műegyetem rkp. 3., H-1111 Budapest, Hungary

† Mobility Electronics – Electromagnetic Compatibility (ME/EMC5)
Robert Bosch Kft., Gyömrői út 104., H-1103 Budapest, Hungary

E-mail: kenderes.anett@edu.bme.hu

Abstract—The equivalence of working volumes (WV) in reverberation chambers (RCs) is investigated by the regime of state-of-the-art sensitivity analysis (SA) techniques by inspecting the effect of changing configuration parameters to the field uniformity (FU) in a frequency-dependent study close to the lowest usable frequency (LUF). The Sobol'indices as SA measures are evaluated at each stirrer step and frequency. For efficient calculation, different state-of-the-art surrogate modeling techniques were utilized to substitute the full-wave simulation model depending on the characteristics of the WVs. The computational expenses of the problem are further reduced by using a decreased number of stirrer steps and frequencies, which are achieved by means of adaptive sampling techniques through kriging interpolation. Furthermore, the size of the experimental design (ED) set, i.e., the number of different configurations is controlled by performing convergence studies. The proposed method is able to reconstruct the 2D sensitivity map (SM) of the configuration parameters as functions of the stirrer steps and the frequency with a fewer number of samples.

Index Terms—reverberation chambers, sensitivity analysis, surrogate modeling, electromagnetic simulation

The electromagnetic field distribution and its statistical properties in a reverberation chamber (RC) are exploited in several ways for electromagnetic compatibility (EMC) measurement purposes, over-the-air (OTA) tests in communication engineering, antenna measurements, and medical applications, etc. This enclosure provides a more realistic alternative by the omnidirectional illumination of the device under test (DUT) compared to commonly used test facilities like anechoic chambers (AC) and TEM-cells. There exist many so-called stirring techniques for slightly displacing the eigenfrequencies occurred in such cavity resonators to achieve the desired statistical field properties [1]. However, the majority of automotive standards, e.g., [2] favor the traditional mechanical stirring. Such stirrers can most commonly be found in vertical orientation in test configurations for automotive purposes, as in the practical sense, a flexible construction can be easily achieved by applying a fixture with wheels.

Even though the reproducibility of the measurements with respect to setup uncertainties is higher than in conventional methods, the detailed analysis of several parameters is still a hot topic [1], especially in the frequency range, where well-stirred conditions are not met. The possibility of testing parallelization is a powerful feature of RCs, exploiting the theoretically position-independent field properties. During such a process, multiple DUTs can be tested at once. However, the lowest operation frequency required by the automotive standards [2] is comparable with the LUF of an RC of typical sizes. Moreover, there is no unequivocal agreement for the exact value of the LUF, as no abrupt change is present between overmoded and undermoded condition [3]. That is why it makes sense to investigate the equivalence of

simultaneously present WVs inspected with respect to the local statistical field properties.

The main contribution of the previous works [4]-[8] was the utilization of Sobol'indices [9] to RCs. In these studies, a full-wave computational model was built, which was substituted by a black-box model to efficiently calculate the chosen SA measures, while the input parameters of the abstraction were the configuration parameters of the stirrer and the antenna. The slightly modified version of the definition of the so-called composite quality factor (Q-factor) introduced in [10] turned out to be the most suitable to be used as an output quantity for the metamodels [5]. In [6], the equivalence of two horizontally positioned WVs was investigated close to the LUF by the regime of SA techniques accordingly. It was concluded that the field inside the WV closer to the stirrer had more deterministic properties. Furthermore, the other WV showing more ideal behaviour exhibited negligible sensitivity in vertical direction, which would imply a highly space-saving practical benefit, especially that it would possible to stack the WVs w.r.t. this direction, i. e., placing the DUTs above each other. Performing such SA is computationally demanding, requiring to evaluate hundreds simulations with the minimum number of stirrer steps suggested by the standards [2] to reach a prediction error of order 1% in magnitude. Performing a frequencydependent study requires a more computationally effective solution to reconstruct qualitatively the same SM from a lower number of simulations. The aim of the paper [7] was to shed light on these possibilities through convergence studies on the Sobol'indices seeking for the opportunities to decrease the size of the experimental design (ED) set as well as through stirrer-dependent SA studies, to be able to reflect the behaviour of an RC by

utilizing less number of stirrer steps. Moreover, a stirrer step-dependent SA study can reveal the significance of a certain stirrer position, which is of primary importance in a radiated immunity (RI) test performed while applying stepwise stirring. In [8], the aforementioned results were exploited to further reduce the computational burden of the problem, by gradually increasing the ED sample set until a prediction error threshold was reached, yielding an overall smaller sample set compared to the previous studies. Additionally, the stirrer steps were chosen by means of an adaptive algorithm based on kriging interpolation. This paper extends the aforementioned approach by applying the adaptive sampling algorithm to the frequency samples as well by utilizing a 2D input parameter space defined by the stirrer steps and the frequency points.

#### I. METHODOLOGY

#### A. Global SA

In the SA studies, in accordance with the previous works, e.g.,[4]-[8], Sobol' indices were utilized. The benefit of choosing this method is detailed in [4]. These indices defined to represent the contribution of each variable (single, overall) formed in the input parameter vector of the mathematical model to the output vector. The method is based on the decomposition of the output variance of mathematical models into individual variances and subvariances if the distributions of the input parameters are known a priori. The first order and total Sobol' indices are obtained by normalization as follows

$$S_i = \frac{D_i}{D}, \quad ST_i = \frac{D_i + \sum_{i < j}^n D_{ij} + \dots + D_{1,\dots n}}{D},$$
(1)

corresponding to the *i*th variable and scaled to the [0,1] interval. The total as well as the partial variances are denoted as D,  $D_i$  and  $D_{1,\dots N_X}$ , respectively [9], where  $N_X$  stands for the input parameter space dimension, i. e., the number of input parameters to be considered.

#### B. Metalmodeling

In order to obtain these indices in a more computationally efficient way, it is more favourable to replace the full-wave simulation model by a functional approximation

$$\mathcal{M}(\boldsymbol{X}) \approx \mathcal{M}^{\text{Meta}}.$$
 (2)

In this expression, the function  $\mathcal{M}$  would represent an operator which maps the input variables formed in vector  $\mathbf{X}$  to the output quantity, and  $\mathcal{M}^{\text{Meta}}$  is its approximation by utilizing a surrogate modeling technique. In paper [4], three state-of-the-art approaches were investigated. Due to the highly resonant, fluctuating behaviour of the RC, to find a proper output quantity with a moderate amount of fluctuations as a function of the input parameters was challenging. The stochastical viewpoint of the kriging model was found to be suitable. Therefore, it was utilized in, e. g., [4] and [6]. The kriging metamodel [9] considers

the model output as a realization of a Gaussian process, which is formulated by the subsequent equation

$$\mathcal{M}^{K}(\boldsymbol{X}) = \boldsymbol{\beta}^{T} \boldsymbol{f}(\boldsymbol{X}) + \sigma^{2} Z(\boldsymbol{X}, W)$$
(3)

where the first term is the trend, i.e., the mean value of the Gaussian process, formed as the linear combination of known  $f(\boldsymbol{X})$  basis functions, e.g., polynomials, while the second term is a multiplication of the variance of the Gaussian process  $\sigma^2$  and a zero-mean, unit-variance stationary Gaussian process  $Z(\boldsymbol{X}, W)$ . The underlying probability space is represented by W. The latter one is defined in terms of a correlation function, i.e., a correlation family . The most common choice is to aim for the so-called Matérn correlation function which is favoured due to its flexible tuning properties, and written as

$$R(h,\theta,\nu) = \frac{1}{2^{\nu-1}\Gamma(\nu)} \left(2\sqrt{\nu}\frac{h}{\theta}\right) \mathcal{K}_{\nu} \left(2\sqrt{\nu}\frac{h}{\theta}\right), \quad (4)$$

where h=|X-X'|, X and X' are two different observations of one input parameter,  $\theta$  is the scale parameter,  $\nu$  is the shape parameter,  $\Gamma$  is the Euler's Gamma function, finally,  $\mathcal{K}_{\nu}$  is the modified Bessel function of the second kind. The expression simplifies if  $\nu$  is half-integer:  $\nu=p+1/2$ , where p is non-negative. In this case the covariance function is a product of an exponential and a polynomial of order p. The most common choices of the shape parameter are  $\nu=5/2$  and  $\nu=3/2$ . These cases are called Matérn-5/2 and Matérn-3/2 covariance functions, respectively. When  $\nu=1/2$ , the covariance function becomes purely exponential. These three covariances will be investigated in Section III, as the choice of the shape parameter significantly influences the ability to tackle the stochastical fluctuations of the output [11].

In a multidimensional case, i. e., the length of the input parameter vector is M, the multi-dimensional correlation function can be constructed from 1D correlation families, e. g., in the two following ways. The *ellipsoidal* correlation function can be written as [9]

$$h = \frac{1}{\theta} \sqrt{\sum_{i=1}^{M} \left(\frac{X_i - X_i'}{\theta_i}\right)^2},\tag{5}$$

and the separable type is calculated as follows

$$R(\boldsymbol{X}, \boldsymbol{X}', \theta) = \prod_{i=1}^{M} R(X_i, X_i', \theta_i).$$
 (6)

However, as it was concluded in [6], the capabilities of the so-called polynomial chaos kriging (PCK) metamodel [9] yielded a more suitable substitution when investigating the WV closer to the stirrer. In this special case of universal kriging, the trend is constructed as a linear combination of basis functions coming from polynomial chaos expansion (PCE)

$$\mathcal{M}^{\text{PCK}}(\boldsymbol{X}) = \sum_{\alpha \in \mathcal{A}} c_{\alpha} \Psi_{\alpha}(\boldsymbol{X}) + \sigma^{2} Z(\boldsymbol{X}, W). \quad (7)$$

In contrast with the PCE, the Sobol'indices cannot be constructed directly from these two metamodels, the corresponding variances are obtained by Monte Carlo simulations instead [9]. A more detailed description about the utilized surrogate modeling techniques can be read in, e. g., [4].

#### C. Error calculation

To validate the metamodels, the same error calculation, namely the so-called leave-one-out (LOO) cross-validation, is used in this work as in [4]-[8] to quantify the accuracy of the surrogate model and the quality of prediction. Due to the physical model's computational cost, this error metric is more favourable compared to the validation error [9], as in this case, there is no need to generate an independent data set (validation set) to determine its value. The definition reads as follows

$$\epsilon_{\text{LOO}} = \frac{\sum_{i=1}^{N} \left( \mathcal{M} \left( \boldsymbol{X}^{(i)} \right) - \mathcal{M}^{\text{Meta} \setminus i} \left( \boldsymbol{X}^{(i)} \right) \right)^{2}}{\sum_{i=1}^{N} (\mathcal{M}(\boldsymbol{X}^{(i)}) - \hat{\mu}_{Y})^{2}}, \quad (8)$$

where  $\hat{\mu}_Y$  is the sample mean of the experimental design response

$$\hat{\mu}_Y = \frac{1}{N} \sum_{i=1}^{N} \mathcal{M}\left(\boldsymbol{X}^{(i)}\right). \tag{9}$$

and  $\mathcal{M}^{\text{Meta}} = \{\mathcal{M}^{\text{K}}, \mathcal{M}^{\text{PCK}}\}$ . The main idea behind this calculation is to train the metamodel multiple times, leaving out only one data point for evaluation in each iteration and checking the predicting qualities of the surrogate model on this omitted data point. This error metric is used to quantify the consistency of the model at each stirrer step while increasing the ED sample set, i. e., the number of configurations gradually until a threshold value is reached ( $\varepsilon_{\text{LOO}} < \varepsilon_{\text{LOO}_{\text{th},\text{ED}}}$ ) as well as to acquire a stable solution for the kriging interpolation for adaptive sampling introduced in the next subsection ( $\varepsilon_{\text{LOO}} < \varepsilon_{\text{LOO}_{\text{th},\text{kriging}}}$ ).

#### D. Adaptive Sampling

After the metamodels are built at each initial stirrer step positions at certain frequencies in a chosen bandwidth (BW), the subsequent stirrer step - frequency pairs  $\boldsymbol{q}=(k,f)$  are determined adaptively until specific criteria are reached.

The sampling method is performed by means of the efficient global optimization (EGO) algorithm. Similar method was carried out in [8], but the input parameter space was only one dimensional, as the investigations were conducted at one frequency point, around the estimated LUF. Firstly, a kriging metamodel is built at initial points in a 2D input parameter space, which is determined by the stirrer steps and the frequencies. Then, the sample set is broadened, in other words, the approximation gets more and more accurate by selecting new sampling points by utilizing the probability information, i. e., the kriging variance and the mean what the model provides.

The new sampling point is determined by maximizing the so-called expected improvement (EI) function. The algorithm works in such a way that a pointwise search in a finer grid is performed in well-known and unknown regions, simultaneously (exploitation and exploration in machine learning [11]). These two type of regions correspond to the first and second term in the fourth case of eq. (10)).

The approach is similar to [12], but some modifications were needed as the SM to be reconstructed is based on a quite low number of samples in this application (as well as in [8]) and the goal is to further reduce the required stirrer steps. For this sake, instead of a maximum search, the aim here was to find the regions where the parameters change importance, which can be achieved by minimizing the absolute difference between each input parameter pairs. Therefore, overall  $\binom{N_X}{2}$  EI functions need to be constructed from the same number of kriging metamodels for the first order and total Sobol'indices in all the monitored WVs, respectively. Moreover,  $N_X$ additional kriging surrogate models are built, as the final goal is the determination of the Sobol'indices as functions of the stirrer steps, but the EGO is carried out only on the  $\binom{N_X}{2}$  metamodels constructed from the absolute differences. The approach differs from [8] only in one aspect, the input parameter space is now twodimensional ((k, f)-space) instead of one (k-space).

In order to keep the number of new sampling points low, different restrictions were imposed, as in [8]. Based on the probability information, which can be obtained from the kriging metamodel, the probability of reaching a certain upper or lower bound for the Sobol'indices corresponding to the differences can be determined and the EI functions could be set to zero. This approach can prevent from unnecessary oversampling in regions, where the minimal difference is already determined (lower bound – first case in eq. (10)) or the knowledge of the exact value is unimportant as the importance would not change anymore (upper bound – second case in eq. (10)). Moreover, if a parameter is *unimportant*, i.e. has a low Sobol'index at a certain stirrer step, the investigation of its behaviour is not needed anymore and it is also unlikely that this parameter will take part in the importancechange action. Therefore, the EI corresponding to the difference pairs in which this parameter is involved can be set to zero (third case in eq. (10). The resulting EI function has the following form

$$\operatorname{EI}_{i}(\boldsymbol{q}) = \begin{cases} 0, \mathbb{P}(\hat{S}_{i,\operatorname{diff}} < S_{\operatorname{diff,low}}) \geq p_{\operatorname{diff,low}} \\ 0, \mathbb{P}(\hat{S}_{i,\operatorname{diff}} > S_{\operatorname{diff,high}}) \geq p_{\operatorname{diff,high}} \\ 0, \mathbb{P}(\hat{S}_{i} < S_{\operatorname{low}}) \geq p_{\operatorname{low}} \\ u_{i}(\boldsymbol{q}) \Phi\left(\frac{u_{i}(\boldsymbol{q})}{\hat{\sigma}_{i}(\boldsymbol{q})}\right) + \hat{\sigma}_{i}(\boldsymbol{q}) \phi\left(\frac{u_{i}(\boldsymbol{q})}{\hat{\sigma}_{i}(\boldsymbol{q})}\right), \text{ otherwise,} \end{cases}$$
(10)

where k is a certain stirrer step,  $\hat{S}_{i,\text{diff}}(q)$  is the mean value, i. e. the kriging trend,  $\hat{\sigma}_i(k)$  is the kriging variance,

and

$$u_i(\boldsymbol{q}) = \min{\{\hat{S}_{i,\text{diff}}(\boldsymbol{q})\}} - \hat{S}_{i,\text{diff}}(\boldsymbol{q}),$$
 (11)

$$i=1\dots \binom{N_X}{2}.$$
 (12)

The EI functions are then normalized in the following way, in order to treat each difference equally

$$EI(\mathbf{q}) = \frac{\sum_{i=1}^{\binom{N_X}{2}} EI_i}{\max EI_i(\mathbf{q})}.$$
 (13)

Finally, the new stirrer step is determined by maximizing the EI function with the following restriction

$$q_{\text{new}} = \arg \max_{q} \text{EI}(q),$$
 (14)

$$q_{\text{new}} = \arg \max_{q} \text{EI}(q),$$
 (14)  
 $\operatorname{dist}(q, q_{\text{new}}) < q_{\text{th}}, \forall q \in Q_{\text{set}},$  (15)

where  $q_{
m th}$  is the threshold for the sample distance and  $Q_{
m set}$  is the current stirrer sample set. By setting this limiting value, the minimum search can be performed in larger steps. On the other hand, we might loose the ability to predict the exact value of the intersections corresponding to the importance change and the accuracy also can degrade, but in our application, it is enough to know that this change in between which stirrer steps and around which frequency points will occur. Moreover, the knowledge of the exact value of the Sobol'indices does not carry any additional information. Due to the stochastic nature of the algorithm, there is no rigorous expression on the required number steps until which the exploration of the modeled function can be ensured adequately. To this end, there are many ways to set a stopping criterion. In this paper (so as in [8]), the number of samples are also restricted

$$N_{\text{samples,max}} = k_{\min} \frac{\text{BW}}{N_{\text{freq,fraction}}}$$
 (16)

where  $k_{\min}$  is the minimum number of stirrer step required by the standard around the LUF, BW is the chosen bandwidth, and  $N_{\rm freq,fraction}$  is the number of fractions in which the BW is partitioned. Besides, the normalized kriging variance can provide an adequate information on the existence of insufficiently explored regions,

$$\frac{\hat{\sigma}_{i}(\boldsymbol{q}) - \min_{\boldsymbol{q}} \{\hat{S}_{i,\text{diff}}(\boldsymbol{q})\}}{\max_{\boldsymbol{q}} \{\hat{S}_{i,\text{diff}}(\boldsymbol{q})\} - \min_{\boldsymbol{q}} \{\hat{S}_{i,\text{diff}}(\boldsymbol{q})\}} < \hat{\sigma}_{\text{norm}_{\text{th}}}, (17)$$

that is why a threshold value is set on these quantities. Furthermore, another limiting value is set in order to prevent the occurrence of unphysical fluctuations of the Sobol'indices as functions of the stirrer steps by controlling the maximum value of the LOO error ( $\varepsilon_{\mathrm{LOO}}$  <  $\varepsilon_{\rm LOO_{\rm th,kriging}}$ ).

#### II. TEST PROBLEM

The model of an RC with approximate sizes of  $4 \,\mathrm{m} \times 5 \,\mathrm{m} \times 3 \,\mathrm{m}$  is built using the commercially available simulation software CST [13]. The E-field is monitored within the maximum number of achievable multiple WVs placed horizontally next to each other as depicted in Fig. 1, in accordance with the standards [2]. The two WVs are preliminary placed at  $\lambda/4$  distance at the lowest frequency of use. The large rectangular volume depicted as a transparent object in Fig. 1 is the maximum achievable WV taking the aforementioned prerequisite into consideration. The TX antenna was chosen to be a dipole for the sake of reducing computational complexity, as in [4]-[8], which points to one of the outermost corners with respect to the WVs. The TX antenna and the stirrer are also at a minimum distance, to study the worst-case scenario.

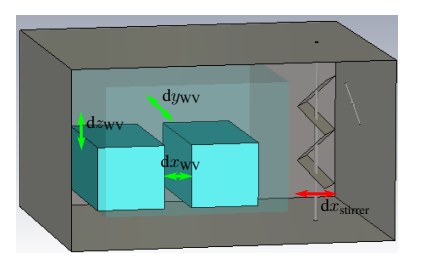


Fig. 1: Configuration parameters [6]

#### A. Input Parameters

In Fig. 1, the input parameters corresponding to the stirrer are marked in the red, while the WV-related ones are highlighted in green. The displacements were chosen to be the largest, taking the aforementioned distance requirement from each metallic object (including the Efield probe sensors in the real measurement environment) into consideration [2]. The ranges of the input parameters are listed in [6]. The position of the DUTs are kept fixed during this investigation.

#### B. Output Parameters

In the previous papers [4]-[7], the Q-factor was chosen as the output parameter for performing the SA, as it is claimed to be the most stable quantity to characterize the statistical properties of RCs [14]. As each eigenfrequency is associated with a Q-factor, it is possible to define the composite Q-factor, which reflects the stochastical behaviour of the RC. The following approximation can be used under well-stirred condition [10]

$$\tilde{Q} \approx \frac{1}{2} \omega \varepsilon V \langle \tilde{E} \rangle^2,$$
 (18)

where  $\omega$  is the angular resonance frequency,  $\varepsilon$  is the permittivity of the air, V is the RC volume,  $\langle \tilde{E} \rangle$  is calculated as a total average over all stirrer rotations and sampling positions, normalized with the square root of the average input power with respect to the stirrer rotation. To some extent, this formula provides a reasonable approximation in the lower frequency range. Caused by the nature of the reverberant environment, the Q factor is fluctuating as a function of the input parameters. In order to smoothen this behaviour as well as to get a more suitable approximation for the volume integral in the original definition, the E-field is densely sampled, and extracted from the two subvolumes corresponding to the two WVs of inspection, as the 3D solution is directly accessible by the nature of the FEM. The configuration parameters were set via MATLAB. In order to provide a detailed analysis on the effect of the stirrer as well as with the frequency, (18) is calculated only over the sampling positions, but on the stirrer steps.

#### III. RESULTS

In [6]-[7], the SA studies were carried out performing  $N_{\rm stirrer} \times N_{\rm samples} = 12 \times 200 = 2400$  full-wave simulations at 170 MHz, which is quite inefficient for a frequency-dependent SA study. In [7], it was justified that it is possible to build up a surrogate model for each stirrer step with an admissible LOO. Therefore, a sampling strategy such as the one detailed above and the 1D form in [8] can be proposed to reduce the computational complexity. By gradually building up the ED sample set while checking the convergence w. r. t. the LOO at each stirrer step, the required number of different configurations could be reduced approximately by half. In the previous studies, the Matérn-5/2 covariance function was utilized with ellipsoidal correlation function. In this paper, three more correlation functions describen in Section I/B were investigated, and the Matérn-3/2 covariance function with separable correlation function exhibited the best performance in handling the fluctuations, thus reducing the LOO by one and in some cases even two order ( $\sim 10^{-4} \dots 10^{-3}$ ). It is worth mentioning that due to the heuristic nature of the method, the number of needed stirrer steps depends on the initial sampling points. As the main intention was to propose this algorithm with the need of as little a priori information as possible, the lowest number of needed stirrer steps and frequency points were used in order to reach the proper quality of reconstruction with a reasonable number of samples. The sampling algorithm was started with 4 stirrer steps and 4 frequency points, which yielded 16 initial samples in total. The kriging interpolation was performed on a grid covering 50 stirring steps, in order to provide a smooth approximation. Tab. I contains the threshold values, which were utilized to produce the SMs. For the sake of brevity, only the first Sobol'indices obtained for the two WVs are depicted in Fig. 2, as this is the parameter, which reflects the single contribution of an input variable. The investigated bandwidth is from 170 MHz to 180 MHz, around the estimated LUF. The results are compared with the SA carried out without the adaptive sampling by utilizing  $N_{\text{stirrer}} \times N_{\text{freq}} \times N_{\text{conf}} = 12 \times 8 \times 100 = 9600$ samples, where the terms stand for the number of stirrer steps, frequency points and configurations, respectively. By carrying out convergence studies, it is possible to reduce  $N_{\text{conf}}$  by half and the number of (k, f) pairs also could be decrease from 96 to 49 in  $WV_1$  and 27 in

Parameter	Value	
$k_{\min}$	12	
$_{\mathrm{BW}}$	$10\mathrm{MHz}$	
$N_{ m freq,fraction}$	10	
$N_{\rm samples, max}$	96	
$S_{ m diff,low}$	0.05	
$S_{ m diff,high}$	0.3	
$S_{ m low}$	0.1	
$p_{ m diff,low}$	90 [%]	
$p_{ m diff,high}$	90 [%]	
$p_{ m low}$	90 [%]	
$k_{ m th}$	0.5	
$k_{ m max}$	12	
$arepsilon_{ m LOO_{ m th,ED}}$	1 [%]	
$\varepsilon_{ m LOO_{th,kriging}}$	100  [%]	

TABLE I: Threshold values for the adaptive sampling algorithm

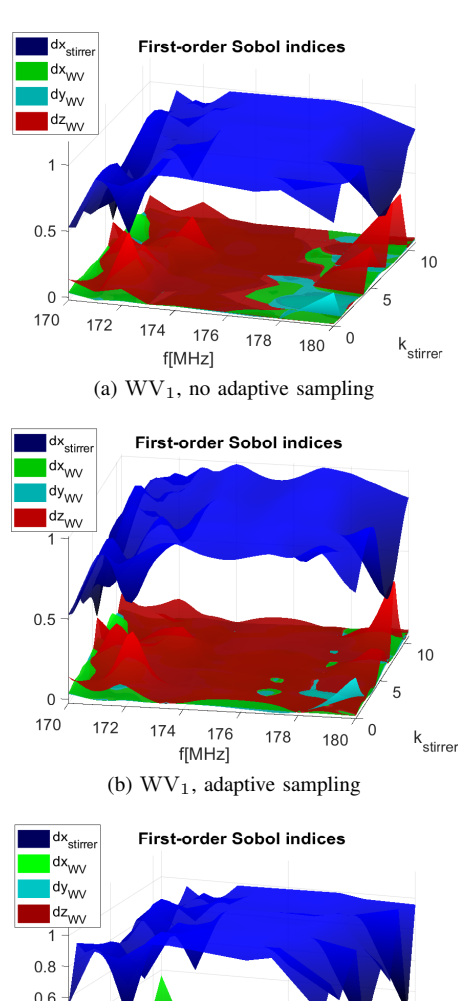
 $WV_2$ , which can be further reduced as depicting the peak values is less important than identifying the regions of the *importance change*. This also means, that the SA can be performed involving a larger BW by using the same order of number of samples, which will be the subject of the analysis in the near future. The discrepancies around  $178\,\mathrm{MHz}$  are due to the restrictions imposed in the first and third line in (10). This was the cost of neglecting the samples corresponding to *unimportant* Sobol' indices and negligible differences. Interestingly, the dissimilarities between the two WVs are in the beginning and in the end of the investigated BW.

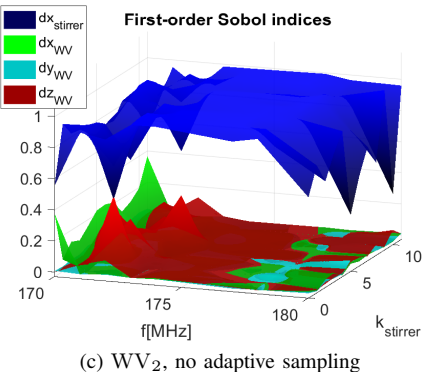
#### IV. CONCLUSION

In this work, the equivalence of working volumes (WV) in empty reverberation chambers (RCs) were investigated by the regime of state-of-the-art sensitivity analysis (SA) techniques while inspecting the effect of changing configuration parameters to the field uniformity (FU) in 10 MHz of BW close to the lowest usable frequency (LUF). It was justified that the proposed method is able to reconstruct the SM of the configuration parameters as functions of the stirrer steps and the frequency with a fewer number of samples. It can be clearly stated that the method of Sobol' indices can reveal the main differences between the simultaneously present WVs. In the near future, a frequency-dependent study will be carried out in a wider BW. Furthermore, the loaded condition, i. e. the effect of the presence of simultaneously tested DUTs will be investigated for DUTs with different volumetric extent. It is worth mentioning that the proposed algorithm is feasible only with moderate input parameter dimensions as the  $\binom{N_X}{2}$  value increases rapidly. A feasibility study about the size of the input parameter set could be involved is also part of a future work. The final goal is that the abovementioned approach should serve as a basis for test setup adaptation during parallelized RI measurements.

#### ACKNOWLEDGMENT

The reported research was supported by the Doctoral Student Scholarship Program (Cooperative Doctoral Pro-





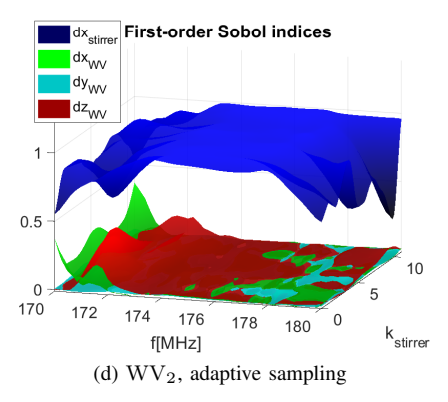


Fig. 2: The stirrer step-dependent Sobol'indices obtained for the two different WVs at 170 MHz by equidistant (left) and adaptive sampling (right) [7]

gram, Ministry for Innovation and Technology, source of the National Research Development.

#### REFERENCES

- Q. Xu, Y. Huang, Anechoic and Reverberation Chambers: Theory, Design, and Measurements, John Wiley & Sons, 2019.
- [2] ISO 11452-11, Road vehicles Component Test Methods for Electrical Disturbances from Narrowband Radiated Electromagnetic Energy — Part 11: Reverberation chamber, 2010.
- [3] C. L. Holloway, D. A. Hill, J. M. Ladbury, G. Koepke, "Requirements for an Effective Reverberation Chamber: Unloaded or Loaded," in *IEEE Transactions on Electromagnetic Compatibility*, Vol.48.1, pp. 187-194, 2006.
- [4] A. Kenderes, Sz. Gyimóthy, P. T. Benkő, ,"On the Field Uniformity of Reverberation Chambers a Global Sensitivity Analysis Study," in COMPEL The International Journal for Computation and Mathematics in Electrical and Electronic Engineering, Vol. 42 No. 5, pp. 1066-1078. 2023.
- [5] A Kenderes, Sz. Gyimóthy, P. T. Benkő, "Sensitivity Analysis with Various Parameters in Undermoded Reverberation Chambers," in COMPEL – The International Journal for Computation and Mathematics in Electrical and Electronic Engineering, accepted for publication, 2024.
- [6] A. Kenderes, Sz. Gyimóthy, and P. T. Benkő, "On the Equivalence of Working Volumes in Reverberation Chambers Close to the Lowest Usable Frequency," EMC Europe 2024, Bruges, Belgium, accepted for publication, May 2024.
- [7] A. Kenderes, Sz. Gyimóthy and P. T. Benkő, "On the Equivalence of Working Volumes in Undermoded Reverberation Chambers," *IEEE 21st Biennial Conference on Electromagnetic Field Com*putation (CEFC), Jeju, Republic of Korea, 2024, accepted for publication, Oct 2024.
- [8] A. Kenderes, Sz. Gyimóthy and P. T. Benkő, "Efficient Reconstruction of the SM Characterizing the Equivalence of Working Volumes in Undermoded Reverberation Chambers," 19th European Conference on Antennas and Propagation (EuCAP) 2025, Stockholm, Sweden, submitted for publication, Oct 2024.
- [9] S. Marelli, B. Sudret, UQLab: A Framework for Uncertainty Quantification in Matlab, American Society of Civil Engineers, 2014.
- [10] S. Wang, Z. C. Wu, G. H. Wei, Y. Z. Cui, L. S. Fan, "A New Method of Evaluating Reverberation Chamber Q-Factor with Experimental Validation," in *Progress In Electromagnetics Research Letters*, Vol. 36, pp. 103-112, EMW Publishing, 2013.
- [11] C. K. I. Williams, C. E. Rasmussen, Gaussian Processes for Machine Learning, Vol. 2,No. 3, MIT Press Cambridge, MA, 2006.
- [12] A. Bingler, S. Bilicz and M. Csörnyei, "Global Sensitivity Analysis Using a Kriging Metamodel for EM Design Problems With Functional Outputs," in *IEEE Transactions on Magnetics*, vol. 58, no. 9, pp. 1-4.
- [13] CST Studio Suite Getting Started, CST Studio Suite 2024, Darmstadt, Germany
- [14] P. Corona, G. Ferrara, M. Migliaccio, "A spectral Approach for the Determination of the Reverberating Chamber Quality Factor," *IEEE Transactions on Electromagnetic Compatibility*, vol. 40, no. 2, pp. 145-153, 1998.

## Effect of Physical and Geometric Parameters on Eddy Current Sensor Response

\*D. Sedira, †B. Messaoudene, †K. Berkas and \*N. Ferkha

\*Laboratory of Electrical Engineering and Industrial Electronics (L2EI), Faculty of Science and Technology, University of Jijel, Jijel 18000, Algeria

<sup>†</sup>Electrical Engineering Department, Faculty of Science and Technology, University of Jijel, Jijel 18000, Algeria E-mail: d\_sedira@univ-jijel.dz

Abstract—This paper deals with the effects of geometric and physical parameters variation on the response of an eddy current sensor. A 2D time harmonic eddy current model is adopted and solved using finite element method. The objective is to determine the variation of the impedance difference of the system for each studied case.

Index Terms— Eddy current testing, Electromagnetic phenomena, Finite element method.

#### I. INTRODUCTION

Nondestructive testing NDT is the use of special equipments and methods to make sure that parts are free of defects without degrading the object [1]. NDT is used in many industries such as aerospace, nuclear industry and pipeline construction. There are several very popular NDT techniques ultrasonic [2], radiography [3], eddy current [4], magnetic particles [5], acoustic emission [6] and magnetic flux leakage testing [7]. The use of each method depends on the conditions in which the control should be conducted out, the piece to be examined and and the kind of inspections to be performed. Among the most used NDT methods, eddy current technique is a powerful tool used to inspect flaws, defects, cracks and other irregularities in conductive materials [8][9][10]. Eddy current testing can reveal the smallest defects. Its high precision guarantees that problems are detected early on, reducing the possibility of major breakdowns. Eddy current testing is known for its capacity to quickly analyze large pieces of material. The non-destructive control equipment is small and does not require contact with the part to be tested. The factors that affect the effectiveness of this method are essentially the electrical conductivity, the magnetic permeability, the material thickness, the liftoff, the edge effect, the frequency and the current intensity of the test coil. Zhengyu et al [11] provide an investigation on the effect of excitation frequency, liftoff value and internal defect size under weak magnetization in a ferromagnnetic material, using a novel dynamic permeability testing (DPT) method. A method using normalization and two reference signals for minimizing the lift-off problem with pulsed eddy current techniques is suggested [12]. Capobianco et al[13] investigated how geometric parameters of the probe coil, metal permeability, magnetic core diameter, and lift-off height affect sensor sensitivity. Song et al[14] study the influence of different probe coil models on eddy current testing, in[15] the best frequency for detecting slit defects on the backside of thick steel plate was determined through experiments and electromagnetic simulations using FEM. Experiments were conducted by Nagendran

et al [16] to determine the best eddy current excitation frequencies for flaws placed at various depths below the top surface of an aluminum plate.

This paper presents a more in-depth examination into the factors that influence the method of induced currents, by presenting the fluctuation of the impedance difference. For that Software Comsol Multiphysics is used to model the sample presented in [17].

This work is structured as follows. First, the principle of eddy currents technique is presented. Then the quasistatic partial derivative formula for electromagnetic phenomena in the case of eddy current testing are established using the well-known Maxwell's equations. Following that, a set of simulations are performed to examine the effect of excitation frequency, the electrical conductivity, the lift-off and finally the position of the defect. At the end a conclusion is given to summarize the obtained results which present a good agreement with the theory.

#### II. MODELING

#### A. Principle of eddy current testing

Eddy currents are creating through Faraday's law. Eddy current testing consists of creating, in conductive materials, currents induced by a variable magnetic field, by means of a coil. In the presence of a defect the movements of these induced current are disrupted, thus causing a variation in the impedance of the sensor. The examination of these changes in impedance provides useful information for carrying out the check of the piece.

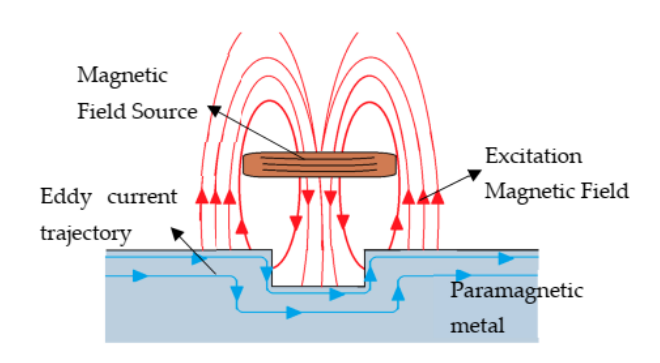


Figure 1: Principle of eddy current testing [18]

#### B. Diffusion Equation

Generally, a nondestructive testing by eddy currents includes magnetic region, conducting region and air region. Neglecting the displacement currents and charge density, the mathematical representation of the electromagnetic phenomenon follows the Maxwell's equations given by:

$$rotE = -\frac{\partial B}{\partial t}$$
 (1)

$$rotH = J (2)$$

$$div \mathbf{B} = \mathbf{0} \tag{3}$$

Where E, B and H correspond to electric field, magnetic flux density and current density respectively. Equation (3) allows to define the magnetic flux density as a function of the magnetic vector potential A:

$$\mathbf{B} = \mathbf{rotA} \tag{4}$$

In a linear and isotropic material the following equation can be written:

$$\mathbf{B} = \mu \mathbf{H} \tag{5}$$

Where  $\mu$  is the magnetic permeability.

The expression of current density is given by the current density used to excite the coil  $J_{ex}$  and the induced current in the conductive piece  $J_{ind}$  such as:

$$\mathbf{I} = \mathbf{I}_{ex} - \mathbf{I}_{ind} \tag{6}$$

The expression of the induced current density provided in the equation below is:

$$I_{ind} = \sigma E \tag{7}$$

Where  $\sigma$  is the electrical conductivity in conductive piece. The electric field intensity is given by:

$$E = -\frac{\partial A}{\partial t} \tag{8}$$

Substituting equation (6) and equation (5) in equation (2) yields:

$$\frac{1}{a} rot(rot(A)) = J_{ex} - \sigma \frac{\partial A}{\partial t}$$
 (9)

Under steady-state conditions the equation above can be written as:

$$\frac{1}{\mu} rot(rot A) = J_{ex} - j\omega\sigma A$$
 (10)

Where  $\omega$  is the angular frequency.

When modeling two dimensional applications, the magnetic vector A and the current density  $J_{ex}$  have one component.

Because of the computation time of the investigated cases, the diffusion equation is resolved using the Comsol multiphysics software, which uses the finite element method.

#### C. Impedance Computation

The impedance of the coil is calculated from energy considerations[19], the magnetic energy W stored in the entire study space and the energy dissipated in the conductive part which represents the heat losses P.

$$W = \frac{1}{2}LI_{ex}^{2}$$
 (11)

$$P = RI_{sv}^{2} \tag{12}$$

Where  $I_{ex}$  is the excitation current. R and L are the resistance and the inductance of the coil respectively

The impedance of the source is given by:

$$Z = R + j\omega L \tag{13}$$

In order to calculate the coil impedance difference, the problem is solved twice, with flaw and with free-flaw. It is calculated according to the follow expression:

$$\Delta Z = Z_d - Z_0 \tag{14}$$

Where  $Z_d$  is the impedance with presence of flaw and  $Z_0$  the impedance without flaw.

#### III. RESULTS AND DISCUSSION

The simulated problem obtained from [17] is shown in figure 2. A coil carrying an alternating current moves along Ox axe on a conductive piece. The latter has a deep flaw located at its middle.

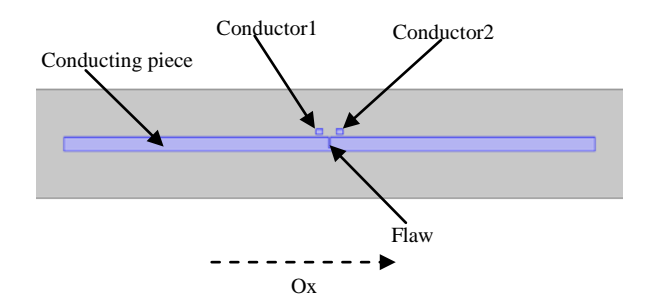


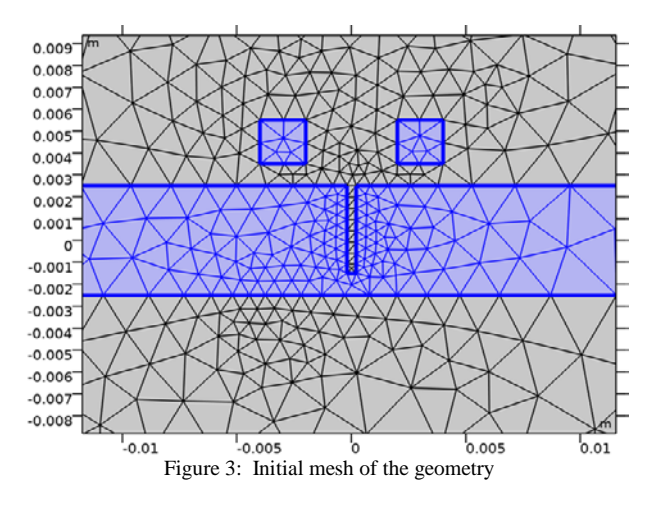
Figure 2: 2D Geometry of studied system

The geometric parameters of the simulated model are given in table 1. Since the author studied the plate as a conductive half-space, its width is not specified. So, it is chosen arbitrarily. The distance separating the two conductors is 0.006m

TABLE I GEOMETRIC MODEL PARAMETERS

Name	Length[m]	Width[m]	
Conductive plate	0.16	0.005	
Flaw	0.0004	0.004	
Conductors	0.002	0.002	

A zoom of finite element discretisation of the geometry on flaw region before and after refining meshes is shown in figure 3 and figure 4 respectively.



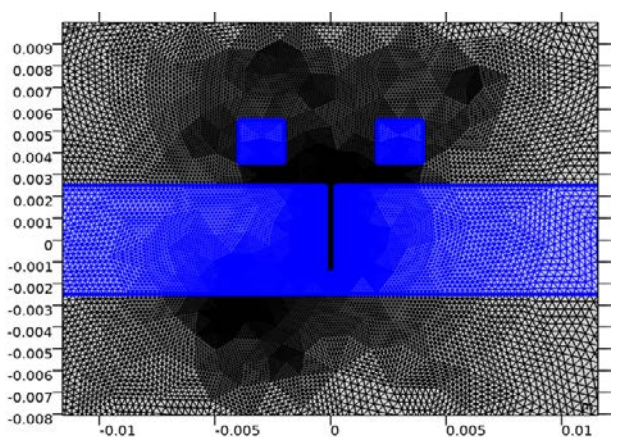


Figure 4: Zoom on refined mesh

In each simulation case studied, the magnetic energy, the dissipated energy and the impedance value are calculated in 31 positions of the coil's center. To avoid the edge effect the displacement points are chosen within the range of -0.02 m to +0.02 m.

#### A. Effect of frequency

This computation includes six frequencies 1KHz, 2KHz, 4KHz, 6KHz, 8KHz and 10KHz. The electrical conductivity in the plate of Aluminium is 35.4\*10<sup>6</sup> S/m and the relative magnetic permeability  $\mu_r$  is 1, the distance between the coil and the plate is 0.001m. For a displacement of +0.003 m of the coil it can be show from figure 5,figure 6 and figure 7 that the intensity of the induced eddy currents in the test piece increases with the frequency of the source current. However the depth of penetration decreases with the increase of frequency. The optimal inspection frequency is 1000 Hz because the induced currents passed through the entire depth of the flaw, this result is in concordance with the excitation frequency used in[17]. Therefore, this frequency will be adopted for the study of the other effects.

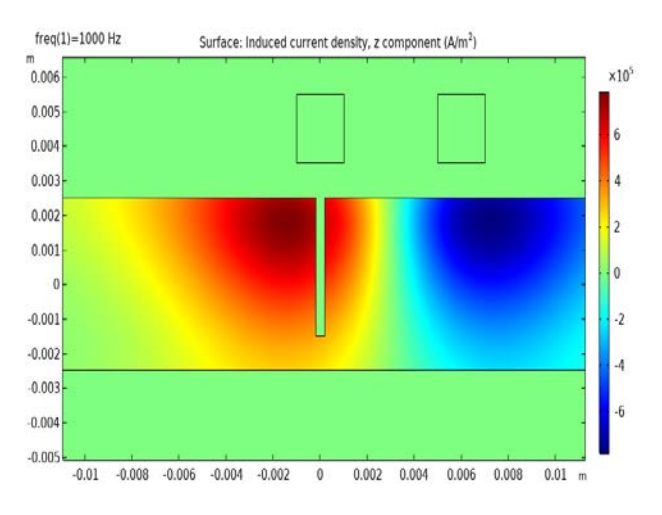


Figure 5: Surface induced currents for f=1KHz

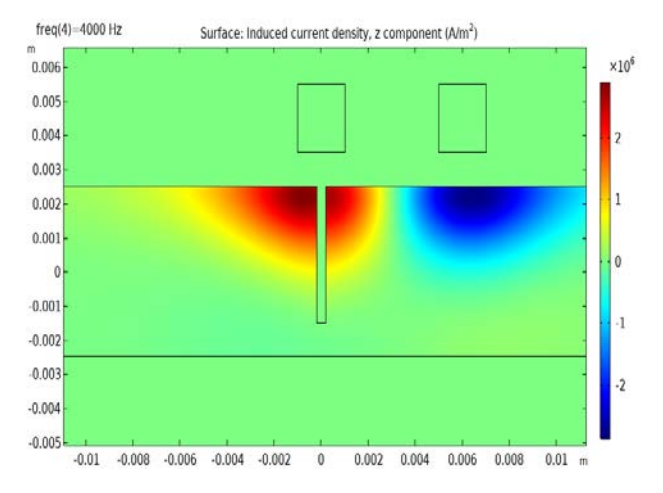


Figure 6: Surface induced currents for f=4KHz

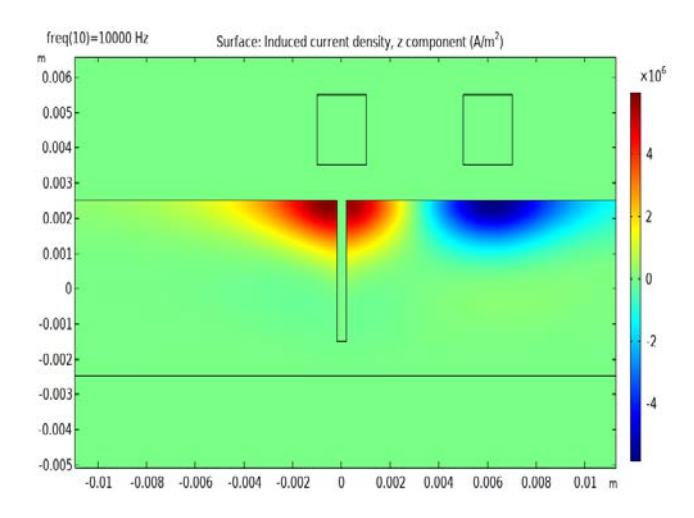


Figure 7: Surface induced currents for f=10KHz

It can be shown from figure 8, that when the frequency increases the variation of the impedance difference  $\Delta Z$  increases. Indeed, the rise in frequency leads to high induced currents in the conductive piece, consequently, the magnetic fields created are significant. These fields oppose the magnetic fields created by the coil, which leads to an important changes in coil impedance.

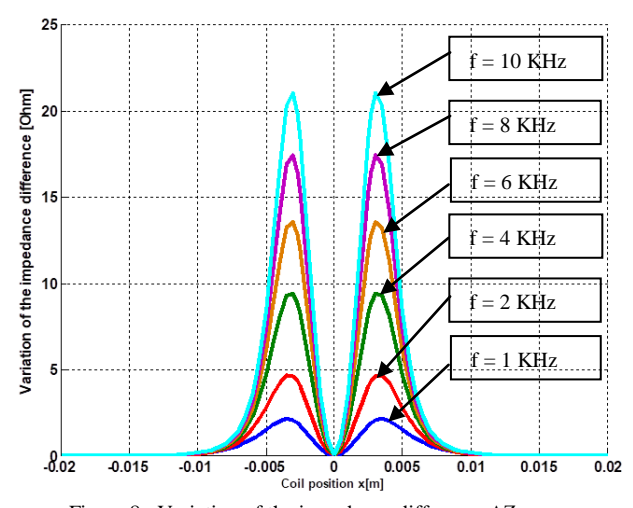


Figure 8: Variation of the impedance difference  $\Delta Z$  versus displacement of the coil center for f=1 KHz, f=2 KHz, f=4 KHz, f=6 KHz, f=8 KHz and f=10 KHz

We can notice that since the defect is very narrow, the impedance variation for x=0 is equal to zero, however it is maximum when the center of the coil is located at x=0.003m.

#### B. Effect of the electrical conductivity

Figure 9 gives the variation of the impedance difference  $\Delta Z$  for the electrical conductivity of Aluminium ( $\sigma=35.4*10^6$  S/m) and Copper ( $\sigma=59*10^6$  S/m).It can be seen that the amplitude of  $\Delta Z$  is proportional to the increase in electrical conductivity. The distance coil-plate is taken the same as the previous simulation.

In a material of high electrical conductivity, strong currents are generated on the surface, they produce a strong secondary magnetic field which opposes the primary magnetic field created by the coil.

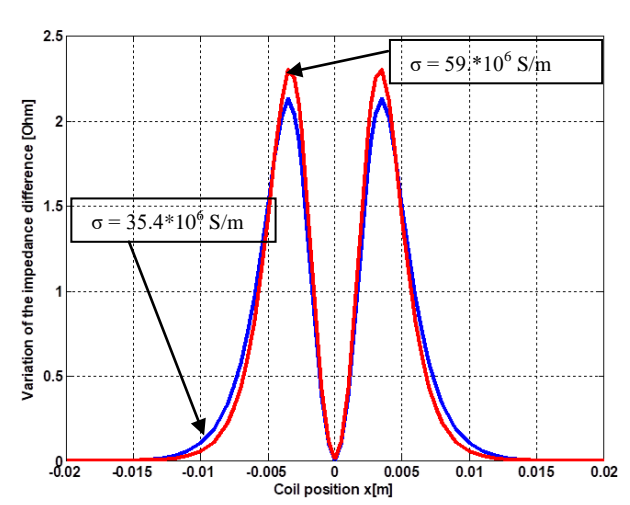


Figure 9: Variation of the impedance difference  $\Delta Z$  versus displacement of the coil center for  $\sigma = 59.*10^6$  S/m and  $\sigma = 35.4*10^6$  S/m

#### C. Effect of the lift-off

The lift-off is the distance between the coil and the tested piece. The goal of this simulation is to investigate how this distance affects the change of the difference impedance  $\Delta Z$ , for h=0.002m, h=0.004m, h=0.006m and h=0.008m. The electrical conductivity is  $35.4*10^6$  S/m.

The variation of the amplitude of the signal  $\Delta Z$  in figure 10, is inversely proportional with the increase of the lift-off. This is explained by the decrease of the electromagnetic coupling between the sensor and the plate to be inspected. The effect of the reverse field of the induced currents decreases with the increase of the lift-off.

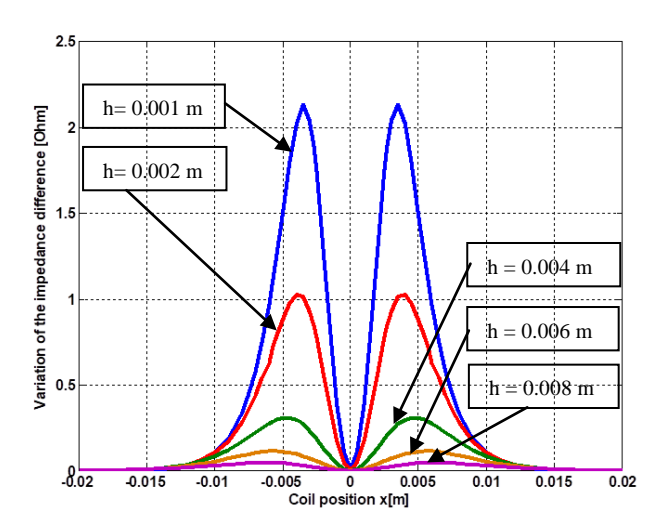


Figure 10: Variation of the impedance difference  $\Delta Z$  versus displacement of the coil center for h=0.001m, h=0.002m and h=0.004m, h=0.006m and h=0.008m

#### D. Effect of the position of the flaw

This last part is devoted to the study of the device when the flaw is on the backside of the plate, the new meshed configuration is shown in figure 11. The simulation is carried out for a frequency equal to 1000 Hz, an electrical conductivity of Aluminium and a lift-off equal to 0.001m.

Figure 12 shows that the detection signal becomes weaker when the flaw is located in the second face of the conductive plate, the sensor cannot be greatly influenced by the change in the distributions of the induced currents because of the distance between the flaw and the coil and because of the low intensity of the induced currents in the flaw.

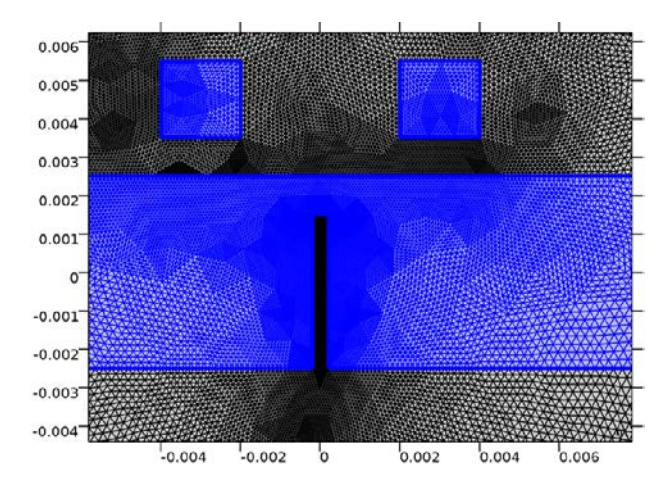


Figure 11: Refined mesh of the new geometry

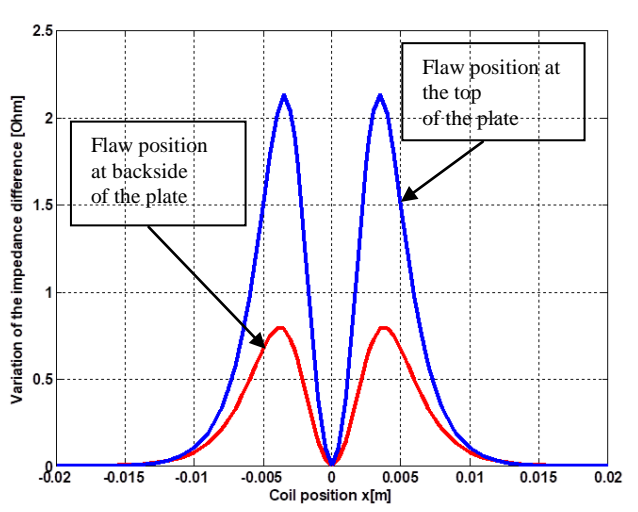


Figure 12: Variation of the impedance difference  $\Delta Z$  versus displacement of the coil center for two different positions of the flaw

#### IV. CONCLUSION

In this work a nondestructive testing with eddy current system comprising a long coil and a conductive plate is simulated. First, a 2D model based on the finite element method is implemented under COMSOL Multiphysics software. A quasi-static formulation is used to model the system, the use of the COMSOL Multiphysics software allowed to save computing resources in particular with regard to the computation time and the memory required for the simulations.

The simulation with free-flaw plate and with flaw under variation of the physical and geometric properties of the studied system let us to conclude the following points:

- The sensor is very sensitive to the increase in the excitation frequency and to the conductivity of the tested piece.
- The sensor loses its sensitivity when the sensor-target distance increases and when the position of the defect is located on the backside of the conductive part.
- The simulations revealed that the defect is detectable despite its fineness and depth, demonstrating the efficiency of the induced current approach in this type of issues.
- The mesh and number of discretization of coil displacements have a significant impact on the accuracy of the results and the smoothing of the impedance difference variation curves.

So, the sensor response is highly dependent on the working frequency, the conductivity of the part to be examined, the lift-off, and the location of the flaw.

The findings are consistent with previous scientific theories and study.

As future prospects we propose an experimental validation and investigation on inverse problem using obtained results.

#### REFERENCES

- [1] M. I. Silva, E. Malitckii, T. G. Santos, and P. Vilaça, "Review of conventional and advanced non-destructive testing techniques for detection and characterization of small-scale defects," *Prog. Mater. Sci.*, vol. 138, p. 101155, 2023.
- [2] Y. Zheng et al., "An ultrasonic nondestructive testing method for density uniformity of basin-type insulators in GIS," IEEE Trans. Instrum. Meas., vol. 70, pp. 1–8, 2021.
- [3] A. Lopez, R. Bacelar, I. Pires, T. G. Santos, J. P. Sousa, and L. Quintino, "Non-destructive testing application of radiography and ultrasound for wire and arc additive manufacturing," *Addit. Manuf.*, vol. 21, pp. 298–306, 2018.
- [4] J. García-Martín, J. Gómez-Gil, and E. Vázquez-Sánchez, "Non-destructive techniques based on eddy current testing," *Sensors*, vol. 11, no. 3, pp. 2525–2565, 2011.
- [5] A. I. Sacarea, G. Oancea, and L. Parv, "Magnetic particle inspection optimization solution within the frame of NDT 4.0," *Processes*, vol. 9, no. 6, p. 1067, 2021.
- [6] D. Karaduman, D. A. Bircan, and A. Çetin, "Non-Destructive examination of underground pressure vessels using acoustic emission (AE) techniques," *Eur. Mech. Sci.*, vol. 1, no. 1, pp. 1–8, 2017.
- [7] B. Feng, J. Wu, H. Tu, J. Tang, and Y. Kang, "A review of magnetic flux leakage nondestructive testing," *Materials* (*Basel*)., vol. 15, no. 20, p. 7362, 2022.
- [8] A. N. AbdAlla, M. A. Faraj, F. Samsuri, D. Rifai, K. Ali, and Y. Al-Douri, "Challenges in improving the performance of eddy current testing," *Meas. Control*, vol. 52, no. 1–2, pp. 46–64, 2019.
- [9] G. Tytko, W. Yin, Y. Luo, and M. Adamczyk-Habrajska, "Eddy Current Testing of Conductive Tubes With the Employment of the I-Core Sensor," *IEEE Access*, vol. 12, pp. 25525–25535, 2024.
- [10] P. Huang, H. Pu, J. Li, L. Xu, and Y. Xie, "An eddy current testing method for thickness and conductivity measurement of non-magnetic material," *IEEE Sens. J.*, vol. 23, no. 5, pp. 4445–4454, 2022.
- [11] Z. Ou, C. Xu, Z. Han, J. Cen, and S. Dong, "Nondestructive testing method for internal defects in ferromagnetic materials under weak bias magnetization," *Measurement*, vol. 226, p. 114173, 2024.
- [12] G. Y. Tian and A. Sophian, "Reduction of lift-off effects for pulsed eddy current NDT," NDT E Int., vol. 38, no. 4, pp. 319–324, 2005.
- [13] T. E. Capobianco, J. D. Splett, and H. K. Iyer, "Eddy current probe sensitivity as a function of coil construction parameters," *Res. Nondestruct. Eval.*, vol. 2, pp. 169–186, 1990.
- [14] M. Song, M. Li, S. Xiao, and J. Ren, "Research on the influence of geometric structure parameters of eddy current testing probe on sensor resolution," *Sensors*, vol. 23, no. 14, p. 6610, 2023.
- [15] W. Yoshimura, T. Sasayama, and K. Enpuku, "Optimal frequency of low-frequency eddy-current testing for detecting defects on the backside of thick steel plates," *IEEE Trans. Magn.*, vol. 55, no. 7, pp. 1–5, 2019.
- [16] R. Nagendran et al., "Optimum eddy current excitation frequency for subsurface defect detection in SQUID based non-destructive evaluation," NDT E Int., vol. 43, no. 8, pp. 713–717, 2010.
- [17] T. Theodoulidis and J. Bowler, "Eddy-current interaction of a long coil with a slot in a conductive plate," *IEEE Trans. Magn.*, vol. 41, no. 4, pp. 1238–1247, 2005.
- [18] N. O. Romero-Arismendi, J. C. Olivares-Galvan, J. L. Hernandez-Avila, R. Escarela-Perez, V. M. Jimenez-Mondragon, and F. Gonzalez-Montañez, "Past, Present, and Future of New Applications in Utilization of Eddy Currents," *Technologies*, vol. 12, no. 4, p. 50, 2024.
- [19] N. Ida, "Alternative approaches to the numerical calculation of impedance," NDT Int., vol. 21, no. 1, pp. 27–35, 1988.

# 2D Transient Calculation of the Step Voltage Distribution of a PV Power Plant

Benjamin Jauk\*, Robert Schürhuber\*, and Katrin Friedl\*

\*Institute of Electrical Power Systems, Inffeldgasse 18/1, A-8010 Graz E-mail: Benjamin.Jauk@TUGraz.at

Abstract—Transient calculation of the step voltage of large-scale ground mounted PV power plants is necessary in order to ensure personal safety in case of lighting strokes. Compared to traditional power plants, the earthing system of these PV plants is much larger and therefore causes an enhanced calculation effort. In this work we demonstrate an efficient way to calculate the transient step voltage of a large PV power plant using Fourier based methods.

Index Terms—Earthing Systems, Large PV Power Plant, Lightning, Transient Surface Potential

#### I. Introduction

The expansion of photovoltaics plays a key role in achieving climate targets. Large-scale PV systems in the mega-Watt range are currently being installed more and more frequently. These are not only located on the roofs of industrial buildings, but are increasingly being realised as ground-mounted systems. Rammed steel profiles are often used instead of conventional concrete foundations to enable these systems to be installed quickly and easily. These driven steel profiles perform like natural earth electrodes and can therefore contribute to the earthing system of the PV system. In this article we demonstrate a scheme to calculate the step voltage on the earth surface in the area of the PV system in two dimensions (2D). Compared to simulations performed in literature, where just a single "equivalent" frequency (e.g. 25 kHz) of the lightning stroke is considered [8], [9], or only a transient calculation of a straight line (1D) is performed [10], [11], [12], we calculate the step voltages in any direction in time domain (TD). The computational effort increases compared to simplified methods (e.g. one dimensional (1D)), but one can be sure that the highest potential gradient and thus the highest possible step voltage is found. This finally leads to a reliable interpretation of the results in terms of personal safety.

#### A. Lightning Protection System (LPS)

To ensure personal safety a lightning protection system (LPS) is used. The system contains measures to protect structures (e.g. buildings, generation units, etc.) or humans and livestock from the damaging effects of lightning strikes. Lightning protection systems are covered by the standard EN 62305-series (Part 1-4) [1], [2], [3]. This standard is applied for safety measures for buildings and livestock against harmful currents of lightnings. General aspects given in [1] for protection measures against electric shocks are:

- lightning protection system
- insulation of exposed bare conductors,
- equipotential bonding system by means of a meshed earthing system,

- physical restrictions and warnings,
- lightning equipotential bonding.

However, even if the lightning protection system is built properly according to the standard, in certain conditions the vicinity to conductors is known to cause hazardous potentials [3]. Such hazardous potentials can occur in the near field of bare conductors (e.g. earthing rods, construction) which carry lightning currents. Therefore several measures are mentioned to protect human beings and livestock. Beside these measures in the new version of IEC 62305 Part 3 2024 [4] a limit of  $25\,\mathrm{kV}$  (permissible step voltage,  $U_\mathrm{Sp}$ ) for the step voltage, with stride length of 1 m under an impulse current  $10/350~\mu\mathrm{s}$  (first positive stroke) is mentioned.

#### B. Prospective Step Voltage $(U_{vS})$

A definition of the term 'step voltage' is missing in [1]. However, according to [6], [7] this term is well defined. As depicted in Fig. 1 the prospective step voltage  $U_{\rm vS}$  is the potential difference of two points on the earth surface with stride length of 1 m, which is the potential difference of those two points of the surface potential  $\varphi$  not being touched. This means only one foot is touching the surface. The prospective step voltage does not take reducing factors e.g, shoes, surface covering layers, etc. into account. So, as depicted in Fig. 1 it can be seen, that in general  $U_{\rm vS} > U_{\rm S}$ . Since this definition is not made in IEC 62305-series, a reasonable assumption is to set  $U_{\rm vS}$  and not  $U_{\rm S}$  to the mentioned limit.

Therefore the limit mentioned in [4] is not exceeded, (1).

$$U_{\rm S} < U_{\rm vS} < U_{\rm Sp} = 25 \,\text{kV}$$
 (1)

The calculation of  $U_{\rm vS}$  is a conservative approach to check whether  $U_{\rm S}$  is below the permissible step voltage  $U_{\rm Sp}$ . Anyway,  $U_{\rm S}$  with the additional resistances ( $Z_{\rm shoe}$  and  $Z_{\rm cover}$  - Fig. 1) could be evaluated in accordance if needed.

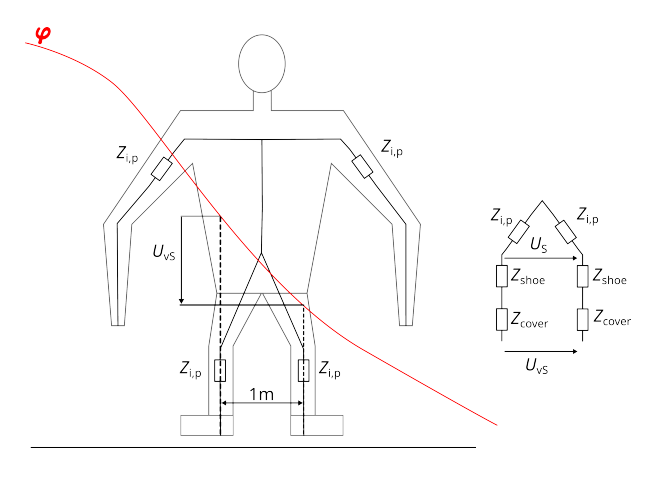


Fig. 1. Bodymodel [7] -  $\varphi$  is the surface potential,  $U_{\rm VS}$  is the prospective step voltage,  $U_{\rm S}$  is the step voltage and  $Z_i$  are the impedances (internal body impedances and additional external impedances)

In the following sections we demonstrate the calculation scheme of  $U_{\rm vS}$  for a transient lightning impulse propagating into a ground mounted PV system. We show the behaviour of  $U_{\rm vS}$  for two different scenarios:

- 1) The individual rows of modules are NOT connected to each other via an equipotential bonding wire,
- 2) the individual module rows are connected to each other via an equipotential bonding wire.

#### II. CALCULATION SCHEME

The transient current of the lightning strike is given by the so-called Heidler curve in equation (2), as defined in [1].

$$i(t) = \frac{I}{k} \cdot \frac{(t/\tau_1)^{10}}{1 + (t/\tau_1)^{10}} \cdot e^{-t/\tau_2}$$
 (2)

I is the peak value of the lightning impulse, k a correction factor,  $\tau_1$  is the front time and  $\tau_2$  is the decay time.

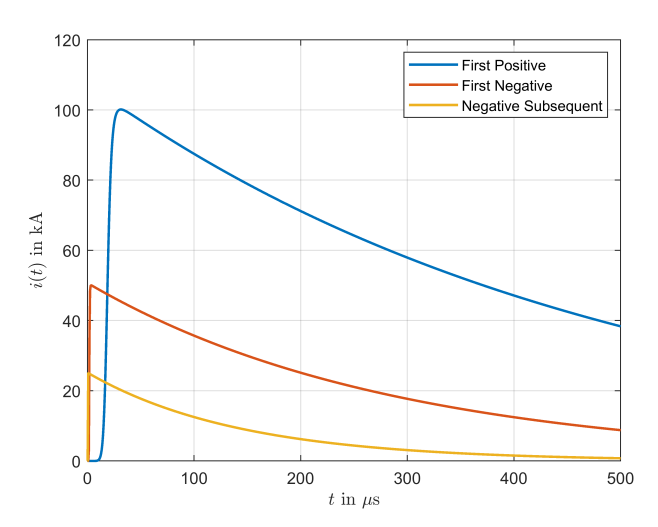


Fig. 2. Transient Currents in time domain (TD) for analytical purposes as presented in [1] for a lightning protection level (LPL) 3

The parameters  $k, \tau_1, \tau_2$  change whether a first positive, first negative or negative subsequent stroke [1] is analysed.

Fig. 2 depicts these three different lightning stroke time signals. To analyse the transient currents, the sampled current in time domain (TD) is transformed into frequency domain (FD) using discrete fourier transform (DFT), defined in (3).

$$X[\Omega] = \sum_{n=0}^{\infty} x[n]e^{-j\frac{\omega \cdot n}{f_{\rm S}}}, \Omega = \frac{\omega}{f_{\rm S}}$$
 (3)

Where  $X[\Omega]$  is the transformed signal x[n] and  $f_{\rm S}=\frac{1}{t_{\rm S}}=40\,{\rm MHz}$  the sample frequency. The calculation of the surface potential  $\varphi$  of the earth

The calculation of the surface potential  $\varphi$  of the earth surface around the ground mounted PV is calculated in frequency domain using a partial element equivalent circuit (PEEC) solver.

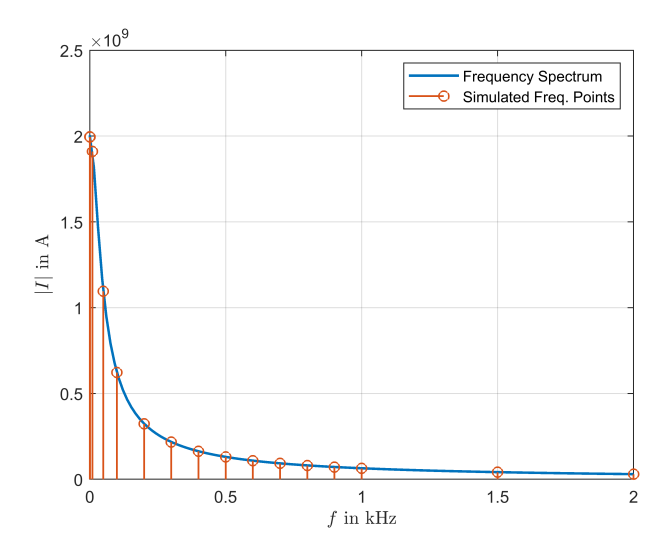


Fig. 3. FFT-Spectrum of the first positive stroke with  $100\,\mathrm{kA}$  (not normalized) - Sampled Frequency Spectrum (blue), at specific sample points simulated values (red) from  $0\,\mathrm{Hz}$  to  $2\,\mathrm{kHz}$ 

To reduce the computational effort, the full frequency spectrum is reduced to specific sampling points (167 [5]), as depicted in Fig. 3. This means the number of simulations needed to run by the Solver is reduced. The surface potential  $\varphi$  is calculated for each frequency sample (magnitude and corresponding frequency). The frequency spectrum of the surface potential is interpolated, using spline interpolation, to the full spectrum and the time domain (TD) representation is calculated applying the inverse FFT (IFFT).

From the full spectrum values of  $\varphi$ ,  $U_{vS}$  is calculated and analysed within the first  $500\,\mu s$  of the transient current.

## III. CALCULATION OF THE STEP VOLTAGE FROM THE SURFACE POTENTIAL

The surface potential  $\varphi$  is calculated in a  $1\,\mathrm{m}\times1\,\mathrm{m}$  grid. The calculation of the step voltage is done in each

grid point, as depicted in Fig. 4. The step voltage is the potential difference between two antipodal points of a circle with a radial distance of  $0.5\,\mathrm{m}$  from each grid point. This potential difference is calculated uniformly for 16 points over the half circumference of the circle, with the maximum value saved for this point. This procedure can be denoted as:

$$U_{\rm S} = \max\{U_{{\rm S},i}\}, i = [1, 2, ..., 16]$$
 (4)

$$U_{S,i} = \varphi'_{+,i} - \varphi'_{-,i} \tag{5}$$

Where  $U_{\rm S}$  is the calculated step voltage,  $U_{{\rm S},i}$  is the calculated step voltage of the *i*-th angle,  $\varphi'_{+,i}$  is the positive interpolated surface potential and  $\varphi'_{-,i}$  the negative / opposite potential. The interpolation of the surface potential between the grid points is performed by a linear interpolation.

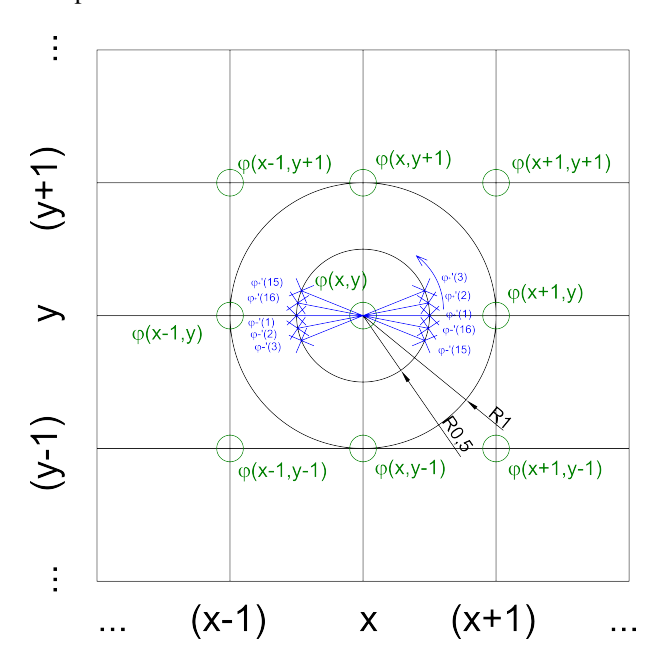


Fig. 4. Step Voltage Calculation Scheme - Calculation at grid point (x,y), with surface potential values  $(\varphi, green)$ , interpolated surface potential values  $(\varphi', blue)$ 

#### IV. VERIFICATION OF THE CALCULATION SCHEME

In order to verify the presented calculation procedure, the surface potential in a specific grid point is compared with a PEEC time domain solver. The input is the model and the transient current and the calculated result will be the time signal again. But it's only possible to calculate a line (1D). So the quantity of choice to compare, is the surface potential  $\varphi$ , as depicted in Fig. 5. Further, the interpolation to the reduced sampling points reduces the computational effort, but results in a lack of accuracy. Fig. 5 shows the surface potential at the selected grid point (X =45 m , Y =23 m), calculated with the time domain solver in blue, and the surface potential from the presented calculation procedure with 167 elements in red.

Although the peak value is slightly over estimated, the overall deviation in the result is minor, even the deviation in the tail is neglictable since the peak value is of interest. So it can be concluded that the presented procedure yields to meaningful results. The deviation of the peak is less than 2%.

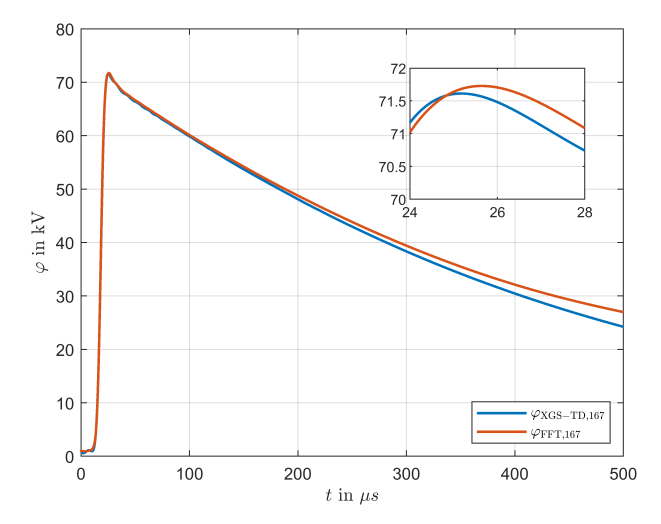


Fig. 5. Verification of the results. The red curve shows the results from the FFT calculation, compared to the blue curve which show the results using the time domain solver

#### V. PV POWER PLANT UNDER STUDY

The analysed ground-mounted PV system consists of four rows of modules, each with a length of 84 m, depicted in Fig. 6. The module rows are designed as single-foot, rammed steel tubes with a nominal diameter of 80 mm and a thickness of 5 mm (magenta). The ramming depth is 2 m. The horizontal PV rails consist of a squared aluminium tube with a side length of 60 mm and a wall thickness of 4 mm (black). The solver treats these tubes as round tubes, because the influence of whether the tube is round or square is marginal. The current-carrying capacity of the system depends mainly on the wall thickness (cross-sectional area). Two different scenarios are analysed:

- 1) The individual rows of modules are <u>not</u> connected to each other via an equipotential bonding wire,
- 2) the individual module rows are connected to each other with an equipotential bonding wire, with a diameter of 10 mm.

In the case where the module rows are connected with an equipotential bonding wire to each other (case 2), a  $10\,\mathrm{mm}$  stainless steel wire (green) is used. The wire is laid at a depth of 1 meter and buried.

The soil is considered frequency independent and homogeneous with a resistivity of  $\rho = 100 \,\Omega m$ ,  $\varepsilon_r = 6$ .

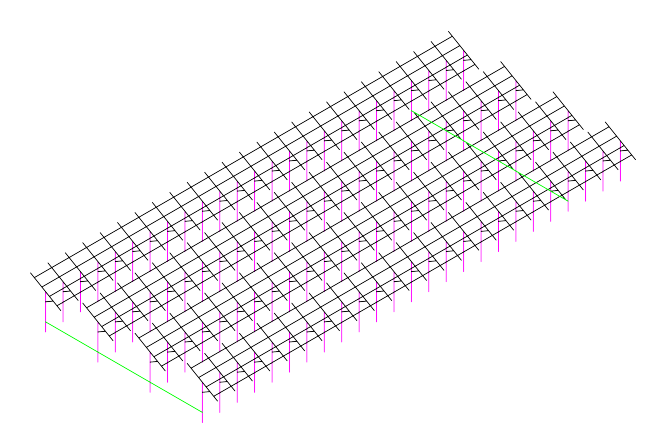


Fig. 6. Wire Frame Model of the ground mounted PV System (first half, 42 m of 84 m)

#### VI. RESULTS

Fig. 7 and 8 depict the maximum occurring step voltage for the first positive strike. It can be clearly seen that the equipotential bonding reduces the occurring potentials. In the case with no equipotential bonding installed (Fig. 7), the lightning current has to pass within one row of the given PV construction into earth, by flowing through the rammed profiles. The gradient of the surface potential is steep, resulting in high values of  $U_{\rm vS}$ , which can be seen in Fig. 7. The highest values occur right next to the rammed profiles. Compared to Fig. 8 where the equipotential bonding let the current pass to the whole structure.

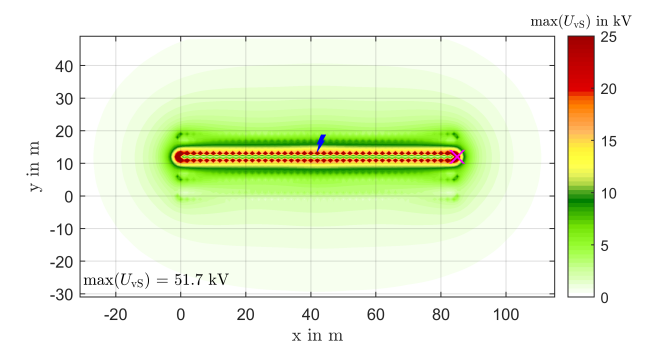


Fig. 7. Maximum Step voltage  $U_{vS}$  without equipotential bonding

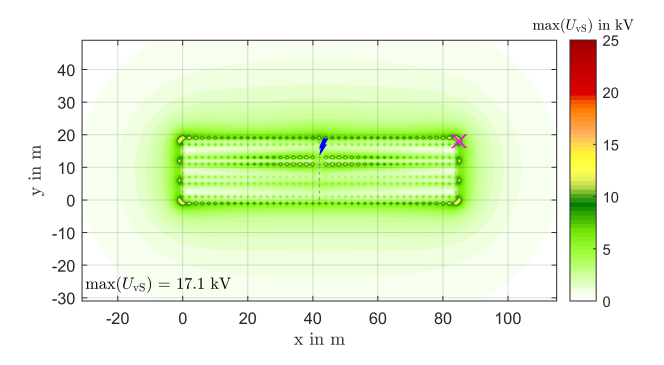


Fig. 8. Maximum Step Voltage  $U_{
m vS}$  with equipotential bonding

Fig. 9 depicts the time signals of the point with the maximum occurring  $U_{\rm vS}$  with equipotential bonding (Position equals to magenta cross in Fig. 8). Further the surface potentials  $\varphi$  of each grid point around this maximum is shown.

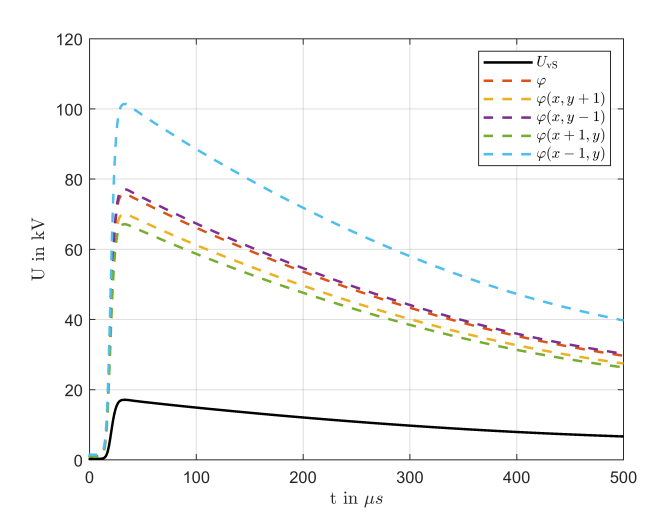


Fig. 9. Potential distribution of  $U_{\rm vS}$  and  $\varphi$  of the grid point with the occurring maximum and its surrounding grid points.

#### VII. CONCLUSION

The proposed method opens up the possibility to analyse the transient potentials on the earth surface in 2D for large earthing systems as for example large PV power plants and investigate the maximum occurring step voltages. So measures like an equipotential bonding system can be analysed for transient signals in order to verify safety measures.

For the PV power plant under study, an equipotential bonding system reduces the maximum prospective step voltage  $U_{\rm vS}$  below the limit of  $25\,\rm kV$  as demanded in [4]. Compared to low frequency steady state faults (e.g. power frequency, by the means of [6]), it can be seen, that the meshed system is not acting like a "equipotential surface" for transient signals and a travelling wave is distributing alongside the earthing system. This is a transient phenomena, which could be also seen, when plotting the time sets, when the maximum value occurs. As a next step for verification of the proposed method, measurements in a real-world ground mounted PV system are planned, also the frequency dependency of the soil resistance in the simulation will be implemented.

#### REFERENCES

- [1] "ÖVE/ÖNORM EN 62305-1 Protection against lightning Part 1: General principles", OVE 2012 "ÖVE/ÖNORM EN 62305-2 Protection against lightning – Part 2:
- Risk Management", OVE 2012
  "ÖVE/ÖNORM EN 62305-3 Protection against lightning Part 3:
- Physical damage to structures and life hazard", OVE 2013
- [4] "IEC 62305-3 Protection against lightning Part 3: Physical damage to structures and life hazard", IEC 2024
- [5] Sint Srl, "XGSLab User Guide"
- "OVE EN 50522 Earthing of power installations exceeding 1 kV a.c.", OVE 2023
- [7] "Effects of current on human beings and livestock Part 1: General Aspects", IEC 2018
- [8] "Lightning Protection and Safety Investigation in Livestock-Integrated Agrivoltaic Systems", Costa K., 37th International Conference on Lightning Protection 2024
- "Calculation of Lightning Effects in the Frequency Domain with a Program based on Hybrid Methods", Meppelink J., Andolfato R., Cuccarollo D., CIGRE International Colloquium on Lightning and Power Systems 2016
- [10] "Lightning transient characteristics of a 500-kV substation grounding grid", Tian, Chenghuan; Zhang, Yi; et. al., Institute of Electrical and Electronics Engineers, 2011 7th Asia-Pacific International Conference on Lightning
- [11] "Step and touch voltages near wind turbine grounding during lightning strokes" Markovski, B.; Grcev, L.; Arnautovski-Toseva, V., 2012 International Symposium on Electromagnetic
- [12] "Lightning Impact on Human Modeled by Network with Lumped Elements", Rock, Michael; Drebenstedt, Christian, 2022 36th International Conference on Lightning Protection

## Görges Polygon and Differential Leakage Coefficient of Polyphase Windings – Part 1 – Integer Slot Windings

Erich Schmidt, Member, IEEE, David A. Lackner Institute of Energy Systems and Electric Drives Vienna University of Technology, Vienna, Austria

Abstract - The paper presents an analytical evaluation of the differential leakage coefficient of polyphase integer slot windings for an arbitrary number of phases. The method considers in detail the geometry of the respective Görges polygon of such windings. For the geometric shape of these polygons, a distinction has to be made between full, short and long pitched windings. The number of edges is directly determined by the number of phases. However, the lengths of edges depend on the distribution of the winding zones along the circumference. The calculations are carried out both for full pitched as well as for pitched windings with normal and double zone spans. The proposed method is validated by means of several examples. In particular, they show the advantages of an increased number of phases.

Index Terms – Görges polygon, differential leakage coefficient, polyphase windings.

#### I. Introduction

Depending on the apparent power of synchronous and asynchronous machines, polyphase armature windings are usually of three-phase type and, more rarely, of two-phase or even of five-phase type. Sometimes, large inverter fed machines of these types are also equipped with two separate three-phase windings connected to individual converters. However, nowadays polyphase windings with a number of phases higher than three gain more and more interest. In particular, the automotive industry is developing related concepts.

All kinds of integer slot windings generate in general the fundamental wave along one pole pair but always also higher harmonics with wave lengths shorter than one pole pair. The Görges polygon and the differential leakage coefficient of such windings provide a measure of the harmonic content of the distribution of the magnetomotive force along the circumference [1]–[3].

The discussed analytical method based on the geometry of the respective Görges polygon of polyphase integer slot windings provides a significant simplification of the evaluation of the differential leakage coefficient. The geometric shape of these polygons depends on the number of phases and will be distinct between full, short and long pitched windings. With the presented approach, the magneto motive force (MMF) within the various slots is obtained directly from the distribution of the winding zones of either full pitch windings or pitched windings.

#### II. DISTRIBUTION OF PHASE ZONES

In order for the individual phase windings to work independently, odd and even numbers of phases have to be treated separately [3], [4]. The angular difference  $\alpha_{ph}$  between the  $m \geq 2$  phases with regard to both space along one pole pair as well as time is given by

odd number 
$$m: \alpha_{ph} = \frac{2\pi}{m}$$
, (1a)

even number 
$$m: \alpha_{ph} = \frac{\pi}{m}$$
. (1b)

The total number of slots and teeth Q and the number of Figs. 1b & 2b show the phase zones of full pitch double pole pairs p along the circumference define the number of

slots per pole pair  $Q/p \in \mathbb{N}$  as the product of twice the number of phases m and the number of slots per pole and phase  $q \in \mathbb{N}$ . Only with an odd number of phases, there are two different winding arrangements,

$$\frac{Q}{p} = 2 m q = \begin{cases} (2m) q, & \text{normal zone span} \\ m (2q), & \text{double zone span} \end{cases} .$$
 (2)

A winding with a normal zone span holds 2m zones with q slots along one pole pair, a winding with a double zone span holds m zones with 2q slots along one pole pair.

Integer slot windings with normal zone spans can be designed as either single layer or double layer windings for any number of phases. However, integer slot windings with double zone spans always require both an odd number of phases and double layer windings.

Figs. 1a & 2a show the phase zones of full pitch single layer windings with normal zone span. The number of phase zones along one pole pair is twice the number of phases m. The angular difference between the two zones of each phase is always equal to an angle of  $\pi$ . The MMF within each slot along the phase zones arises from only one phase current. Therefore, the MMF of each slot of a full pitch winding with normal zone span serves as a reference value for the MMF of the slots with all kinds of integer slot windings. The normalized MMF of each slot of a full pitch winding with normal zone span can be defined as  $|\hat{\underline{v}}_{Sk}| = 1, k = 1, 2, \dots, Q.$ 

On the other hand, each double layer winding has two zone rings which can be rotated against each other. The zone distribution of the layers always remains unaltered. but a full pitch winding is changed to a pitched winding [3], [4]. The classical parameters pitch  $\sigma$  and shortening  $\varepsilon$ 

$$\sigma = \frac{y_{\sigma}}{m \, q} \, , \quad 0 < \sigma < 2 \, , \tag{3a}$$

$$\varepsilon = \frac{y_{\varepsilon}}{m q} = \frac{m q - y_{\sigma}}{m q} , \quad 1 > \varepsilon > -1 ,$$
 (3b)

(1a)  $\sigma = 1$  or  $\varepsilon = 0$  represents a full pitch winding, are defined from the slot step  $y_{\sigma} \in \mathbb{N}$  and the number of slots per (1b) pole mq. Due to  $q \in \mathbb{N}$  and consequently  $mq \in \mathbb{N}$ , the shortening step  $y_{\varepsilon}$  always holds  $y_{\varepsilon} \in \mathbb{Z}$ .

layer windings with normal zone spans. Figs. 1cd) & 2cd

a)

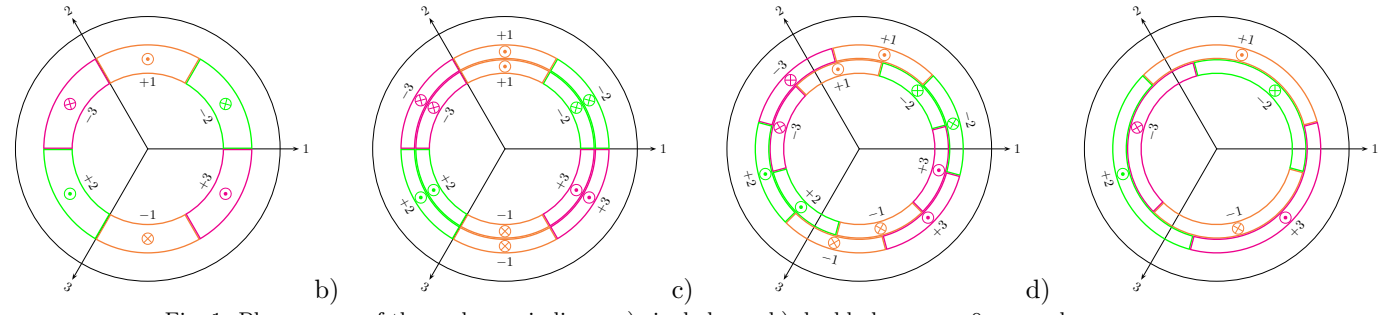


Fig. 1: Phase zones of three-phase windings: a) single layer; b) double layer  $\sigma=0$ , normal zone span; c) double layer  $\sigma=5/6$ , normal zone span; d) double layer  $\sigma=5/6$ , double zone span.

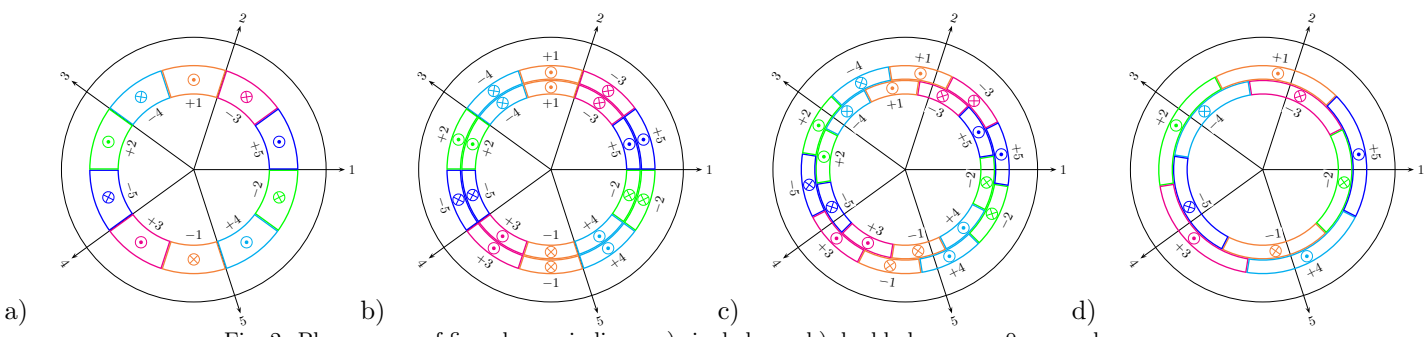


Fig. 2: Phase zones of five-phase windings: a) single layer; b) double layer  $\sigma=0$ , normal zone span; c) double layer  $\sigma=9/10$ , normal zone span; d) double layer  $\sigma=9/10$ , double zone span.

show the phase zones of pitched double layer windings with normal and double zone spans, respectively. The number of phase zones along one pole pair with a layer of normal zone span is always twice the number of phases m. However, the number of phase zones along one pole pair with a layer of double zone span is always equal to the number of phases m. Obviously, there are now two types of slots, depending on the pitch those with only one phase with their normalized MMF  $|\hat{y}_{Sk}| = 1$  and always those with two different phases with their normalized MMF  $|\hat{y}_{Sk}| < 1$ .

#### III. GÖRGES POLYGON

A Görges polygon gives a two-dimensional diagram of the distribution of the MMFs of slots  $\underline{\hat{v}}_S$  and teeth  $\underline{\hat{v}}_Q$  along the circumference [1]–[4]. The normalized MMF of each slot results from the distribution of zones and symmetric time-harmonic currents within each phase. Further, the MMF of each slot defines the difference of the MMFs of two adjacent teeth.

Based on the Kirchhoff law along all slots and the conservation of magnetic flux along all teeth, the MMFs of slots and teeth satisfy the equations

$$\sum_{k=1}^{Q} \underline{\hat{v}}_{Sk} = 0 , \quad \sum_{k=1}^{Q} \underline{\hat{v}}_{Qk} = 0 . \tag{4}$$

Hence, a Görges polygon along a base winding is always closed. In case of any integer slot winding, the Görges polygon is defined by the MMFs along only one base winding, i.e. only one pole pair.

Figs. 3a & 4a depict the Görges polygons of full pitch windings with normal zone span, see also Figs. 1ab & 2ab. These polygons are always the same for single and double layer windings. Figs. 3b & 4b and Figs. 3c & 4c depict the Görges polygons of pitched double layer windings with

normal zone span and double zone span, respectively, see also Figs. 1cd & 2cd. The pictures show the time phasors of the symmetric phase currents and the circle of the fundamental wave, too.

Assuming a normalized MMF of the slots of a full pitch winding with normal zone span as of  $|\hat{\underline{v}}_{Sk}| = 1$ , the geometry of the Görges polygon of any integer slot winding can be described in a very general form. For the geometric shape of these polygons, a distinction has to be made between full pitch windings as well as short and long pitched windings with their various pitching sections.

#### A. Full Pitch Windings

Fig. 5 shows the respective repetitive section of these polygons for full pitch windings with normal zone spans. The regular polygon of twice the number of phases can be described by the angles

$$2\alpha = \pi - \gamma \ , \quad \gamma = \frac{\pi}{m} \ , \tag{5}$$

and a length of each edge equal to the number of slots per pole and phase q, which defines

$$\cos \alpha = \frac{q}{2r_B} \ . \tag{6}$$

Hence, the circumscribed radius is given from

$$2r_P \sin \frac{\pi}{2m} = q . (7)$$

The MMF of each tooth k = 1, 2, ..., q, along one edge can be obtained by using the law of cosines from

$$|\hat{\underline{v}}_{Qk}|^2 = r_P^2 + k^2 - 2k r_P \cos \alpha . \tag{8}$$

Finally, the averaged square sum along all teeth is given by the values along one edge as

$$\frac{1}{Q} \sum_{k=1}^{Q} |\underline{\hat{v}}_{Qk}|^2 = \frac{1}{q} \sum_{k=1}^{q} |\underline{\hat{v}}_{Qk}|^2 = r_P^2 - \frac{q^2 - 1}{6} . \tag{9}$$

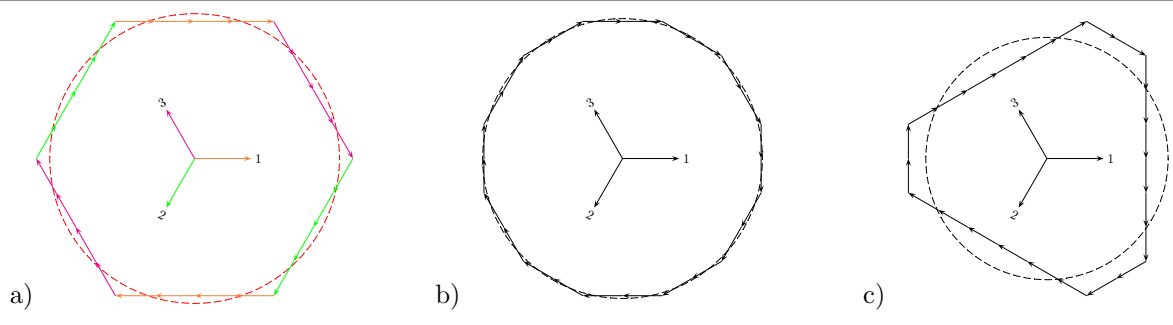


Fig. 3: Görges polygons of three-phase windings, q=4: a) full pitch, normal zone span; b) pitch  $\sigma=5/6$ , normal zone span; c) pitch  $\sigma=5/6$ , double zone span.

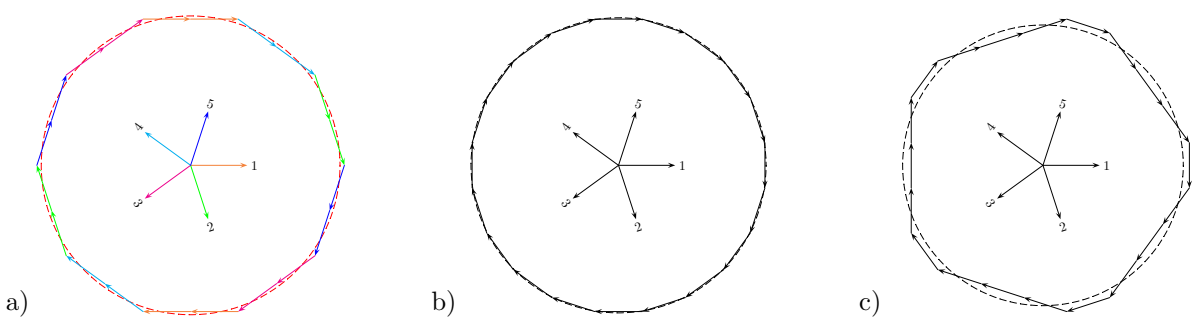


Fig. 4: Görges polygons of five-phase windings, q=2: a) full pitch, normal zone span; b) pitch  $\sigma=9/10$ , normal zone span; c) pitch  $\sigma=9/10$ , double zone span.

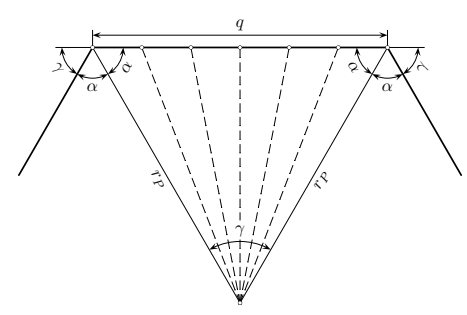


Fig. 5: Geometry of the Görges polygons, full pitch windings with normal zone span.

Fig. 6: Geometry of the Görges polygons, pitched windings with normal zone span or double zone span.

#### B. Pitched Windings

Fig. 6 shows the respective repetitive section of these polygons for pitched windings with normal or double zone spans. The inherent differences between the shape of these polygons will be determined by the exterior angle  $\gamma$  and the number of edges.

The polygon of a pitched winding with normal zone span holds a periodicity of twice the number of phases and in general a number of edges with four times the number of phases,

$$\alpha + \beta = \pi - \frac{\gamma}{2}$$
 ,  $\gamma = \frac{\pi}{m}$  . (10)

There are two edges  $e_{\alpha}$ ,  $e_{\beta}$  of different lengths with two numbers of slots or teeth  $n_{\alpha}$ ,  $n_{\beta}$ . The sum along the two edges is equal to the number of slots within one zone,  $n_{\alpha} + n_{\beta} = q$ . However, at any transition between two shortening sections (11), the polygon shows only a number of edges with twice the number of phases.

The  $l=1,2,\ldots,m$  sections with their various shortening values

$$\frac{l-1}{m} \le |\varepsilon_l| \le \frac{l}{m} , \quad l = 1, 2, \dots, m , \qquad (11)$$

determine the numbers  $n_{\alpha}, n_{\beta}$  of the slots along the two edges, the MMFs of the slots and hence the edge lengths  $e_{\alpha}, e_{\beta}$  as listed with Table I.

The relations

$$\cos \alpha = \frac{e_{\alpha}}{2 r_{Pl}} , \quad \cos \beta = \frac{e_{\beta}}{2 r_{Pl}} , \qquad (12)$$

allow for a closed calculation of the length  $r_{Pl}$  for each section. First, the angles  $\alpha, \beta, \gamma$  satisfy the relationship

$$\cos^2 \alpha + \cos^2 \beta + 2 \cos \alpha \cos \beta \cos \frac{\gamma}{2} = \sin^2 \frac{\gamma}{2} . \quad (13)$$

Hence, the circumscribed radius is given from

$$2 r_P \sin \frac{\gamma}{2} = \sqrt{e_\alpha^2 + e_\beta^2 + 2 e_\alpha e_\beta \cos \frac{\gamma}{2}}$$
 (14)

Finally, the averaged square sum along all teeth is given by the values along one repetitive section as

$$\frac{1}{Q} \sum_{k=1}^{Q} |\hat{\underline{v}}_{Qk}|^2 = \frac{1}{q} \sum_{k=1}^{q} |\hat{\underline{v}}_{Qk}|^2 = r_{Pl}^2$$

$$+ \frac{1}{q} \sum_{k=1}^{n_{\alpha}} \left( k^2 \cos^2 \frac{(l-1)\pi}{2m} - 2k \, r_{Pl} \cos \frac{(l-1)\pi}{2m} \cos \alpha \right)$$

$$+ \frac{1}{q} \sum_{k=1}^{n_{\beta}} \left( k^2 \cos^2 \frac{l\pi}{2m} - 2k \, r_{Pl} \cos \frac{l\pi}{2m} \cos \beta \right)$$
(15)

and after summation

$$\frac{1}{q} \sum_{k=1}^{q} |\hat{\underline{v}}_{Qk}|^2 = r_{Pl}^2 \tag{16}$$

$$-\frac{n_{\alpha} \left(n_{\alpha}^{2}-1\right) \cos ^{2} \frac{\left(l-1\right) \pi }{2 m}+n_{\beta} \left(n_{\beta}^{2}-1\right) \cos ^{2} \frac{l \pi }{2 m}}{6 \, q} \quad -\frac{n_{\alpha} \left(n_{\alpha}^{2}-1\right) \cos ^{2} \frac{\left(l-2\right) \pi }{2 m}+n_{\beta} \left(n_{\beta}^{2}-1\right) \cos ^{2} \frac{l \pi }{2 m}}{12 \, q}$$

The polygon of a pitched winding with double zone span holds a periodicity with the number of phases and in general a number of edges with twice the number of phases,

$$\alpha + \beta = \pi - \frac{\gamma}{2}$$
 ,  $\gamma = \frac{2\pi}{m}$  . (17)

There are two edges  $e_{\alpha}$ ,  $e_{\beta}$  of different lengths with two numbers of slots or teeth  $n_{\alpha}$ ,  $n_{\beta}$ . The sum along the two edges is equal to the number of slots within one zone,  $n_{\alpha} + n_{\beta} = 2q$ . However, at any transition between two shortening sections (18), the polygon shows only a number of edges with the number of phases.

The l = 1, 3, ..., m sections with their various shortening values

$$\frac{\max(0, l-2)}{m} \le |\varepsilon_l| \le \frac{l}{m} , \quad l = 1, 3, \dots, m , \quad (18)$$

determine the numbers  $n_{\alpha}, n_{\beta}$  of the slots along the two edges, the MMFs of the slots and hence the edge lengths  $e_{\alpha}, e_{\beta}$  as listed with Table II.

The circumscribed radius  $r_{Pl}$  for each section follows again from the relations Eq. (12),(13) and (14).

Finally, the averaged square sum along all teeth is given by the values along one repetitive section as

$$\frac{1}{Q} \sum_{k=1}^{Q} |\underline{\hat{v}}_{Qk}|^2 = \frac{1}{2q} \sum_{k=1}^{2q} |\underline{\hat{v}}_{Qk}|^2 = r_{Pl}^2$$

$$+ \frac{1}{2q} \sum_{k=1}^{n_{\alpha}} \left( k^2 \cos^2 \frac{(l-2)\pi}{2m} - 2k \, r_{Pl} \cos \frac{(l-2)\pi}{2m} \cos \alpha \right)$$

$$+ \frac{1}{2q} \sum_{k=1}^{n_{\beta}} \left( k^2 \cos^2 \frac{l\pi}{2m} - 2k \, r_{Pl} \cos \frac{l\pi}{2m} \cos \beta \right)$$
(19)

and after summation

$$\frac{1}{2q} \sum_{k=1}^{2q} |\hat{\underline{v}}_{Qk}|^2 = r_{Pl}^2 \tag{20}$$

It should be explicitly mentioned that in the shortening section l=m with both normal and double zone windings there are always slots with a normalized MMF  $\underline{\hat{v}}_{Sk}=0$ . As given with Table I and Table II, the edges  $e_{\beta}$  show a zero length with this shortening section.

#### IV. VALIDATION AGAINST LITERATURE

Among others, Liwschitz [5] and Richter [2] in particular have shown some results from the Görges polygons of full and short pitched windings with phase numbers of m=2 and m=3.

#### A. Full Pitch Windings

Based on Eq. (7), (9), the special cases of m=2 and m=3 show the results

$$r_P \Big|_{m=2} = \frac{q}{\sqrt{2}} , \frac{1}{q} \sum_{k=1}^{q} |\hat{\underline{v}}_{Qk}|^2 \Big|_{m=2} = \frac{2q^2 + 1}{6} , \quad (21a)$$

$$r_P \Big|_{m=3} = q$$
,  $\frac{1}{q} \sum_{k=1}^{q} |\hat{\underline{v}}_{Qk}|^2 \Big|_{m=3} = \frac{5q^2 + 1}{6}$ , (21b)

which are in full accordance with the original values derived in [2], [5].

#### B. Pitched Windings

Based on Eq. (14),(16) and Table I, the shortening section 1 of pitched two-phase windings with normal zone spans is described with

$$r_{P1}^2 = \frac{1}{4} \left( 2 q^2 - 2 q |y_{\varepsilon}| + y_{\varepsilon}^2 \right) , \quad 0 \le |y_{\varepsilon}| \le q , \quad (22)$$

hence finally

(20) 
$$\frac{1}{q} \sum_{k=1}^{q} |\hat{\underline{v}}_{Qk}|^2 = \frac{2q^2 + 1}{6} + \frac{|y_{\varepsilon}|}{12q} \left( y_{\varepsilon}^2 - 3q |y_{\varepsilon}| - 1 \right) , \quad (23)$$

 ${\bf TABLE~I}$  Pitch sections of pitched windings with normal zone span.

Section	Step $ y_{\varepsilon} $	Number $n_{\alpha}$	Number $n_{\beta}$	Edge $e_{\alpha}$	Edge $e_{\beta}$
1	$0 \le \frac{ y_{\varepsilon} }{q} \le 1$	$q- y_{arepsilon} $	$ y_arepsilon $	$n_{lpha}$	$n_{\beta} \cos \frac{\pi}{2m}$
2	$1 \le \frac{ y_{\varepsilon} }{q} \le 2$	$2q -  y_{\varepsilon} $	$ y_{arepsilon} -q$	$n_{\alpha} \cos \frac{\pi}{2m}$	$n_{\beta} \cos \frac{2\pi}{2m}$
3	$2 \le \frac{ y_{\varepsilon} }{q} \le 3$	$3q -  y_{\varepsilon} $	$ y_{arepsilon}  - 2q$	$n_{\alpha} \cos \frac{2\pi}{2m}$	$n_{\beta} \cos \frac{3\pi}{2m}$
l	$l-1 \le \frac{ y_{\varepsilon} }{q} \le l$	$l q -  y_{\varepsilon} $	$ y_{\varepsilon}  - (l-1)q$	$n_{\alpha} \cos \frac{(l-1)\pi}{2m}$	$n_{\beta} \cos \frac{l\pi}{2m}$

TABLE II
PITCH SECTIONS OF PITCHED WINDINGS WITH DOUBLE ZONE SPAN.

Section	Step $ y_{\varepsilon} $	Number $n_{\alpha}$	Number $n_{\beta}$	Edge $e_{\alpha}$	Edge $e_{\beta}$
1	$0 \le \frac{ y_{\varepsilon} }{q} \le 1$	$q- y_{arepsilon} $	$ y_{arepsilon}  + q$	$n_{\alpha} \cos \frac{\pi}{2m}$	$n_{\beta} \cos \frac{\pi}{2m}$
3	$1 \le \frac{ y_{\varepsilon} }{q} \le 3$	$3q -  y_{\varepsilon} $	$ y_{arepsilon} -q$	$n_{\alpha} \cos \frac{\pi}{2m}$	$n_{\beta} \cos \frac{3\pi}{2m}$
l	$l-2 \le \frac{ y_{\varepsilon} }{q} \le l$	$l  q -  y_{arepsilon} $	$ y_{\varepsilon}  - (l-2) q$	$n_{\alpha} \cos \frac{(l-2)\pi}{2m}$	$n_{\beta} \cos \frac{l\pi}{2m}$

which is in full accordance with the original value derived in [5].

Based on Eq. (14),(16) and Table I, the shortening sections 1&2 of pitched three-phase windings with normal zone spans are described with

$$r_{P1}^2 = \frac{1}{4} \left( 4 q^2 - 2 q |y_{\varepsilon}| + y_{\varepsilon}^2 \right) , \quad 0 \le |y_{\varepsilon}| \le q , \quad (24a)$$

$$r_{P2}^2 = \frac{1}{4} \left( 7 q^2 - 5 q |y_{\varepsilon}| + y_{\varepsilon}^2 \right) , \quad q \le |y_{\varepsilon}| \le 2q , \quad (24b)$$

hence finally within section 1,  $0 \le |y_{\varepsilon}| \le q$ ,

$$\frac{1}{q} \sum_{k=1}^{q} |\hat{\underline{v}}_{Qk}|^2 = \frac{5q^2 + 1}{6} + \frac{|y_{\varepsilon}|}{24q} \left( y_{\varepsilon}^2 - 6q |y_{\varepsilon}| - 1 \right) , (25a)$$

and within section 2,  $q \leq |y_{\varepsilon}| \leq 2q$ ,

$$\frac{1}{q} \sum_{k=1}^{q} |\hat{\underline{v}}_{Qk}|^2 = \frac{5q^2 + 1}{8}$$
 (26a)

$$+\frac{|y_{\varepsilon}|-q}{24 q} \left(2 \left(|y_{\varepsilon}|-q\right)^2-3 q \left(|y_{\varepsilon}|-q\right)-9 q^2-2\right) ,$$

which are in full accordance with the original values derived in [2], [5].

#### V. DIFFERENTIAL LEAKAGE COEFFICIENT

The deviation of a Görges polygon from the circular shape corresponding to the fundamental wave provides a measure of the harmonic content of the circumferential distribution of the magnetomotive force of a polyphase armature winding. As already given in [1]–[4], [6], [7] with non-normalized values, the differential leakage coefficient  $\sigma_o$  can be obtained from the averaged square sum of the MMFs along all teeth and the winding factor  $\xi_1$  of the fundamental wave along one pole pair.

Based on the normalized MMF of the slots  $|\underline{\hat{v}}_{Sk}|$  and the normalized MMF of the teeth  $\underline{\hat{v}}_{Qk}$ , the differential leakage coefficient can be evaluated from

$$1 + \sigma_o = \left(\frac{\pi}{mq}\right)^2 \frac{1}{\xi_1^2 Q} \sum_{k=1}^{Q} |\hat{\underline{v}}_{Qk}|^2 . \tag{27}$$

#### A. Full Pitch Windings

Table III lists the winding factor of the fundamental wave and the differential leakage coefficient for various full pitch

windings with normal zone spans. Particular interest lies on those pairs of windings with different numbers of phases but a fixed number of slots per pole mq and thus an unchanged number of coils. Obviously, the higher number of phases always yields an increased winding factor of the fundamental wave  $\xi_1$  as well as a reduced differential leakage coefficient  $\sigma_o$ .

With any odd number of phases, the differential leakage coefficient will be equal between full pitch windings with normal and double zone spans. On the one hand, the distribution factors of the fundamental wave with normal and double zone spans

$$\xi_{2m,d1} = \frac{\sin\frac{\pi}{2m}}{q\sin\frac{\pi}{2ma}}, \quad \xi_{m,d1} = \frac{\sin\frac{\pi}{m}}{2q\sin\frac{\pi}{2ma}},$$
 (28a)

always hold

$$\xi_{m,d1} = \xi_{2m,d1} \cos \frac{\pi}{2m}$$
 (28b)

On the other hand, the numbers  $n_{\alpha}, n_{\beta}$  are equal and the edges  $e_{\alpha}, e_{\beta}$  have the same length, see Table II. However, these lengths are shortened by the factor  $\cos(\pi/(2m))$  against the length of the edge  $e_{\alpha}$  of a full pitch winding with normal zone spans, see Table I. Consequently, the differential leakage coefficient (27) remains unchanged.

#### B. Pitched Windings

Fig. 7 and Fig. 8 show the differential leakage coefficient  $\sigma_o$  of pitched windings with normal zone spans for the number of phases m=3 and m=5 in dependence on the number of slots per pole and phase  $q\geq 2$  and the shortening step  $|y_\varepsilon|$ . The differential leakage coefficients of concentrated windings q=1 with a step  $0\leq |y_\varepsilon|< mq$  are always equal to those of full pitched windings, see Table III.

As already listed for full pitch windings, the higher number of phases together with a number of slots per pole phase  $q \geq 2$  always yields a reduced differential leakage coefficient  $\sigma_{o}$ .

#### C. Pitched Windings, Comparison of Designs

As an example, the changeover of an inverted fed asynchronous machine with a rated power of 1.8 MVA, a

TABLE III
FUNDAMENTAL WINDING FACTOR AND DIFFERENTIAL LEAKAGE COEFFICIENT, FULL PITCH WINDINGS, NORMAL ZONE SPAN.

Number of	Winding	Number of slots per pole and phase										
phases $m$	parameter	q = 1	q = 2	q = 3	q = 4	q = 5	q = 6	q = 7	q = 8			
9	$\xi_1$	1.000000	0.923880	0.910684	0.906127	0.904029	0.902893	0.902208	0.901764			
2	$\sigma_o$	0.233701	0.084028	0.046802	0.033008	0.026487	0.022908	0.020738	0.019324			
9	$\xi_1$	1.000000	0.965926	0.959795	0.957662	0.956677	0.956143	0.955821	0.955612			
3	$\sigma_o$	0.096623	0.028437	0.014061	0.008896	0.006481	0.005163	0.004366	0.003848			
F	$\xi_1$	1.000000	0.987688	0.985432	0.984644	0.984279	0.984081	0.983962	0.983885			
5	$\sigma_o$	0.033558	0.008900	0.004115	0.002424	0.001639	0.001211	0.000953	0.000786			
7	$\xi_1$	1.000000	0.993712	0.992554	0.992149	0.991962	0.991860	0.991798	0.991759			
1	$\sigma_o$	0.016955	0.004369	0.001982	0.001142	0.000752	0.000541	0.000413	0.000330			
0	$\xi_1$	1.000000	0.996195	0.995492	0.995247	0.995133	0.995071	0.995034	0.995010			
9	$\sigma_o$	0.010216	0.002601	0.001170	0.000668	0.000435	0.000309	0.000233	0.000183			

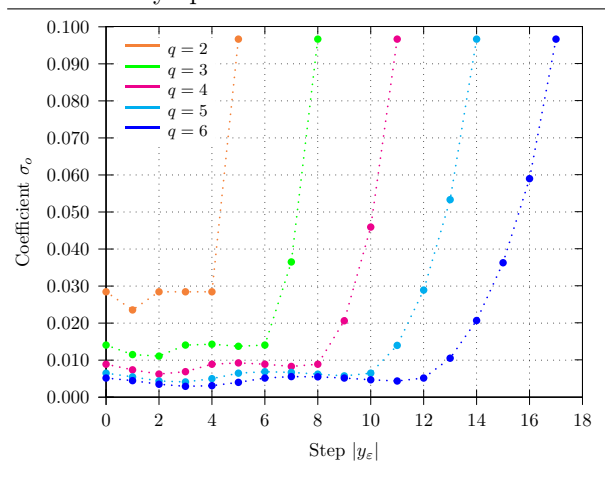


Fig. 7: Differential leakage coefficient of pitched windings with normal zone spans, m=3.

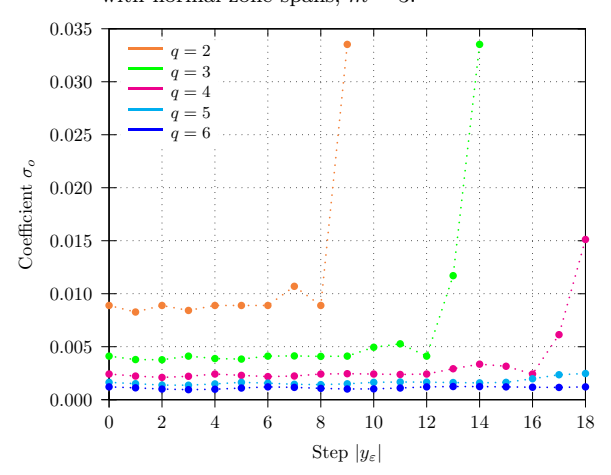


Fig. 8: Differential leakage coefficient of pitched windings with normal zone spans, m = 5.

number of poles 2p=4 and a number of stator slots Q=60 is discussed. The armature winding has the number Q/p=2mq=30 of slots per pole pair. Thus, a number of phases m=3 yields the number of slots per pole and phase  $q=5\in\mathbb{N}$ . Moreover, a number of phases m=5 yields the number of slots per pole and phase  $q=3\in\mathbb{N}$ .

Table IV lists the fundamental winding factors and the differential leakage coefficients of the two windings with a shortening range  $0 \le |\varepsilon| \le 1/3$  for both normal and double zone spans.

From a practical point of view, the windings with normal zone spans are more important. The differential leakage coefficient  $\sigma_o$  of the winding with five phases decreases by up to 30% depending on the shortening. The winding with five phases shows an increased fundamental winding factor  $\xi_1$  of approximately 3%.

However, the differences between the two windings are more noticeable with double zone spans. The differential leakage coefficient  $\sigma_o$  of the winding with five phases decreases by 30% up to 90% depending on the shortening. The winding with five phases shows an increased fundamental winding factor  $\xi_1$  of approximately 12%.

With both arrangements of normal and double zone spans, the electromagnetic torque of the fundamental waves will be higher to the same extent as the fundamental winding factor while the power and iron losses remain constant.

#### VI. CONCLUSION

The paper presents a detailed discussion of the geometry of the Görges polygon of integer slot windings with an arbitrary number of phases. Full pitch and pitched windings with normal as well as double zone spans are analyzed in order to evaluate the differential leakage coefficient by an analytical method. Thereby, the complete range of the pitch sections of such windings is shown in detail for the first time.

In particular, a higher number of phases provides an improved behaviour of an integer slot winding even with an unchanged number of coils. This is shown in detail using an example with practically existing machines.

The presented approach allows for an easy to use and fast implementation into the design process and an optimization of polyphase windings with an arbitrary number of phases.

#### References

- Sequenz H.: Die Wicklungen elektrischer Maschinen, Band I, Springer Verlag, Wien, 1950.
- [2] Richter R.: Elektrische Maschinen, Band IV, Birkhäuser Verlag, Basel/Stuttgart, 1954.
- [3] Müller G., Vogt K., Ponick B.: Berechnung elektrischer Maschinen, Wiley-VCH Verlag, Weinheim, 2008.
- [4] Pyrhönen J., Jokinen T., Hrabovcová V.: Design of Rotating Electrical Machines, John Wiley & Sons Ltd, 2008.
- [5] Liwschitz M.M.: "Differential Leakage with Respect to the Fundamental Wave and to the Harmonics." Electrical Engineering, Vol. 63, No. 12, Dec 1944.
- [6] Caruso M., Di Tommaso A.O., Marignetti F., Miceli R., Ricco Galluzzo G.: "A General Procedure for the Construction of Görges Polygons for Multiphase Windings of Electrical Machines." Proceedings of the IEEE International Conference on Ecological Vehicles and Renewable Energies (EVER 2018), Monte Carlo (Monaco), Apr 2018.
- [7] Caruso M., Di Tommaso A.O., Genduso F., Miceli R., Ricco Galluzzo G.: "A General Mathematical Formulation for the Determination of Differential Leakage Factors in Electrical Machines With Symmetrical and Asymmetrical Full or Dead-Coil Multiphase Windings." *IEEE Transactions on Industry Appli*cations, Vol. 54, No. 6, Nov/Dec 2018.

TABLE IV
COMPARISON OF PITCHED WINDINGS, DIFFERENT NUMBER OF PHASES.

		Normal z	one span		Double zone span					
$\operatorname{Shortening}_{\operatorname{step}}  y_{\varepsilon} $	m =	= 3	m =	= 5	m	= 3	m = 5			
500P  9E	$\xi_1$	$\sigma_o$	$\xi_1$	$\sigma_o$	$\xi_1$	$\sigma_o$	$\xi_1$	$\sigma_o$		
0	0.956677	0.006481	0.985432	0.004115	0.828507	0.006481	0.937201	0.004115		
1	0.951436	0.005485	0.980033	0.003790	0.823968	0.009523	0.932067	0.004995		
2	0.935772	0.004366	0.963898	0.003772	0.810402	0.018559	0.916721	0.007253		
3	0.909854	0.004114	0.937201	0.004115	0.787957	0.033257	0.891331	0.009619		
4	0.873968	0.004995	0.900237	0.003885	0.756879	0.052852	0.856176	0.009513		
5	0.828507	0.006481	0.853409	0.003835	0.717508	0.075710	0.811640	0.008336		

# Görges Polygon and Differential Leakage Coefficient of Polyphase Windings – Part 2 – Fractional Slot Windings

Erich Schmidt, Member, IEEE, David A. Lackner

Institute of Energy Systems and Electric Drives Vienna University of Technology, Vienna, Austria

Abstract – The paper presents an algorithmic evaluation of the differential leakage coefficient of polyphase fractional slot windings for an arbitrary number of phases. The procedure relies directly on the respective Görges polygon of such windings. The calculations are carried out for windings with normal and double zone spans. In particular, all kinds of tooth-coil windings can be analyzed. The proposed method is validated by means of several examples.

Index Terms - Görges polygon, differential leakage coefficient, polyphase windings, tooth-coil windings.

#### I. Introduction

Depending on the apparent power of synchronous and asynchronous machines, polyphase armature windings are usually of three-phase type and, more rarely, of two-phase or even of five-phase type. Sometimes, large inverter fed machines of these types are also equipped with two separate three-phase windings connected to individual converters. However, nowadays polyphase windings with a number of phases higher than three gain more and more interest. In particular, the inverter fed generators of wind power units offer this degree of freedom in the design of their integer or fractional slot windings.

All kinds of fractional slot windings generate in general the fundamental wave along one pole pair but always also higher harmonics with wave lengths shorter than one pole pair and usually also subharmonics with wave lengths longer than one pole pair. In particular, the subharmonics occur with many kinds of tooth-coil windings, sometimes named as fractional slot concentrated windings. The Görges polygon and the differential leakage coefficient of such windings provide a measure of the harmonic content of the distribution of the magnetomotive force along the circumference [1]–[3].

The discussed algorithmic method based on the geometry of the respective Görges polygon of polyphase fractional slot windings provides a significant simplification of the evaluation of the differential leakage coefficient. The geometric shape of these polygons depends on the number of phases as well as the number of pole pairs necessary for the base winding. With the presented approach, the magneto motive force (MMF) within the various slots will be obtained from the distribution of the winding zones by using the corresponding Tingley plan. In addition, a Fourier analysis of the MMF along the slots of one base winding will be applied in order to evaluate the winding factors of particularly the subharmonics.

### II. Symmetry Conditions and Distribution of Phase Zones

In order for the individual phase windings to work independently, odd and even numbers of phases have to be treated separately [3], [4]. The angular difference  $\alpha_{ph}$  between the  $m \geq 2$  phases with regard to both space along

one pole pair as well as time is given by

odd number 
$$m: \alpha_{ph} = \frac{2\pi}{m}$$
, (1a)

even number 
$$m: \alpha_{ph} = \frac{\pi}{m}$$
. (1b)

The winding zones of integer slot windings satisfy this angular difference within in each pole pair. However, the winding zones of fractional slot windings comply with this angular difference in general along more than one pole pair.

The total number of slots and teeth Q and the number of pole pairs p along the circumference define the number of slots per pole and phase

$$q = \frac{Q}{2 p m} = \frac{q_n}{q_d} = q_i + \frac{q_p}{q_d} ,$$

$$\gcd(q_n, q_d) = \gcd(q_p, q_d) = 1 .$$
(2)

Herein,  $q_i \in \mathbb{N}_0$  denotes the integer part of the fraction,  $q_n \in \mathbb{N}$  and  $q_p \in \mathbb{N}$  the numerator of the improper and proper fraction, respectively, and  $q_d \in \mathbb{N}$  the denominator of the fraction. In particular, tooth-coil windings always show an integer part  $q_i = 0$ .

A symmetry of the phases enforces necessary conditions for the total number of slots Q and the number of slots per pole and phase  $q \notin \mathbb{N}$  as given in Table I. These conditions also define the number of repetitive sections of the slots  $t = \gcd(Q,p)$  along the circumference and the number of repetitive sections of the slots necessary for an entire base winding  $t^*$  as listed in Table II.

Fractional slot windings with an odd number  $q_d$  are called first kind, with an even number  $q_d$  second kind [3], [4]. In order to create a fundamental wave along one pole pair,  $gcd(q_d, m) = 1$  must be fulfilled, too. Consequently, fractional slot windings of the second kind are possible for an odd number of phases only.

Therefore, an integer slot winding holds a base winding along each pole pair. A fractional slot winding of first kind shows a base winding along a number  $q_d \in \mathbb{N}_{\text{odd}}$  of pole pairs. A double layer fractional slot winding of second kind has a base winding along a number  $q_d/2$  of pole pairs, a single layer winding again along a number  $q_d \in \mathbb{N}_{\text{even}}$  of pole pairs, see Table II.

TABLE I Symmetry conditions of fractional slot windings

	Single layer windings	Double layer windings
Number of slots	$\frac{Q}{2m} \in \mathbb{N}$	$\frac{Q}{m} \in \mathbb{N}$
Number of slots per pole and phase	$\frac{p}{q_d} \in \mathbb{N}$	$\frac{2p}{q_d} \in \mathbb{N}$

 ${\bf TABLE~II}$  Repetitive sections of slots and base windings.

Winding	Repetitive	Repetitive sections per base winding				
type	slot sections	Single layer	Double layer			
$q\in\mathbb{N}$	$t=p\in\mathbb{N}$	$t^* = 1$	$t^* = 1$			
$q_d \in \mathbb{N}_{\mathrm{odd}}$	$t = \frac{p}{q_d} \in \mathbb{N}$	$t^* = 1$	$t^* = 1$			
$q_d \in \mathbb{N}_{\text{even}}$	$t = \frac{2p}{q_d} \in \mathbb{N}$	$t^* = 2$	$t^* = 1$			

As usual, the parameters pitch  $\sigma$  and shortening  $\varepsilon$ 

$$\sigma = \frac{y_{\sigma}}{m \, q} \quad , \quad 0 < \sigma < 2 \quad , \tag{3a}$$

$$\varepsilon = \frac{y_{\varepsilon}}{m \, q} = \frac{m \, q - y_{\sigma}}{m \, q} \, , \quad 1 > \varepsilon > -1 \, ,$$
 (3b)

 $\sigma=1$  or  $\varepsilon=0$  represents a full pitch winding, are defined from the slot step  $y_{\sigma}\in\mathbb{N}$  and the number of slots per pole mq. Due to  $q\notin\mathbb{N}$  and consequently  $mq\notin\mathbb{N}$ , a full pitch winding is impossible now, all kinds of fractional slot windings are pitched.

#### III. VOLTAGE PHASOR DIAGRAM, TINGLEY PLAN

On the one hand, the design of a fractional slot winding can be done from the phasor diagram of the voltages assigned to each slot of a base winding [1]–[4]. On the other hand, the Tingley plan shows a linear representation of the slots along the base winding [1], [2]. With both design tools, the phase difference between two adjacent slots is given by the slot angle  $\alpha_Q = \pi/(mq)$ .

A voltage phasor diagram of a complete winding shows a periodicity according to the number of repetitive slot sections. The number of full cycles is given by the number of pole pairs of each repetitive slot section, e.g. see Fig. 1.

A Tingley plan consists of a number of poles as given by the base winding. Thereby, the slots along the base winding are arranged according to their angle  $\alpha_Q$ , e.g. see Fig. 2 and Fig. 3.

Sequenz [1] gives a natural arrangement for the coil groups of lap windings. An entire or equivalent parts of the base winding consists of  $(q_d - q_p)$  groups with  $q_i$  coils and  $q_p$  groups with  $(q_i + 1)$  coils, in summary  $(q_i q_d + q_p)$  coils within  $q_d$  groups. The average number of coils within the  $q_d$  groups

$$\frac{\left(q_d - q_p\right)q_i + q_p\left(q_i + 1\right)}{q_d} = \frac{q_i q_d + q_p}{q_d} \tag{4}$$

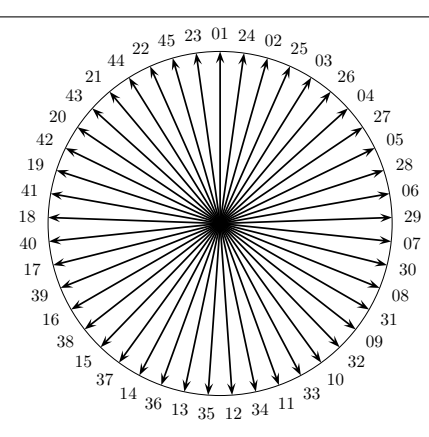


Fig. 1: Voltage phasor diagram of a fractional slot winding, number of slots Q=45, number of poles 2p=4,  $m=3,\ q=15/4$  or  $m=5,\ q=9/4,\ \alpha_Q=16$  deg.

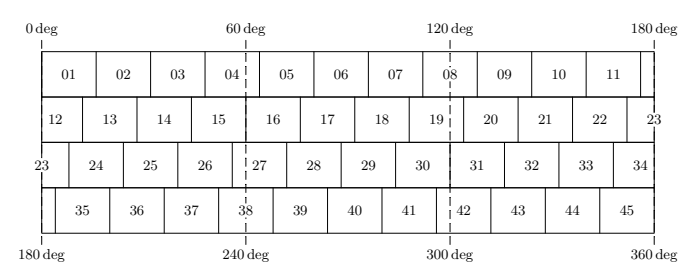


Fig. 2: Tingley plan of a fractional slot winding with phase zones,  $Q=45,\,2p=4,\,m=3,\,q=15/4,\,\alpha_Q=16\deg$ .

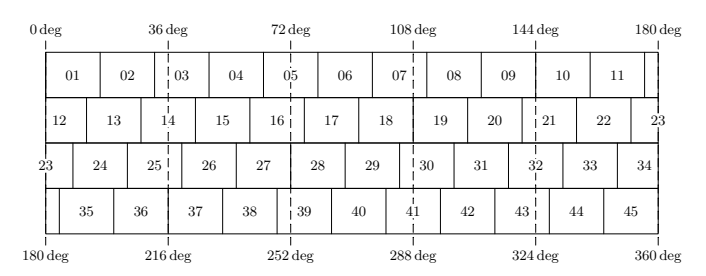


Fig. 3: Tingley plan of a fractional slot winding with phase zones,  $Q=45,\,2p=4,\,m=5,\,q=9/4,\,\alpha_Q=16\deg.$ 

equals to the number of slots per pole and phase with this composition of the various coil groups along the base winding.

For a double layer lap winding, the slots of each phase in the upper layer are given directly according to the phase zones as shown with the Tingley plan. The slots of each phase in the lower layer are given from the chosen slot step  $y_{\sigma}$ . For a single layer lap winding, sometimes a fixed slot step  $y_{\sigma}$  cannot be realized for all coils. The remaining coils with a step  $y_{\sigma}\pm 1$  must be distributed symmetrically along the base winding with regard to the number of phases. Nevertheless, the assignment of the slots to the phases can be carried out by an algorithmic procedure.

These group patterns give the best possible utilisation of the symmetrical distribution of the phase zones particularly in terms of the winding factor of the fundamental wave. However, taking into account the above composition of the various coil groups, several other group patterns are also possible, see e.g. [1], [5]. In such cases, the entire Tingley plan will be imported into the algorithmic procedure.

On the other hand, single and double layer wave windings always require interconnections within the phase rings along approximately one pole pitch. According to [1], the

total numbers of these interconnections is given by

$$n_{ic} = \frac{4 p m}{q_d} |m q_n - y_\sigma q_d| . {5}$$

Since these interconnections will often be assigned manually, the entire Tingley plan will be imported into the algorithmic procedure in such cases.

#### IV. Görges Polygon

A Görges polygon gives a two-dimensional diagram of the distribution of the MMFs of slots  $\underline{\hat{v}}_S$  and teeth  $\underline{\hat{v}}_Q$  along the circumference [1]–[4]. The normalized MMF of each slot results from the mapping of the phases onto the slots as given by the Tingley plan and symmetric time-harmonic currents within each phase. Further, the MMF of each slot defines the difference of the MMFs of two adjacent teeth. Thereby, a normalized MMF  $|\underline{\hat{v}}_{Sk}| = 1$  occurs within those slots where all layers are excited from the same phase current.

Based on the Kirchhoff law along all slots and the conservation of magnetic flux along all teeth, the MMFs of slots and teeth satisfy the equations

$$\sum_{k=1}^{Q} \hat{\underline{v}}_{Sk} = 0 , \quad \sum_{k=1}^{Q} \hat{\underline{v}}_{Qk} = 0 . \tag{6}$$

Hence, a Görges polygon along a base winding is always closed. The number of cycles of the polygon is equal to the number of pole pairs necessary for the base winding. Due to the non-uniform distribution of the winding zones along a base winding, the cycles of the polygons are different with each pole pair.

Assuming a normalized MMF of the slots of a full pitch winding with normal zone span of  $|\hat{\underline{v}}_{Sk}| = 1$ , a Görges polygon of any fractional slot winding can be described in a very general form. The geometric shape of these polygons depends only on the number of phases, the number of pole pairs of a base winding and the mapping of the phases onto the slots along a base winding. Just like pitched integer slot windings, every fractional slot windings have two types of slots, depending on the pitch those with only one phase with their normalized MMF  $|\hat{\underline{v}}_{Sk}| = 1$  and always those with two different phases with their normalized MMF  $|\hat{\underline{v}}_{Sk}| < 1$ .

Fig. 4 and Fig. 5 depict the Görges polygons of the fractional slot windings according to the already shown Tingley plans Figs. 2 & 3. Both arrangements of normal and

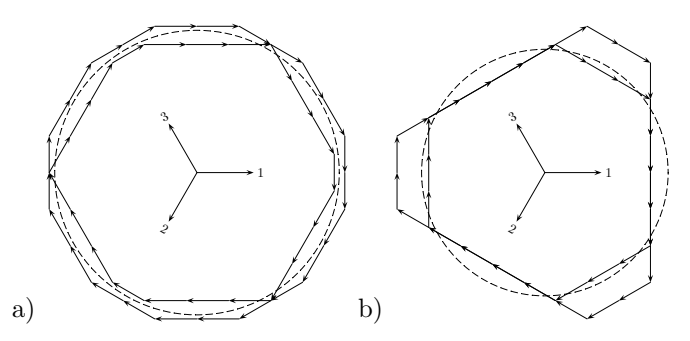


Fig. 4: Görges polygons of fractional slot lap windings,  $m=3,\ q=15/4,\ \sigma=8/9$ :

a) normal zone span, b) double zone span.

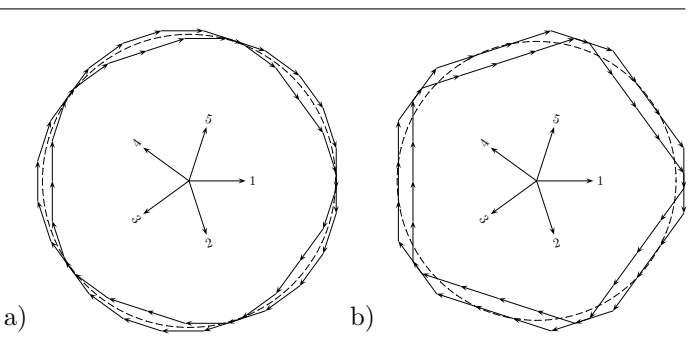


Fig. 5: Görges polygons of fractional slot lap windings,  $m=5, q=9/4, \sigma=8/9$ :
a) normal zone span, b) double zone span.

double zone spans are shown. All windings are designed as two layer lap windings with a fixed slot step  $y_{\sigma} = 10$ . The product mq = 45/4 gives the same pitch  $\sigma = 8/9$  for both number of phases. The diagrams show the time phasors of the symmetric phase currents and the circle of the fundamental wave, too.

#### V. DIFFERENTIAL LEAKAGE COEFFICIENT

Each integer and fractional slot winding enforces superharmonics along the circumference. However, a fractional slot winding with an exception of any double layer winding with  $q_d=2$  always generates additional subharmonics along the circumference.

The deviation of a Görges polygon from the circular shape corresponding to the fundamental wave provides a measure of the harmonic content of the circumferential distribution of the magnetomotive force of a polyphase armature winding. As already given in [1]–[4], [6], [7] with non-normalized values, the differential leakage coefficient  $\sigma_o$  can be obtained from the averaged square sum of the MMFs along all teeth and the winding factor  $\xi_1$  of the fundamental wave along one pole pair.

Based on the normalized MMF of the slots  $|\underline{\hat{v}}_{Sk}|$  and the normalized MMF of the teeth  $\underline{\hat{v}}_{Qk}$ , the differential leakage coefficient can be evaluated from

$$1 + \sigma_o = \left(\frac{\pi}{mq}\right)^2 \frac{1}{\xi_1^2 Q} \sum_{k=1}^Q |\hat{\underline{v}}_{Qk}|^2 . \tag{7}$$

Fractional slot windings show much more design opportunities than integer slot windings. Consequently, each Görges polygon will be treated by an algorithmic procedure. The  $t/t^*$  base windings in the majority of cases are identical in terms of their arrangement of coils and coil groups. The summation given above can be carried out adequately along slots and teeth of one base winding in such cases. Nevertheless, numerous group patterns are possible for a base winding, see e.g. [1], [5].

The winding factor of the fundamental wave can be obtained from classical formulas for lap windings with coils of a fixed slot step according to the already given natural arrangement only. A Fourier analysis of the magnetomotive forces along the slots of one base winding will be applied for other windings. In particular, this is advisable for all kinds of wave windings, for the manifold tooth-coil windings and for the winding factors of the subharmonics, too.

#### VI. APPLICATIONS

#### A. Comparison of Different Numbers of Phases

Table III lists the winding factors of the fundamental wave and the differential leakage coefficients of the fractional slot windings according to the already shown Tingley plans Figs. 2 & 3 and Görges polygons Figs. 4 & 5.

The higher number of zones with five phases enforces an increased winding factor of the fundamental wave, in particular with double zone spans. The significantly smaller content of super- and subharmonics with five phases represented by the decreased differential leakage coefficients is recognizable by the already shown Görges polygons, too.

TABLE III
COMPARISON OF THE WINDINGS WITH DIFFERENT NUMBERS OF PHASES.

Winding type	Coil pitch	Normal zone span				
Winding type	$\sigma$	$\xi_1$	$\sigma_o$			
m = 3, q = 15/4	8/9	0.940613	0.012140			
m = 5, q = 9/4	8/9	0.968885	0.007870			

Winding type	Coil pitch	Double zone span				
winding type	$\sigma$	$\xi_1$	$\sigma_o$			
m = 3, q = 15/4	8/9	0.815091	0.027047			
m = 5, q = 9/4	8/9	0.922026	0.011509			

#### B. Comparison of Lap and Wave Windings

Large hydro-generators with a high number of poles are usually equipped with a fractional slot winding with a rather small number of slots per pole and phase. According to the rated voltage of the armature winding, a phase winding typically extends along more than one base winding, too. Thus, lap windings require many interconnections of the coil groups along the poles of a base winding. For this reason, wave windings are usually the preferred winding type, in particular due to the reduced power losses because of the significantly smaller number of interconnections.

This example concerns three-phase synchronous machines of a run-of-river plant with an apparent power 50 MVA, a number of poles 2p=60, and a fractional slot winding with q=7/5. A base winding extends along 10 poles, the entire winding shows  $t=\gcd(Q,p)=6$  base windings, see Table II. The number of slots Q/t=42 along one base winding yields a total number of slots Q=252. Considering the winding factor of the fundamental wave and the product mq=21/5, a slot step as of  $y_{\sigma}=4$  is advisable.

Fig. 6 depicts the voltage phasor diagram and the Tingley plans of both lap and wave windings. Fig. 7 shows the respective Görges polygons. Both diagrams show the time phasors of the symmetric phase currents and the circle of the fundamental wave, too.

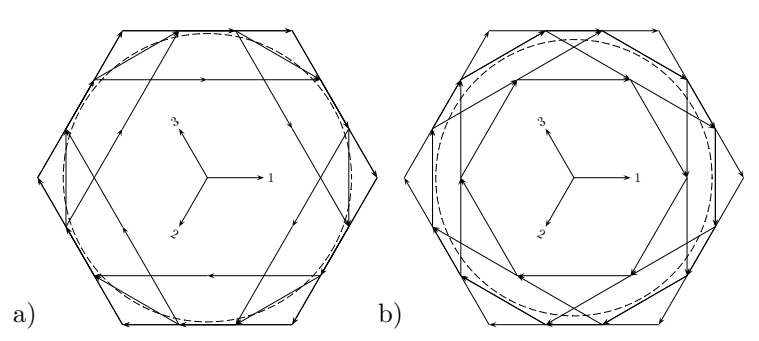


Fig. 7: Görges polygons of fractional slot windings,  $Q=42, \, 2p=10, \, m=3, \, q=7/5;$  a) lap winding  $y_{\sigma}=4, \, \sigma=20/21,$  b) wave winding  $y_{\sigma}=4, \, \sigma=17/21.$ 

The lap base winding has two parts with a phase difference as of  $\pi$ . Each part consists of three groups with one coil and two groups with two coils, in summary seven coils within five groups. The wave base winding has two branches with a phase difference as of  $\pi$ . The four interconnections within upper and lower layers necessary for closed branches of e.g. phase 3 are inserted between the coil sides UL02-UL07, UL41-UL04 and LL23-LL28, LL20-LL25. In comparison of both winding types, the lap winding with a fixed slot step shows a fixed pitch  $\sigma = 20/21$ . However, the wave winding shows a wider extend along the pole pitches resulting in an effective pitch  $\sigma = 17/21$ .

Table IV lists the winding factors of the fundamental wave and the differential leakage coefficients of the described lap and wave windings. The different winding factors di-

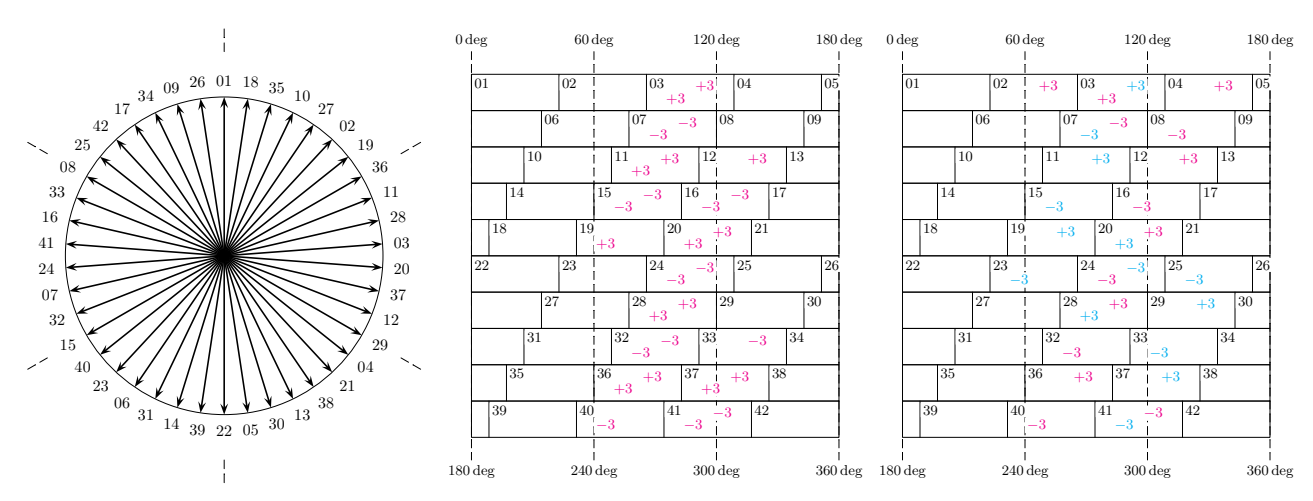


Fig. 6: Voltage phasor diagram and Tingley plans of fractional slot windings, Q=42, 2p=10, m=3, q=7/5; lap winding  $y_{\sigma}=4, \sigma=20/21$  and wave winding  $y_{\sigma}=4, \sigma=17/21.$ 

rectly result from the different pitch values. However, the harmonic content from both super- and subharmonics is quite the same. The Fourier analysis along a base winding yields the winding factors of the subharmonic wave of order  $\nu=-1/5$  of the lap and wave windings as of  $\xi_{-1/5}=0.022033$  and  $\xi_{-1/5}=0.027309$ , respectively.

In spite of the winding factors, the machines are equipped with the shown wave windings. One of the main reasons lies from the reduced power losses due to the significantly a) smaller number of interconnections.

TABLE IV Synchronous machine, 50 MVA,  $2p=60,\ m=3,\ q=7/5,$  comparison between Lap and wave windings.

Windington	Coil mitals	Normal zone span					
Winding type	Coil pitch	$\xi_1$	$\sigma_o$				
$Lap y_{\sigma} = 4$	$\sigma = 20/21$	0.953148	0.077751				
Wave $y_{\sigma} = 4$	$\sigma = 17/21$	0.913356	0.077892				

#### C. Comparsion of Various Slot Steps

This example concerns three-phase synchronous machines of a quick start pumped storage power plant with an apparent power 500 MVA, a number of poles 2p=14, a fractional slot winding with q=23/7 and a total number of slots Q=138. Fig. 8 depicts the Tingley plan of this entire winding along all 14 poles.

0 d	eg							60	d	eg							1	20	deg	g						180	deg
	01			02			03	-		04	05				06		07	7	. 0			(	9		10		
		11		1	2		13		Ī	14		1	5		1	16			17		18			19		20	
		21	l		22		2	3	I	24	Į		25	,		26			27		1	28		2	9	30	
		;	31		32			33	į	;	34		3	35		3	6		3	37		38			39		
4	10		41		4	2		43	į		44			45			46			47		48			49		
	50		5	1		52		5	į		5	64		5	55 56			57			8		59				
	60			61		62	2	6		63 64				65		6	6		67		68		(	9			
	70	)		71			72		i	73	74			75		76		}	77			7	78		79		
	8	80		8	1		82		1	83	84			85			86 8		87	87 8		88		89			
		90	)		91		9	2		93	3		94	Į		95			96	;	Ç,	97		9	8	99	
		1	00		101		1	102	i	1	03		1	04		10	)5		1	06		107		1	108		
10	09		110		11	11		112	į		113	3		114	Į.		115			116		11	7		118		
	119		12	0		121		12	22	:	1:	23		12	24		125	5	iL	12	6	1	27		128	3	
	129		1	30		13	1		132			133			134 135		35		136			13	7	1	38		
180	deg							240	) (	leg							3	00	deg	Š						360	deg

Fig. 8: Tingley plan of fractional slot windings, Q = 138, 2p = 14, m = 3, q = 23/7.

The lap winding has two parts with a phase difference as of  $\pi$ . Each part consists of five groups with three coils and two groups with four coils, in summary 23 coils within seven groups. Regarding the product mq=69/7, two different slot steps as of  $y_{\sigma}=8$  and  $y_{\sigma}=9$  are discussed hereinafter. Fig. 9 shows the respective Görges polygons. The diagrams show the time phasors of the symmetric phase currents and the circle of the fundamental wave, too.

Table V lists the winding factors of the fundamental wave and the differential leakage coefficients of the two lap windings. Again, the different winding factors directly result from the different pitch values. The harmonic content from both super- and subharmonics will be 10% smaller with the shorter slot step. The Fourier analysis along the

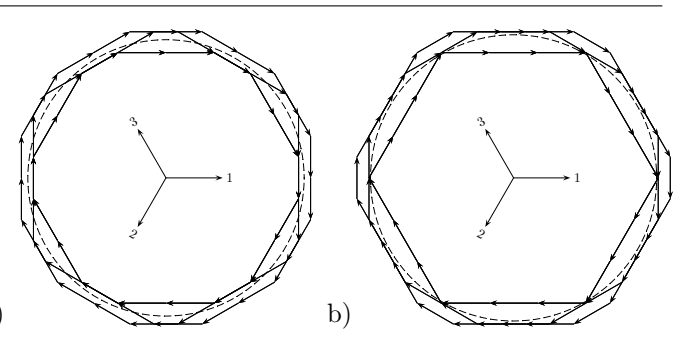


Fig. 9: Görges polygons of fractional slot lap windings,  $Q=138,\ 2p=14,\ m=3,\ q=23/7;$ 

- a) slot step  $y_{\sigma} = 8$ ,  $\sigma = 56/69$ ,
- b) slot step  $y_{\sigma} = 9, \, \sigma = 63/69.$

winding yields the winding factors of the subharmonic wave of order  $\nu = +1/7$  of the lap windings with slot steps as of  $y_{\sigma} = 8$  and  $y_{\sigma} = 9$  as of  $\xi_{+1/7} = 0.004042$  and  $\xi_{+1/7} = 0.004540$ , respectively.

In spite of the decreased fundamental winding factor, the machines are equipped with lap windings with a slot step  $y_{\sigma} = 8$  in view of the reduced differential leakage coefficient and particularly the winding factor of the subharmonic wave.

TABLE V Synchronous machine, 500 MVA,  $2p=14,\ m=3,\ q=23/7,$  comparison of different shortenings.

Winding tune	Coil mitch	Normal zone span					
Winding type	Coil pitch	$\xi_1$	$\sigma_o$				
$Lap y_{\sigma} = 8$	$\sigma = 56/69$	0.913494	0.014831				
$Lap y_{\sigma} = 9$	$\sigma = 63/69$	0.946117	0.016359				

#### D. Tooth-Coil Windings

All kinds of tooth-coil windings show a definite slot step  $y_{\sigma} = 1$ . With the intent of a reasonable pitch factor of the fundamental wave, the number of slots per pole and phase of such windings will be chosen from the range

$$\frac{2}{3} \le \frac{1}{m \, q} \le \frac{4}{3} \tag{8}$$

Hence, the number of slots per pole and phase follows from the symmetry conditions as listed in Table I and

$$\frac{3}{4m} \le \frac{q_n}{q_d} \le \frac{3}{2m}$$
,  $\gcd(q_d, m) = 1$ . (9)

As an example, Fig. 10 shows voltage phasor diagram, Tingley plan and Görges polygon of the tooth-coil winding with the number of slots per pole and phase q=2/5. Table VI lists the fundamental winding factor and the differential leakage coefficient for selected two layer tooth-coil windings.

Obviously, there are main drawbacks of tooth-coil windings in terms of the harmonic content. On the one hand, the winding factor of the fundamental wave will be less than with other fractional slot windings especially with a low number of phases. On the other hand, the differential leakage coefficient is always significantly higher than with other fractional slot windings.

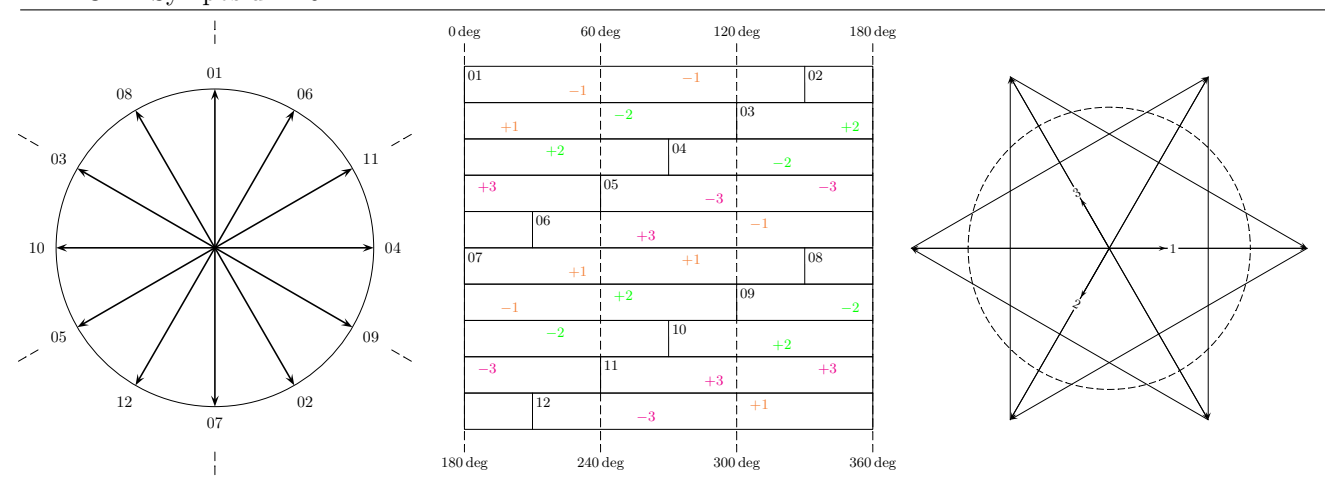


Fig. 10: Voltage phasor diagram, Tingley plan and Görges polygon of tooth-coil windings; Q = 12, 2p = 10, m = 3, q = 2/5,  $\sigma = 5/6$ .

TABLE VI Fundamental winding factor and differential leakage coefficient of selected two layer tooth-coil windings.

Number of phases $m$	Range	Winding parameter			Windin	ng data		
		$q = q_n/q_d$	2/3	2/5	3/5	3/7	4/7	5/7
2	$\frac{3}{8} < \frac{q_n}{q_d} < \frac{3}{4}$	$\xi_1$	0.853553	0.853553	0.879653	0.879653	0.888716	0.805496
	- 4u -	$\sigma_o$	0.905026	4.291739	1.214393	3.340210	1.391825	0.863412
	$\frac{1}{4} \le \frac{q_n}{q_d} \le \frac{2}{4}$	$q = q_n/q_d$	1/2	1/4	2/5	2/7	3/7	3/8
3		$\frac{1}{4} \le \frac{q_n}{q_d} \le \frac{2}{4}$	$\xi_1$	0.866025	0.866025	0.933013	0.933013	0.901912
	- 44 -	$\sigma_o$	0.462164	4.848654	0.968349	2.857964	0.834941	1.182101
	$\frac{3}{20} < \frac{q_n}{q_d} < \frac{3}{10}$	$q = q_n/q_d$	1/4	1/6	2/7	2/9	2/11	3/11
5		$\xi_1$	0.951057	0.951057	0.880037	0.975528	0.975528	0.900237
		$\sigma_o$	0.745851	2.928164	0.561113	1.100125	2.137223	0.637304

These properties are caused by two facts. The fixed slot step  $y_{\sigma}=1$  yields a rather constant winding factor of the superharmonics. The number of slots per pole and phase q<1 enforces a considerable portion of subharmonics, too. Apparently, the substantially increased harmonic content also exists with a higher number of phases.

However, tooth-coil windings present various well-known advantages. E.g. the reduced amount of conducting material and the reduced power losses in the end winding region as well as an easier manufacturing should be mentioned.

#### VII. CONCLUSION

The paper presents an algorithmic evaluation of the differential leakage coefficient of symmetric fractional slot windings with an arbitrary number of phases based on the Görges polygon of such windings. The mapping of the phases onto the slots of a single or double layer base winding with normal as well as double zone spans follows from the respective Tingley plans. The plans of lap windings follow directly from the distribution of the phase zones along the base winding. However, in case of wave windings, the entire plans will be imported into the algorithmic process.

The application of the algorithmic evaluation is shown in detail using examples with fractional slot windings of practically existing machines. The presented approach allows for an easy to use and fast implementation into the design process and an optimization of polyphase windings with an arbitrary number of phases. In particular, all kinds of tooth-coil windings can be analyzed very efficiently by the proposed method.

#### References

- Sequenz H.: Die Wicklungen elektrischer Maschinen, Band I, Springer Verlag, Wien, 1950.
- [2] Richter R.: Elektrische Maschinen, Band IV, Birkhäuser Verlag, Basel/Stuttgart, 1954.
- [3] Müller G., Vogt K., Ponick B.: Berechnung elektrischer Maschinen, Wiley-VCH Verlag, Weinheim, 2008.
- [4] Pyrhönen J., Jokinen T., Hrabovcová V.: Design of Rotating Electrical Machines, John Wiley & Sons Ltd, 2008.
- [5] Liwschitz M.M.: "Differential Leakage of the Different Patterns of a Fractional Slot Winding." Transactions of the American Institute of Electrical Engineers, Vol. 68, No. 2, Jul 1949.
- [6] Caruso M., Di Tommaso A.O., Marignetti F., Miceli R., Ricco Galluzzo G.: "A General Procedure for the Construction of Görges Polygons for Multiphase Windings of Electrical Machines." Proceedings of the IEEE International Conference on Ecological Vehicles and Renewable Energies (EVER 2018), Monte Carlo (Monaco), Apr 2018.
- [7] Caruso M., Di Tommaso A.O., Genduso F., Miceli R., Ricco Galluzzo G.: "A General Mathematical Formulation for the Determination of Differential Leakage Factors in Electrical Machines With Symmetrical and Asymmetrical Full or Dead-Coil Multiphase Windings." *IEEE Transactions on Industry Appli*cations, Vol. 54, No. 6, Nov/Dec 2018.

# Data driven parameter identification of nonlinear magnetic properties in steel sheets

E. Mušeljić, A. Reinbacher-Köstinger, A. Gschwentner and M. Kaltenbacher

Institute of Fundamentals and Theory in Electrical Engineering, TU Graz, Inffeldgasse 18/1, 8010 Graz, Austria E-mail: emuseljic@tugraz.at

Abstract—To perform high fidelity simulations of electrical machines, it is crucial to have appropriate material models. Determining the parameters of such material models usually requires a lot of computational power and the performed simulations in such cases are usually not reused. Meaning that data obtained this way, is vastly underutilized in practice. In this work, we investigate the application of machine learning methods for the identification of the magnetic permeability in cut electrical steel sheets for the nonlinear material case. The proposed method uses the idea of mapping the magnetic field measurements, above the steel sheets, to field values in the steel sheets. In doing so, it is possible to reuse the simulation information for the particular measurement setup. The approach is validated on simulated measurement data.

Index Terms—Parameter identification, Machine learning, Materials, Magnetics

#### I. Introduction

Accurate material models [1] are necessary nowadays to facilitate the ever growing demand for highly optimized devices. Specifically, when building electrical machines, the degradation due to the cutting process [2], [3] has a great influence on the magnetic properties of the material. These degradation profiles of the materials introduce new unknowns which raise the complexity of the problem. This paper is about the process of obtaining the parameters, which describe the material model with the degradation profile. An adjoint based method applied to the same problem can be found in [4]. Here we apply a data driven approach, for which we precompute a dataset containing different material parameter sets. This data is then used to fit models, which are subsequently used in the identification process. In the following sections we first introduce the experimental setup, the computational model based on it and explain the material model used within. Next we explain the approach used to identify the parameters, after this the approach is evaluated and the results are shown. We do this on simulated measurement values as real measurement values are not yet available. Finally we give a summary of the main points and conclusion.

#### II. COMPUTATIONAL MODEL

The sensor-actuator system, depicted in Figure 1, consists of stacked iron sheets and two excitation coils. With this system it is possible to locally magnetize electrical steel sheets while, at the same time, measuring the local magnetic flux density. An array of  $N_{\rm S}$  Hall sensors is used to precisely measure the x-,y- and z-components of the magnetic flux above the steel sheets. The arrangement used consists of two steel sheets (Sample 1 and 2) placed so that the cutting edges of these face each other. Such a setup is needed to make sure that the cutting edges get magnetized correctly and also to ensure a satisfying sensitivity for the inverse scheme [7]. In such a setup, where Sample 1 and 2 are from

the same batch with the same cutting parameters, it is valid to assume a symmetrical and identical material behavior in these. The measurement data is obtained by

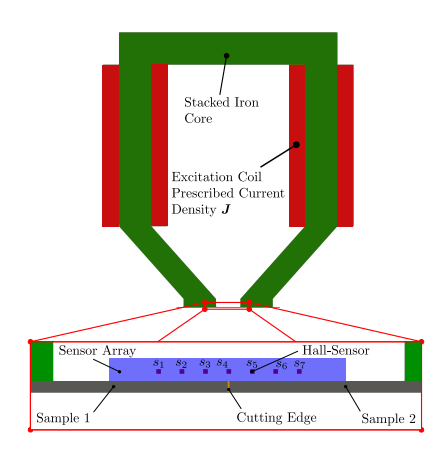


Fig. 1. The sensor-actuator model with two electrical steel sheets, denoted as Sample 1 and Sample 2. All simulations of the system are performed with *openCFS* [6].

moving the sensor-actuator system along the x-direction and recording the measurements at  $N_{\rm P}$  positions. As the material variation is greater in the vicinity of the cutting edge, more measurement points are placed here as opposed to the bulk part of the material. Also, the steel sheets are demagnetized between each measurement position. The resulting data set contains measurements for the three magnetic field components at each sensor and measurement position, denoted as  $B_{x,i,j}^{\rm meas}$ ,  $B_{y,i,j}^{\rm meas}$  and  $B_{z,i,j}^{\rm meas}$  with  $i=1,2,...,N_{\rm S}$  the sensor positions and  $j=1,2,...,N_{\rm P}$  the measurement positions. Subsequently, based on this information, the measurement data can be summarized in

$$\mathbf{B}^{\text{meas}} = \begin{bmatrix} B_{x,1,1}^{\text{meas}} & B_{y,1,1}^{\text{meas}} & B_{z,1,1}^{\text{meas}} \\ & \vdots & \\ B_{x,N_{\text{S}},N_{\text{P}}}^{\text{meas}} & B_{y,N_{\text{S}},N_{\text{P}}}^{\text{meas}} & B_{z,N_{\text{S}},N_{\text{P}}}^{\text{meas}} \end{bmatrix}. \quad (1)$$

The magnetic field density amplitude is computed using the Euclidean norm, represented as

$$B_{i,j}^{\rm meas} = \sqrt{(B_{x,i,j}^{\rm meas})^2 + (B_{y,i,j}^{\rm meas})^2 + (B_{z,i,j}^{\rm meas})^2}, \quad (2)$$

leading to the amplitude of the measurement data

$$||\mathbf{B}^{\text{meas}}||_2 = \begin{bmatrix} B_{1,1}^{\text{meas}} & B_{2,1}^{\text{meas}} & \dots & B_{N_S,N_P}^{\text{meas}} \end{bmatrix}^{\text{T}}.$$
 (3)

#### A. Material model

The degradation zone of the material extends a few millimeters away from the cutting edge. The size of this zone depends on the cutting technique and parameters. To model this behavior of the material, the electrical steel sheets are divided into M subdomains  $\Omega_m$ . A zoomed in view of the subdivided electrical steel sheets is shown in Figure 2. As can be seen, the sizes of these subdomains are smaller near the cutting edge, again to better resolve the material degradation near the cutting edge. For each

Fig. 2. Electrical steel sheet discretization into M subdomains  $\Omega_m$  with m=1,2,...,M (color coded), each subdomain assigned with a magnetic reluctivity  $\nu_m$  in the linear case and a BH-curve for the nonlinear case.

subdomain  $\Omega_m$ , a BH-curve is defined and given by the magnetic reluctivity

$$\nu(B; \mathbf{c}_m) = c_{0,m} + c_{1,m} B^{c_{2,m}}, \ \forall B = ||\mathbf{B}||_2.$$
 (4)

The material behavior, in each subdomain  $\Omega_m$ , is therefore defined by the three parameters  $c_{0,m},c_{1,m},c_{2,m}$ . In general, for the given setup of M subdomains, we can write the parameter vector as

$$\mathbf{p} = \begin{bmatrix} c_{0,0} & c_{1,1} & c_{2,1} & \dots & c_{0,M} & c_{1,M} & c_{2,M} \end{bmatrix}^{\mathrm{T}}.$$
(5)

The total number of material parameters is therefore 3M.

#### III. PARAMETER IDENTIFICATION

The parameter identification approach consists of multiple steps. A flowchart of the steps performed in the pipeline is depicted in Figure 3. The measured magnetic flux values  $\mathbf{B}^{\mathrm{meas}}$  are denoted as  $\mathbf{B}_{\mathrm{o}}$ , standing for the magnetic flux values outside the steel sheets. With  $\mathbf{B}_{\mathrm{i}}$  and  $\mathbf{H}_{\mathrm{i}}$  we denote, respectively, the magnetic flux and the magnetic field inside the steel sheets. The values of  $\mathbf{B}_{\mathrm{i}}$  and  $\mathbf{H}_{\mathrm{i}}$  are in all cases evaluated at the center points of the subdomains  $\Omega_m$ , as can be seen in Figure 2. Two mapping functions,

$$\hat{\mathbf{B}}_{i} = \hat{f}_{B-\text{map}}(\mathbf{B}_{o}), \tag{6}$$

$$\hat{\mathbf{H}}_{i} = \hat{f}_{H-\text{map}}(\hat{\mathbf{B}}_{i}), \tag{7}$$

are used to obtain the values of  $\mathbf{B}_i$  and  $\mathbf{H}_i$ , which cannot be directly measured. We make a distinction here using the *hat* symbol, over the variables, for approximated values. Therefore,  $\mathbf{B}_i$  represents values obtained by measurement or simulation and  $\hat{\mathbf{B}}_i$  the approximated values obtained from the mapping functions. The same

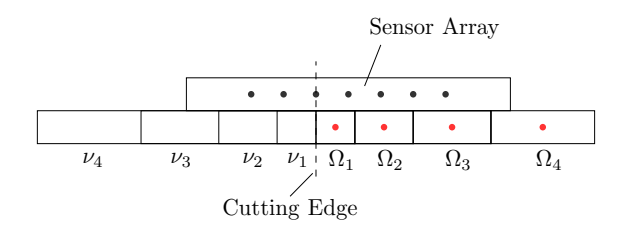


Fig. 3. The magnetic flux values outside the steel sheets,  $\hat{\mathbf{B}}_{\text{o}}$ , are mapped onto the magnetic flux values inside the steel sheets,  $\hat{\mathbf{B}}_{\text{i}}$ . Variables with subscript "i" are defined where the red dots are located. With the second mapping function  $\hat{f}_{\mathrm{H-map}}$ , we then map  $\hat{\mathbf{B}}_{\text{i}}$  to the magnetic field  $\hat{\mathbf{H}}_{\text{i}}$  inside the steel sheet. Finally  $(\hat{\mathbf{B}}_{\text{i}},\hat{\mathbf{H}}_{\text{i}})$  are used within a classic parameter identification approach to obtain  $\hat{\mathbf{p}}$ .

is true for all other variables. In the final step we use the obtained value pairs  $(\hat{\mathbf{B}}_i,\,\hat{\mathbf{H}}_i)$  as inputs for a least squares parameter identification. From the relation

$$\hat{\mathbf{H}}_{i} = \nu(\hat{B}_{i}; \mathbf{p})\hat{\mathbf{B}}_{i}, \tag{8}$$

where  $\hat{B}_i$  is the magnitude of the magnetic flux density  $\hat{\mathbf{B}}_i$ , we define the residual as

$$e(\hat{\mathbf{B}}_{i}, \hat{\mathbf{H}}_{i}; \mathbf{p}) = (\hat{\mathbf{H}}_{i} - \nu(\hat{B}_{i}; \mathbf{p})\hat{\mathbf{B}}_{i})^{2}.$$
 (9)

Finally, the optimization problem can be defined as

$$\mathbf{p}^* = \arg\min_{\mathbf{p}} e(\hat{\mathbf{B}}_{i}, \hat{\mathbf{H}}_{i}; \mathbf{p}), \tag{10}$$

and by solving it we obtain the optimized parameter vector  $\mathbf{p}^*$ . For this approach to work we need to complete several steps. These are listed below and explained in more detail in the following subsections.

- A. Sampling the high fidelity FE simulation for different **p** vectors
- B. Construct the mapping functions  $\hat{f}_{\mathrm{B-map}}$  and  $\hat{f}_{\mathrm{H-map}}$
- C. Perform nonlinear least squares [8] to identify the unknown parameters

#### A. Model sampling

To be able to construct the mapping functions,  $\hat{f}_{B-map}$ and  $f_{\rm H-map}$ , we first need to obtain the data. This step is crucial in the sense that it determines the range in which the method will be applicable. Meaning that, we first need to select an appropriate range for the parameters in p, and secondly, the right system excitation levels. In this paper we take the largest possible range for the parameters in p. It is important to note here, that we don't put any additional constraints on the parameters between the individual subdomains  $\Omega_m$ . This means that, the resulting parameter combinations can produce samples which are physically not feasible but for the sake of exploring the parameter space and giving the surrogate model additional information, they are useful. Surely, one could define an additional constraint on the parameter values to reflect a known behavior of the material parameters.

For the excitation levels we define 10 points on a curve given by

$$J_{\text{exc}}(x) = J_{\text{init}} \cdot 10^x, \tag{11}$$

where  $J_{\rm init}=10^4\frac{A}{m^2}.$  The resulting excitation curve is given in Figure 4. Finding the best excitation curve

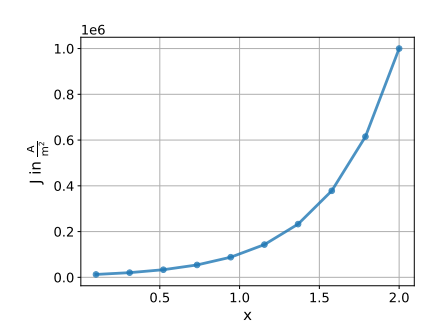


Fig. 4. The excitation curve used for all performed simulations.

for the simulation was not part of this work but it has a significant influence when applying the method. As using a smaller number of excitation points, means doing less simulations, therefore saving computational time. Additionally, also, the optimal excitation curve maximizes the information content at each excitation level, making the whole identification task simpler for the optimizer.

Given the ranges for the parameters in  $\mathbf{p}$  we construct a sampling plan with the shape  $(N \times 3M)$ . N is the number of samples and 3M gives us the total number of parameters in  $\mathbf{p}$ . For the sampling plan generation we use a Latin Hypercube Sampling (LHS) plan [9]. Using such sampling approaches is crucial in cases when dealing with a high dimensional input space. It maximizes the information content by optimizing the placement of samples in the input space. For the problem at hand the data generated is described in Table I. The main information in the generated datasets

$\mathbf{M}$	N	Train split $\mathbf{B}^{\mathrm{Train}}$	Test split $\mathbf{B}^{\mathrm{Test}}$	$N_{ m exc}$
5	2000	1500	500	10

TABLE I

An LHS sampling plan with 2000 samples for 15 total parameters is generated and simulated for each of the 10 excitation levels. This data is split into a train and test set of 1500 and 500 samples respectively.

are for each excitation level the magnetic flux values outside the steel sheets,  $\mathbf{B}_{\rm o}$ , as well as the magnetic flux and the magnetic field inside the steel sheets,  $\mathbf{B}_{\rm i}$  and  $\mathbf{H}_{\rm i}$ . Furthermore, we assume that the measurements  $\mathbf{B}^{\rm meas} = \mathbf{B}_{\rm o}$  are noisy due to the measurement process and this noisy data we denote as  $\tilde{\mathbf{B}}_{\rm o}$ .

#### B. Mapping functions

After having generated the datasets, the mapping functions can be constructed by fitting an interpolation

model onto the data. For this purpose we have used Gaussian Process Regression (GPR) [10]. GPRs perform very well in high dimensional spaces due to their high flexibility and the ability to control the smoothness and continuity of the resulting function by choice of the kernel function and it's parameters. Another point which makes them useful is that they are very data efficient, which means that it is possible to produce accurate interpolations with smaller datasets. There

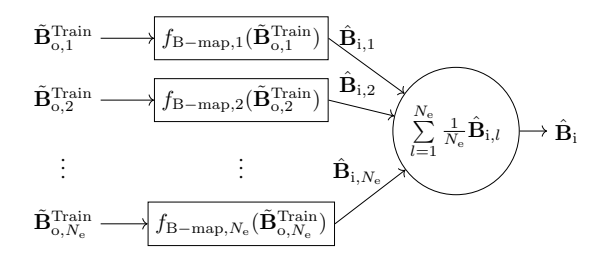


Fig. 5. Training process for the  $N_{\rm e}$  models in the  $f_{\rm B-map}$  ensemble. This is used to illustrate the point that each individual mapping function inside the ensemble has it's own instance of the noisy training data.

are also approaches where the relationship between the parameters  $\mathbf{p}$  and the measurements  $\mathbf{B}_{o}$  is directly modeled by a surrogate model like GPR. By doing so the model gets the measurements  $\mathbf{B}_{\mathrm{o}}$  as inputs and the parameters p are the outputs. Applying such an approach to this problem did not work well. The main cause for this is the complex relationship between the parameters and the measurements which leads to non unique solutions. Also, using the GPRs directly on the noisy measurements  $\mathbf{B}_{0}$  does not produce satisfying results, because the variance in the field values due to the noise levels distorts the mapping information in the data. Thus, leading to the GPRs not being able to interpolate correctly. To counteract this, we employ so called ensembles of GPRs [11]. The main idea behind this is that, many models together create a better prediction than one single model. Especially in the case of uncertainty in the input variables, where GPRs do not offer many methods on counteracting it, compared to the uncertainty in the outputs. By applying this method we can incorporate knowledge about the noise in the measurements. This is achieved by using the training set  $\mathbf{B}_{\mathrm{i}}^{\mathrm{Train}}$ , from Table I, and for  $N_{\mathrm{e}}$  ensemble models and a noise level  $\eta$ , we generate  $N_{\rm e}$  noisy datasets  $\tilde{\bf B}_{\rm i,l}^{\rm Train}$  $(l=1,\ldots,N_{\rm e})$ . Each of these  $N_{\rm e}$  noisy datasets share the same noise level  $\eta$  but are just different draws from the same random distribution. Then for each dataset  $ilde{\mathbf{B}}_{\mathrm{i}\;l}^{\mathrm{Train}}$  one  $f_{\mathrm{B-map},l}$  is fitted. Finally the main prediction output  $\hat{\mathbf{B}}_{i}$  is constructed as the average over the  $N_{e}$ outputs  $\hat{\mathbf{B}}_{i,l}$ , as can be seen in Figure 5. To evaluate the ensemble on some input  $B_0$  we just feed the same input to all of the submodels in the ensemble, as in Figure 6. The rest is the same as in the case of the training process.

For the  $f_{\rm H-map}$  function we don't need to use the ensemble as we have only the uncertainty in the  ${\bf B}_{\rm o}$ 

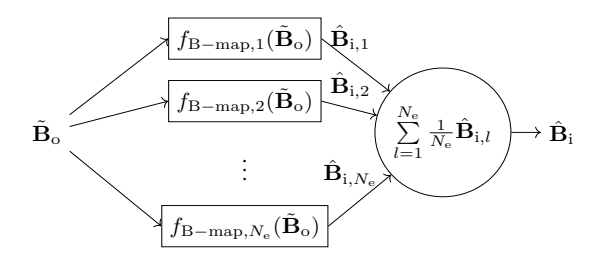


Fig. 6. Evaluation process for the  $N_{\rm e}$  models in the  $f_{\rm B-map}$  ensemble.

values, outside the steel sheet, where the measurement is taken. Therefore, for the  $f_{\rm H-map}$  function we just use a standard GPR to perform the mapping to the  $\hat{\mathbf{H}}_{\rm i}$  values. All of the used GPRs are constructed as a combination of the *RBF* (Radial Basis Function) and *WhiteKernel* kernels, available in the *GaussianProcessRegressor* class in the Scikit-learn [12] package for python.

#### C. Nonlinear least squares

Now that the mapping functions are constructed, we can use these to obtain the value pairs  $(\hat{\mathbf{B}}_i, \hat{\mathbf{H}}_i)$  for each excitation level. By doing so, we essentially get the information we need to reconstruct the BH-curve, Figure 7, of the underlying material. We employ the nonlinear least squares approach to solve the problem defined in (10). As a results, we obtain the optimal parameters  $\mathbf{p}^*$  for the material curve function (4). This step is also beneficial in the sense that smaller deviations, in the predicted value pairs  $(\hat{\mathbf{B}}_i, \hat{\mathbf{H}}_i)$ , have no significant influence on the final result as these get filtered out by the identified curve which best fits the data.

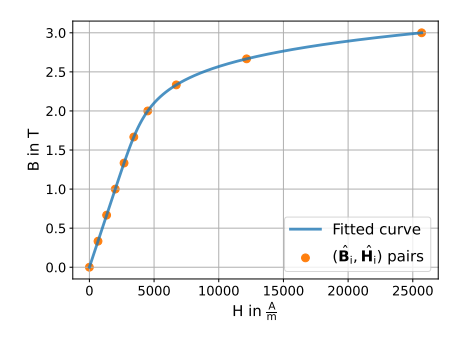


Fig. 7. Example BH-curve obtained by sampling the mapping functions at different excitation levels and then performing the identification to obtain the parameters for the material curve function.

#### IV. RESULTS

The models constructed in the approach, described in the previous sections, are saved and do not change in the following investigation. We evaluate the approach for three cases of the noise level  $\eta = [0.05, 0.1, 0.15]$  which corresponds to 5%, 10% and 15% noise, respectively. The results are evaluated by using the test data as seen in Table I. For each noise level, we perform a statistical error evaluation to get a better estimate on the actual

performance of the approach. The reason behind this is that for example, a noise instance could be generated which gives very good or, on the contrary, very poor results. This would lead to false estimates of the error values. To get a better estimate for the errors, we run each experiment, for the different noise levels, for 100 different random seeds. Each time, generating the noise to overlay over the test data  $\mathbf{B}_{0}^{\mathrm{Test}}$  and obtain the noisy test data  $\tilde{\mathbf{B}}_{0}^{\mathrm{Test}}$ . On Figures 8, 9, 10, 11, we have shown the relative error of the identified  $\nu(\hat{B}_i; \mathbf{p})$  curve values compared to the correct ones in each of the 5 subdomains. We can see that, on average, only single digit relative errors are present, even in the case of the large noise level of 15%. Additionally, we can see that the errors are the largest in the vicinity of the cutting edge. This is expected, as also the uncertainty in the field values near the cutting edge is the largest. The cause for this, can be explained by the smaller subdomains in the region near the cutting edge and therefore smaller sample of this discrete material portion. As explained in subsection III-A, we don't add any additional constraints over the parameters in the generated dataset. Therefore the shown errors can further be reduced by introducing an additional constraint over the parameter behavior making the identification problem somewhat simpler. In Figure 12, we can see an example identification of a representative material case where the material properties get better when moving away from the cutting edge. The figure shows an identification carried out at 5% noise level. Another important aspect of the sampling process is that the choice of the excitation levels influences the range in which the identified BH-curve is identified. So adapting the excitation level to the usage levels is necessary to guarantee identifications over the whole range. Also, the error calculations are based on these ranges so anything outside the range is not considered.

#### V. CONCLUSION

We have presented an approach which uses Gaussian Process Regression (GPR) to estimate not measurable field values, inside the cut steel sheets, from measured field values outside. Then, we use these estimated values, at different excitation levels of the system, to identify the underlying material parameters of the different subdomains. The proposed method incorporates ensembles of GPRs to counteract the variance in the inputs by introducing knowledge about the measurement noise through the augmented training data. Finally, the non linear least squares method is applied to identify the parameters of the material BH-curve function in each subdomain of the steel sheets. Looking at the statistical evaluation of the results for three nonzero noise levels, we see that the proposed approach performs well even for strong noise influence. An important benefit of such an approach is that, the constructed maps and the whole pipeline with these can be reused for the same material type if the selected parameter ranges and system excitation levels

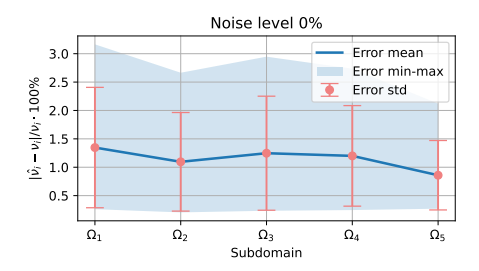


Fig. 8. Error over  $\tilde{\mathbf{B}}_{\mathrm{o}}^{\mathrm{Test}}$  evaluated for 100 random noise instances (with  $\eta=0.0$ ).

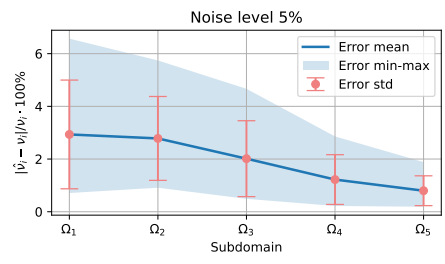


Fig. 9. Error over  $\tilde{\mathbf{B}}_{o}^{Test}$  evaluated for 100 random noise instances (with  $\eta=0.05$ ).

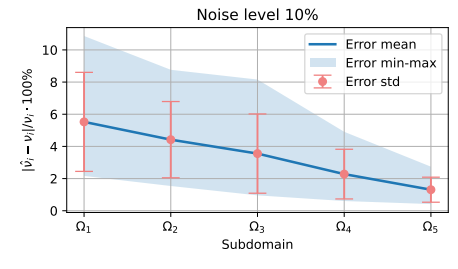


Fig. 10. Error over  $\tilde{\mathbf{B}}_{\rm o}^{\rm Test}$  evaluated for 100 random noise instances (with  $\eta=0.10$ ).

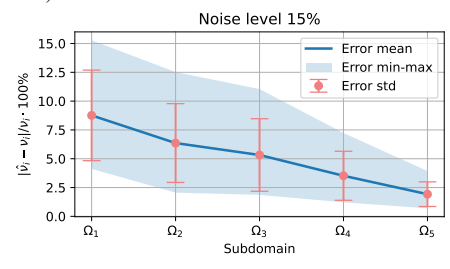


Fig. 11. Error over  $\tilde{\mathbf{B}}_{o}^{Test}$  evaluated for 100 random noise instances (with  $\eta=0.15$ ).

do not change. This makes it possible to just run the identification process without the need for generating new samples with the high fidelity FE simulation. In the end, making it even possible to do fast online identification. As an outlook, we still have to test the method on real world measurement data. There are also some other points to consider to even further increase the performance of the method, like, optimizing the selection of the system excitation levels, selecting appropriate parameter ranges and dealing with discrepancies between the simulation and the real world measurements.

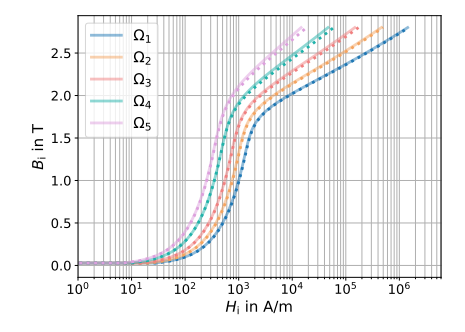


Fig. 12. Example of identified BH-curves for the case of  $\eta=0.05$  (5%) noise, for a representative material case. The figure shows 5 different colors for the different subdomains. The full lines are the exact curves while the dots correspond to the identified curves.

#### VI. ACKNOWLEDGEMENT

This work is partially supported by the joint Collaborative Research Centre CREATOR (DFG: ProjectID 492661287/TRR 361; FWF: 10.55776/F90) at TU Darmstadt, TU Graz and JKU Linz.

#### REFERENCES

- [1] Li, M. and Mohammadi, M.H. and Rahman, T. and Lowther, D., "Analysis and design of electrical machines with material uncertainties in iron and permanent magnet", COMPEL the International Journal for Computation and Mathematics in Electrical and Electronic Engineering Vol. 36 5, (2017)
- [2] Schoppa, A. and Schneider, J. and Wuppermann, C.-D., "Influence of the manufacturing process on the magnetic properties of nonoriented electrical steels", Journal of Magnetism and Magnetic Materials 215/216, (2000)
- [3] Sundaria, R. and Hemeida, A. and Arkkio, A. and Daem, A. and Sergeant, P. and Belahcen, A., "Effect of different cutting techniques on magnetic properties of grain oriented steel sheets and axial flux machines", IECON 2019-45th Annual Conference of the IEEE Industrial Electronics Society Vol. 1, (2019)
- [4] M. Kaltenbacher and A. Gschwentner and B. Kaltenbacher and S. Ulbrich and A. Reinbacher-Köstinger, "Inverse Scheme to Locally Determine Nonlinear Magnetic Material Properties: Numerical Case Study", Mathematics Vol 12. 10, (2024)
- [5] Gschwentner, A. and Roppert, K. and Kaltenbacher, M., "Determination of Local Magnetic Material Properties Using an Inverse Scheme", IEEE Transactions on Magnetics Volume 60, 2024, 3, pages 1-4, https://doi.org/10.1109/TMAG.2023.3299620
- [6] Kaltenbacher M, et al, "openCFS (Coupled Field Simulation): a finite element-based multi-physics modelling and simulation tool.", (2024)
- [7] Gschwentner, A. and Roppert, K. and Kaltenbacher, M., "Determination of Local Magnetic Material Properties Using an Inverse Scheme", IEEE Transactions on Magnetics Vol. 60 3, (2024)
- [8] Bates, D. M. and Watts, D. G., "Nonlinear Regression Analysis and Its Applications", New York: Wiley, (1988)
- [9] McKay, M. D., Beckman, R. J. and Conover, W. J., "A Comparison of Three Methods for Selecting Values of Input Variables in the Analysis of Output from a Computer Code", Technometrics, 21(2), 239-245. doi:10.1080/00401706.1979.10489755, (1979)
- [10] Williams, Christopher, and Carl Rasmussen. "Gaussian processes for regression." Advances in neural information processing systems 8 (1995).
- [11] Dietterich, T. G. "Ensemble Methods in Machine Learning", In J. Kittler Additionally F. Roli (Eds.), Multiple Classifier Systems (pp. 1-15). Springer, (2000)
- [12] Pedregosa, F., Varoquaux, G., Gramfort, A., Michel, V., Thirion, B., Grisel, O., Blondel, M., Prettenhofer, P., Weiss, R., Dubourg, V., Vanderplas, J., Passos, A., Cournapeau, D., Brucher, M., Perrot, M. and Duchesnay, É., "Scikit-learn: Machine Learning in Python", Journal of Machine Learning Research, 12, 2825-2830. (2011)

# Sequential Bayesian Experimental Design for Efficiency Maps using Gaussian Processes

A. Reinbacher-Köstinger\*, P. K. Dhakal<sup>†</sup>, K. Heidarikani<sup>†</sup>, E. Mušeljić\*, T. Komann<sup>‡</sup>, A. Muetze<sup>†</sup>, S. Ulbrich<sup>‡</sup> and M. Kaltenbacher\*

\*Institute of Fundamentals and Theory in Electrical Engineering, TU Graz, Inffeldgasse 18/1, 8010 Graz, Austria 

†Institute of Electric Drives and Power Electronic Systems, TU Graz, Inffeldgasse 18/1, 8010 Graz, Austria

†Department of Mathematics, TU Darmstadt, Dolivostraße 15, 64293 Darmstadt, Germany

E-mail: alice.koestinger@tugraz.at

Abstract—This work presents a design of experiments approach to determine the required number and optimal locations of sampling points in an efficiency map to perform an accurate yet resource-efficient drive cycle analysis of an electric machine. Gaussian processes are used to predict the efficiency at the operating points associated with the drive cycle and simultaneously determine the uncertainties of these predictions. The study considers two distinct use cases: the first aims to achieve a robust general interpolation of efficiency across the entire map, while the second focuses on devising an optimal sampling plan to optimize motor performance throughout the entire drive cycle.

Index Terms—Optimal design of experiments, Gaussian Process Regression, efficiency map.

#### I. INTRODUCTION

Drive cycles, such as the Worldwide Harmonized Light Vehicle Test Procedure (WLTP) are used to assess the energy consumption and emissions of a given vehicle in a standardized way [1]. Often, electric machines, when designed for electric traction applications, are evaluated against such driving profiles using look-up tables in the form of efficiency maps. These maps are typically determined using a grid-based approach, which is time consuming, and there is uncertainty on the grid density to be chosen to achieve the desired degree of accuracy [2]. The iterative nature of evaluating efficiency maps for each new design proposal within an optimization framework adds significantly to the time required.

Alternative sampling strategies, such as Latin hypercube or Sobol sequences, offer potential improvements by avoiding the exhaustive grid point computations. However, these methods require a predefined sample size and the resulting uncertainty of interpolated efficiency values is unknown. In [3] and [4] metamodels using deep learning and Kriging, respectively, have been explored for efficiency prediction. Such approaches can be very useful when used in an optimization procedure, but they require a lot of training data in advance, which is then only valid for a particular optimization parameter set.

To address these challenges, adaptive sequential sampling via Gaussian Process Regression (GPR) presents a robust alternative both in terms of handling measurement noise and determining the minimum number of sampling points. This method allows for dynamic evaluation of the necessary sample size to achieve a desired confidence level throughout the sampling process. GPR not only facilitates precise value predictions but also quantifies uncertainty at any point of interest. This dual capability is ideal for experimental design, enabling precise identification of optimal sampling points. This approach minimizes interpolation errors and reduces the need for extensive

data collection, thereby enhancing the efficiency of the design process [5]. Within the optimization process, the sample size can vary for each newly proposed design, resulting in an approach that is both extremely efficient and flexible while providing very accurate solutions.

#### II. GAUSSIAN PROCESSES

Gaussian Process Regression is a Bayesian nonparametric method used to infer continuous functions from data [6]. It is particularly advantageous due to its flexibility and the intrinsic ability to quantify uncertainty in predictions [7].

A Gaussian Process (GP) is fully specified by a mean function m(x) and a covariance function k(x,x'), where x and x' are points in the input space. Typically, the mean function is taken as zero m(x)=0 for simplicity, unless prior knowledge suggests a more informative mean. The power of GP regression largely stems from the choice of the covariance function, which encodes assumptions about the function being learned, such as smoothness and periodicity.

#### Covariance Functions

The covariance function  $K(\boldsymbol{x}, \boldsymbol{x}')$ , also known as the kernel, defines the expected covariance between the function values at two points in a p-dimensional input space. A popular choice for the kernel is the Squared Exponential (SE) kernel, also referred to as the Radial Basis Function (RBF) kernel, defined as

$$K(x, x') = \exp\left(-\frac{1}{2}\sum_{i=1}^{p} \frac{(x_i - x_i')^2}{l_i^2}\right),$$
 (1)

where l is the vector of length-scales, with each component  $l_i$  specifying the characteristic length scale in the corresponding dimension of the input space. This parametrization allows the kernel to adapt its sensitivity

to differences in each dimension of the input, thus controlling the smoothness of the function modeled in each respective dimension. This kernel assumes that the function outputs are normally distributed, with mean zero and variance defined by the kernel.

Other kernels can be used depending on the properties desired in the function, such as the Matérn, Rational Quadratic, or Periodic kernels, each introducing different characteristics into the function behavior.

#### Training the Gaussian Process

Given a training set  $\{(\boldsymbol{x}_i, y_i)\}_{i=1}^n$ , where  $\boldsymbol{y}$  represents n observations, the combination of the GP prior and the data likelihood leads to the posterior distribution over functions. The joint distribution of the observed target values and the function values at a new test point  $\boldsymbol{x}_*$  under the GP model is described by:

$$\begin{bmatrix} \boldsymbol{y} \\ f(\boldsymbol{x}_*) \end{bmatrix} \sim \mathcal{N} \left( \boldsymbol{0}, \begin{bmatrix} K(\boldsymbol{X}, \boldsymbol{X}) + \sigma_{\mathrm{d}}^2 \boldsymbol{I} & K(\boldsymbol{X}, \boldsymbol{x}_*) \\ K(\boldsymbol{x}_*, \boldsymbol{X}) & K(\boldsymbol{x}_*, \boldsymbol{x}_*) \end{bmatrix} \right), \quad (2)$$

where  $K(\boldsymbol{X}, \boldsymbol{X})$  is the covariance matrix computed between all pairs of training inputs,  $K(\boldsymbol{X}, \boldsymbol{x}_*)$  is the covariance between the training inputs and the test input and  $\boldsymbol{I}$  is the identity matrix. In cases using measurements as observations, noise is typically assumed to be Gaussian,  $y_i = f(x_i) + \eta$ , with  $\eta \sim \mathcal{N}(0, \sigma_{\rm d}^2)$  and  $\sigma_{\rm d}$  denoting the data noise variance. The length scales in the GP model are optimized by maximizing the marginal likelihood of the training data using gradient-based optimization methods, which adjust the scales to best capture the dependencies of inputs on outputs. These optimized length scales are then used in the kernel for the prediction and uncertainty quantification.

#### Prediction

The posterior distribution for  $f(x_*)$  given the data is also Gaussian, defined by the posterior mean and variance

$$\mu(\boldsymbol{x}_*) = K(\boldsymbol{x}_*, \boldsymbol{X})[K(\boldsymbol{X}, \boldsymbol{X}) + \sigma_{\mathrm{d}}^2 \boldsymbol{I}]^{-1} \boldsymbol{y}, \quad (3)$$

$$\sigma^2(\boldsymbol{x}_*) = K(\boldsymbol{x}_*, \boldsymbol{x}_*) - K(\boldsymbol{x}_*, \boldsymbol{X})[K(\boldsymbol{X}, \boldsymbol{X}) + \sigma_{\mathrm{d}}^2 \boldsymbol{I}]^{-1} K(\boldsymbol{X}, \boldsymbol{x}_*), \quad (4)$$

where  $\mu(x_*)$  is the best prediction of the function at  $x_*$  and  $\sigma^2(x_*)$  quantifies the prediction's uncertainty. This uncertainty is crucial for applications like active learning, because it is used as a measure for selecting the new data point to be added to the training set. The standard deviation  $\sigma$  can be used to compute a 95% confidence interval for predictions, offering a robust measure of the reliability of the predictions.

### III. SEQUENTIAL BAYESIAN EXPERIMENTAL DESIGN APPROACH

The proposed methodology starts with the definition of candidate points  $X_{\mathrm{cand}}$ . These points represent a set

of operating points from which the algorithm, during the sequential procedure, selects new samples based on their uncertainty. Since this stage involves only specifying inputs without calculating their corresponding outputs, the candidate set can be extensive. Subsequently, a small initial dataset,  $X_{\mathrm{init}}$ , is chosen from the candidate set. The size of this initial dataset is often found to be somewhat arbitrary in the literature [8]. It is generally influenced by the problem's dimensionality and the associated computational costs. Therefore, the initial dataset should be kept as small as feasible, yet it must exceed the dimensionality of the problem, which in this case is two (torque and speed). The sampling points are chosen by applying a K-Means algorithm in order to get well distributed points within predefined bounds. These points serve as the training data for a Gaussian Process (GP) model and are denoted by  $X_{
m active}$ . The respective output  $f(oldsymbol{X}_{\mathrm{active}})$  represents efficiency calculations derived from an analytical model as outlined in Sec. IV in this work. It is important to emphasize that the primary motivation for implementing the proposed experimental design approach is to minimize the computational effort associated with complex, time-consuming models, such as finite element models. Notably, the procedure described here is flexible; the model is exchangeable, and even direct measurements could be integrated as an alternative. The uncertainty of the model predictions, defined by the posterior covariance in (4), is readily computed for any candidate sampling point using the trained GP. Subsequently, new samples are strategically added based on their associated uncertainties from the set of candidate points. The GP model is then iteratively retrained with the updated dataset. This process continues until the uncertainty associated with all sampling points in the domain falls below a specified threshold  $\epsilon$ , indicating sufficient model precision and reliability. The procedure is shown in Fig. 1.

To analyze the proposed approach, the Root Mean Square Error (RMSE) between the predictions  $\hat{f}(\boldsymbol{X})$ , which are the mean values according to (3), and the observations  $f(\boldsymbol{X})$ , that can be measurements or model outputs, is evaluated for N test points by

$$RMSE(\boldsymbol{X}) = \sqrt{\frac{1}{N} \sum_{i=1}^{N} \left(\hat{f}_i(\boldsymbol{x}_i) - f_i(\boldsymbol{x}_i)\right)^2}, \quad (5)$$

where  $x_i$  is the *i*-th row vector of X. The test points  $X_{\text{test}}$  must be distinct from the candidate points to ensure their values are not inherently zero. It is worth noting that error calculations are not part of the optimal sampling point identification process, and the corresponding model output evaluations are not part of the computational effort required to develop an effective GPR model.

#### IV. EFFICIENCY MAP AND DRIVE CYCLE

In order to show the feasibility of the proposed method for identifying the number and location of sampling points for efficiency analysis, an analytical model is used.

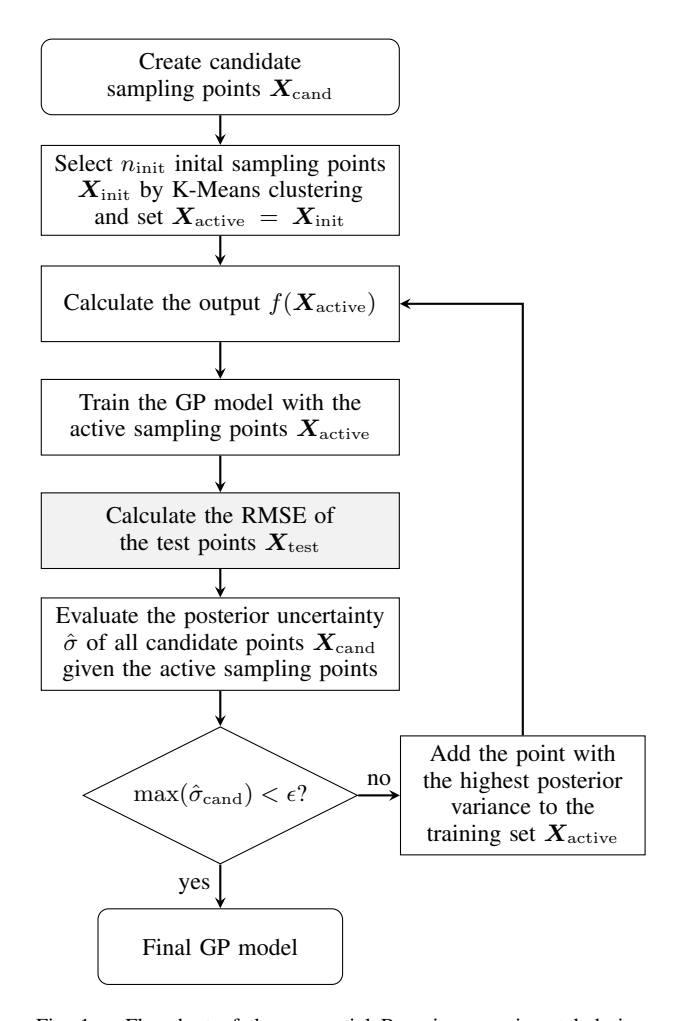


Fig. 1. Flowchart of the sequential Bayesian experimental design. The grey-colored block is only needed for the analysis of the error convergence and is not used for finding the optimal sampling points. Thus, the related efforts do not count for the efficiency of the proposed method.

This section describes the evaluation of operating points from drive cycles and the calculation of the efficiency for a specific Permanent Magnet Synchronous Motor (PMSM) design.

Drive cycle

A drive cycle is a time-based pattern of vehicle speed designed to mimic typical real-world driving conditions for specific regions or cities, such as the WLTP and Artemis [9]. For each drive cycle, the required torque is determined using a mechanical model of the vehicle. However, the actual drive cycles of a vehicle cannot be directly tested in a laboratory due to the limited ranges of testing equipment. Thus, these drive cycles must be appropriately scaled down. For instance, in the context of the PMSM discussed in this study, the torque-speed points corresponding to the drive cycle are derived using the down-scaling method outlined in [10].

Efficiency calculation

For a given motor operating point, i.e. torque-speed point  $(T, \omega)$ , the efficiency in percent is obtained by,

$$\eta(T,\omega) = \frac{P_{\text{output}}(T,\omega)}{P_{\text{input}}(T,\omega)} \cdot 100\%, \qquad (6)$$

which can be expended as,

$$\eta(T,\omega) = \frac{T\omega}{T\omega + P_{\text{losses}}(T,\omega)} \cdot 100\%,$$
(7)

where  $P_{\text{losses}}$  incorporates copper, iron a no load losses:

$$P_{\text{losses}}(T,\omega) = P_{\text{cu}}(T) + P_{\text{iron}}(\omega) + P_{\text{no\_load}}(\omega)$$
. (8)

The copper losses are calculated using the phase current corresponding to the motor torque and the resistance in the windings:

$$P_{\rm cu}(T) = 3 I_{\rm phase}^2(T) R_{\rm phase}. \tag{9}$$

The total iron losses consisting of hysteresis, eddy current and excess loss, are calculated with the well known Steinmetz equation [11],

$$P_{\text{iron}}(\omega) = k_{\text{h}} f(\omega) B_{\text{m}}^2 + k_{\text{e}} f^2(\omega) B_{\text{m}}^2 + k_{\text{ex}} f^{1.5}(\omega) B_{\text{m}}^{1.5},$$
 (10)

with the maximum flux density  $B_{\rm m}$  and the motor operating frequency f that corresponds to the motor speed  $\omega=2\pi f$ . The coefficients  $k_{\rm h},k_{\rm e}$  and  $k_{\rm ex}$  are determined using a curve fitting toolbox in MATLAB, based on the manufacturer's data for the steel used in the motor. The values of these coefficients are provided in Tab. I.

Parameter	Value
$R_{\rm phase}$	$8.9462\Omega$
$k_1$	$5.32 \times 10^{-5}$
$k_2$	$5.04 \times 10^{-9}$
$k_h$	0.0183
$k_e$	$2.88 \times 10^{-5}$
$k_{ex}$	$4.71 \times 10^{-4}$
$B_{ m m}$	$0.4147\mathrm{T}$

TABLE I
MODEL PARAMETERS FOR EFFICIENCY CALCULATION.

The no-load losses are calculated with the no-load torque and the speed,

$$T_{\text{no\_load}}(\omega) = k_1 N_{\text{rpm}}^{0.4}(\omega) + k_2 N_{\text{rpm}}^{1.5}(\omega)$$
$$P_{\text{no\_load}}(\omega) = \omega T_{\text{no\_load}}(\omega), \qquad (11)$$

with  $N_{\rm rpm}=\frac{30}{\pi}\,\omega$ . The loss coefficients are derived using curve fitting toolbox in MATLAB, based on the no load torque measurements of the PMSM in the laboratory at different rotor speeds.

#### V. RESULTS

All investigations were done using a motor design with the parameters given in Tab. I. The corresponding efficiency map and the operating points of the two drive cycles are illustrated in Fig. 2.

Two different use cases have been analyzed in this study. The first use case (use case 1) is aimed at developing an

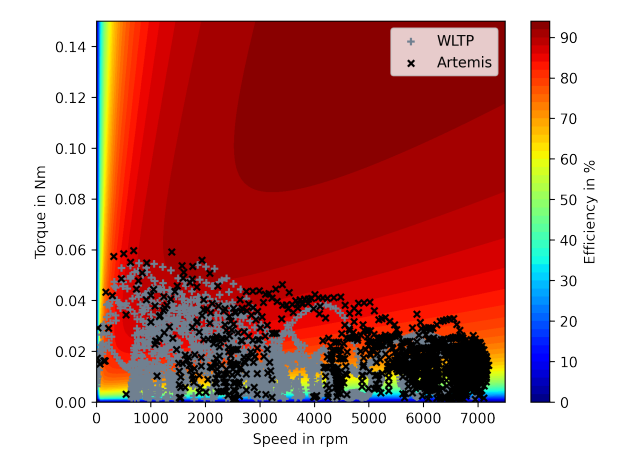


Fig. 2. Efficiency map and operating points of the drive cycles WLTP and Artemis.

optimal sampling strategy for the entire efficiency map, with the objective of providing a robust general interpolation. The second use case (use case 2) is specifically tailored for motor design optimization, where each new design iteration requires evaluations at multiple operating points along a defined drive cycle. Consequently, the primary goal of use case 2 is to optimize the sampling plan within the region of the efficiency map that corresponds to the operating points of the drive cycle, excluding areas that are not relevant to the cycle.

The key distinction between these two use cases lies in the definition of candidate points. For use case 1, a dense and uniform grid of candidate points is generated within the bounds of the efficiency map, ensuring comprehensive coverage. In contrast, for use case 2, the candidate points are directly derived from the trajectory of operating points related to the drive cycle.

It should also be noted that all input variables were normalized to the unit range [0,1] during the process to ensure compatibility with GP models. A Squared Exponential kernel, as described in (1), was employed for both use cases. Additionally, the length scale parameters of the kernel were automatically optimized during the GP model training to adapt to the specific characteristics of the data.

#### A. Use case 1

The candidate points  $\boldsymbol{X}_{\mathrm{cand}}$  for this use case are generated as grid data within the  $(\omega,T)$  range of the efficiency map. These points define the maximum number of potential sampling points, given by  $n_{\mathrm{cand}} = n_{\omega} \cdot n_{\mathrm{T}}$ . For the approach outlined in Sec. III, a candidate set of  $n_{\mathrm{cand}} = 200 \cdot 200 = 40,000$  was generated within the parameter ranges  $\omega \in [0,7500]$  and  $T \in [0,0.14]$ . Starting with an initial dataset  $(\boldsymbol{X}_{\mathrm{init}},f(\boldsymbol{X}_{\mathrm{init}}))$  containing only 3 samples, the sequential algorithm identified the optimal sampling points, which converged at 100 sampling points, as shown in Fig. 3.

The optimized sampling points are well distributed across the efficiency map domain, with some regions of

higher uncertainty exhibiting a wider spread of points. The final model, trained using 100 sampling points, achieved an anisotropic length scale of  $\boldsymbol{l} = [0.09, 0.11]$  for the speed and the torque, respectively.

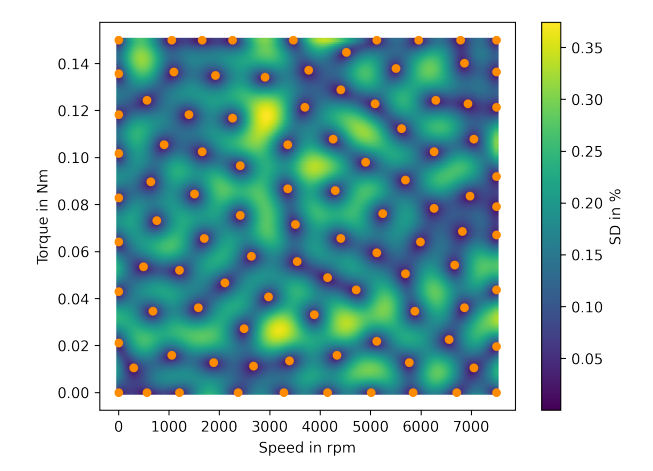


Fig. 3. Standard deviation of the efficiency using the optimized sampling points.

Figure 4 illustrates the resulting prediction error computed on a fine grid across the efficiency map. Higher errors are observed in regions with low torque and low speed. This is attributed to the shape of the efficiency function, which exhibits steep gradients near the lower boundaries and remains relatively flat elsewhere.

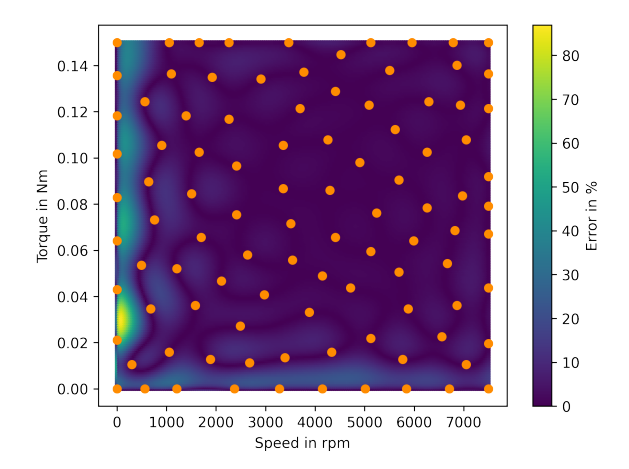


Fig. 4. Optimized sampling points and prediction error across the efficiency map.

The convergence of the Root Mean Square Error (RMSE) is depicted in Fig. 5, evaluated on a set of randomly generated test points across the efficiency domain. The RMSE for the operating points of the WLTP and Artemis drive cycles is also shown. Both exhibit similar trends; however, the results of the WLTP drive cycle, primarily designed for city-mode operation, displays slightly higher errors due to the greater prediction errors at low speeds. The mean standard deviation, computed across all candidate points, closely mirrors the RMSE trends. This correlation enables the use of the standard deviation as a

stopping criterion for the algorithm, eliminating the need for additional, time consuming efficiency evaluations in order to determine the RMSE.

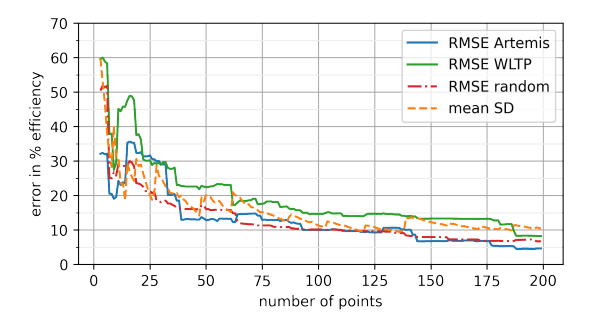


Fig. 5. Error and uncertainty of the efficiency prediction as a function of the number of training points. The error is evaluated for the operating points of the two drive cycles as well as for randomly distributed test points of the efficiency map (use case 1).

#### B. Use case 2

The design of a traction motor should be optimized for at least one drive cycle to achieve a well-balanced machine. During the optimization process, the efficiency map evolves with each newly proposed design, necessitating the creation of a new surrogate model for efficiency prediction. Therefore, it is crucial to identify a minimal number of optimal sampling points that ensure a low RMSE of the efficiency along the operating points of the drive cycle.

For this use case, the drive cycle-related operating points are considered as candidate points instead of grid points like in the first use case. In each iteration of the adaptive sampling procedure, the operating point with the highest posterior uncertainty is added to the training set of the GP model. This strategy ensures that the sampling plan focuses on regions most critical to the drive cycle, leading to efficient and accurate predictions.

The resulting sampling plan, along with the corresponding prediction error, is illustrated in Fig. 6. It can be observed that the sampling points are concentrated along the trajectory of the operating points of the drive cycle, effectively minimizing errors in these regions.

Figure 7 shows the convergence of the RMSE for both drive cycles, but with candidates taken only from the WLTP drive cycle. Similarly, Fig. 8 presents the error convergence taking the operating points of both the WLTP and Artemis drive cycles into account. The results highlight the effectiveness of the proposed adaptive sampling strategy, which achieves significant error reduction with a minimal number of sampling points. For instance, stopping at a posterior standard deviation of 10% requires only 35 samples and corresponding efficiency evaluations, whereas achieving the same uncertainty level in use case 1 demands more than 100 samples. Furthermore, the associated RMSE for this use case is significantly lower than in use case 1, remaining below 8%.

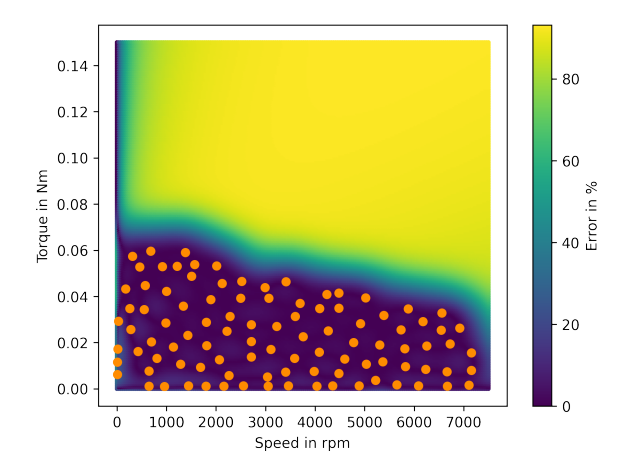


Fig. 6. Locations of the optimized sampling points and prediction error (color) for use case 2, which aims to reduce the error for the operating points of the drive cycle.

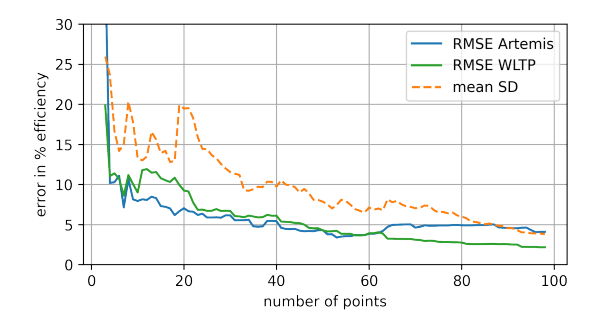


Fig. 7. Error and uncertainty of the efficiency prediction for use case 2. Only operating points of the WLTP drive cycle are considered as training points in the GP model. However, the prediction error associated with the Artemis drive cycle is just as small.

#### VI. CONCLUSION

This study has successfully demonstrated a novel experimental design approach using Gaussian Process Regression to efficiently and effectively determine the optimal number and location of sampling points on an efficiency map for electric machines undergoing drive cycle analysis. Through the utilization of Gaussian Processes, the study addresses the common challenges associated with traditional grid-based sampling methods, offering a dynamic and adaptive solution that significantly reduces the need for extensive data collection while enhancing the accuracy of efficiency predictions.

The two distinct use cases presented illustrate the versatility and applicability of the proposed method. The first use case highlights the ability to achieve a robust general interpolation across the entire efficiency map, which is essential for general performance evaluation and preliminary design stages. The second use case focuses on optimizing the sampling strategy specifically tailored for motor design optimization, emphasizing efficiency in the regions most critical during actual drive cycles. For example, the optimization efforts described in [12] and [13] initially focused on single operating points, but will soon expand to include investigations at multiple

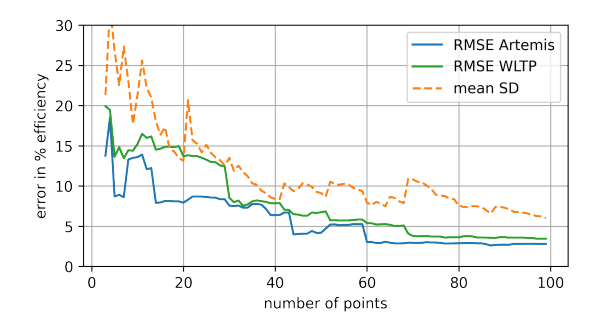


Fig. 8. Error and uncertainty of the efficiency prediction for use case 2. Operating points of both the WLTP and Artemis drive cycle are considered as training points in the GP model.

operating points. This development will provide a more comprehensive understanding of engine behavior under different conditions, ultimately leading to better and more efficient engine designs.

The results from both use cases demonstrate substantial improvements in sampling efficiency and prediction accuracy, with a significant reduction in the number of required samples to achieve high confidence levels in the efficiency predictions. The adaptive nature of the sampling strategy, guided by the quantified uncertainties from the GPR model, ensures that each new data point maximizes the potential to refine the model, thereby streamlining the development process of more efficient and effective electric machines.

#### ACKNOWLEDGMENT

This work is partially supported by the joint Collaborative Research Centre CREATOR (DFG: Project-ID 492661287/TRR 361; FWF: 10.55776/F90) at TU Darmstadt, TU Graz and JKU Linz.

#### REFERENCES

- BMW, "WLTP: New Times, New Rules." https://www.bmw.com/en/innovation/wltp.html, 2024. Accessed: Aug. 19, 2024.
- [2] E. Roshandel, A. Mahmoudi, S. Kahourzade, and W. L. Soong, "Efficiency maps of electrical machines: A tutorial review," *IEEE Transactions on Industry Applications*, vol. 59, pp. 1263–1272, Mar 2023.
- [3] A. Khan, M. H. Mohammadi, V. Ghorbanian, and D. Lowther, "Efficiency map prediction of motor drives using deep learning," *IEEE Transactions on Magnetics*, vol. 56, no. 3, pp. 1–4, 2020. Conference Name: IEEE Transactions on Magnetics.
- [4] M. Djami, M. Hage-Hassan, C. Marchand, G. Krebs, P. Dessante, and L. Belhaj, "Kriging metamodel for electric machines: A drive cycle approach," in 2022 International Conference on Electrical Machines (ICEM), pp. 251–256, 2022. ISSN: 2381-4802.
- [5] P. Pandita, P. Tsilifis, N. M. Awalgaonkar, I. Bilionis, and J. Panchal, "Surrogate-based sequential bayesian experimental design using non-stationary gaussian processes," *Computer Methods in Applied Mechanics and Engineering*, vol. 385, p. 114007, 2021.
- [6] B. Shahriari, K. Swersky, Z. Wang, R. P. Adams, and N. de Freitas, "Taking the human out of the loop: A review of bayesian optimization," *Proceedings of the IEEE*, vol. 104, no. 1, pp. 148–175, 2016.
- [7] C. E. Rasmussen and C. K. I. Williams, Gaussian Processes for Machine Learning. The MIT Press, 2006.
- [8] J. N. Fuhg, A. Fau, and U. Nackenhorst, "State-of-the-art and comparative review of adaptive sampling methods for kriging," vol. 28, no. 4, pp. 2689–2747.

- [9] DieselNet, "Emission Test Cycles," 2011. available at: https://dieselnet.com/standards/cycles/index.php (accessed 23 September 2024)
- [10] P. K. Dhakal, K. Heidarikani, and A. Muetze, "Down-scaling of drive cycles for experimental drive cycle analyses," in 12th International Conference on Power Electronics, Machines and Drives (PEMD 2023), vol. 2023, (Brussels, Belgium), pp. 271– 276, Oct. 2023.
- [11] A. Krings and J. Soulard, "Overview and comparison of iron loss models for electrical machines," in MC2D & MITI Conference, 2010.
- [12] M. Wiesheu, T. Komann, M. Merkel, S. Schöps, S. Ulbrich, and I. Cortes Garcia, "Combined parameter and shape optimization of electric machines with isogeometric analysis,"
- [13] T. Komann, M. Wiesheu, S. Ulbrich, and S. Schöps, "Robust design optimization of electric machines with isogeometric analysis," *Mathematics*, vol. 12, no. 9, 2024.

## Finite element modeling of eddy currents in a multiconductor system with quasi-2D symmetry

Bakondi Tamás, Gyimóthy Szabolcs, Bilicz Sándor

Budapest University of Technology and Economics, Hungary

#### Purpose:

The purpose of this paper is to introduce a fast and resource-efficient method for modeling litz wires with complex structures. The method is also capable of taking into account nonlinear materials in the configuration (e.g. ferrite-core coil).

#### Design/methodology/approach:

The modeling of litz wires is performed in two-dimensional (2D), with the key being the proper consideration of three dimension (3D) phenomena (twisting, constraints resulting from braiding, winding and the circuit constraints) in 2D. These phenomena can be taken into account through specific constraint conditions, which, when incorporated into the boundary value problem equations, enable the system of equations to be solved in a single step.

#### Findings:

With the developed method, 3D problems related to wire modeling can be solved in 2D by eliminating superposition. As a result, the model can handle nonlinearities such as a magnitude-dependent complex permeability, allowing for the modeling of ferrite-core coils as well. A comparison between a simple 2D-3D model example demonstrates significant time savings, while the 2D model reproduces the results of the 3D model fairly well. The 2D model can also be extended to wires with more complex structures, the modeling of which in 3D would require extremely high computational power, if feasible at all.

#### Originality/value:

This paper shows the applicability of the 2D model as a substitute for the 3D model by showing the agreement of the results, as well as the savings in computation time and performance.

#### Keywords:

FEM, Eddy currents, Litz wire, Complex permeability

## An air-gap element for the isogeometric space-time simulation of electric machines

Reichelt Michael (1, 2), Merkel Melina (2), Schöps Sebastian (2), Steinbach Olaf (1)

(1) Institute of Applied Mathematics, Graz University of Technology, Graz, Austria (2) Chair of Computational Electromagnetics, Technische Universität Darmstadt, Darmstadt, Germany

#### Purpose:

Space-time methods promise more efficient time-domain simulations, in particular of electrical machines. However, most approaches require the motion to be known in advance so that it can be included in the space-time mesh. The purpose of this paper is to overcome this problem by proposing the use of the well-known air-gap element for rotor-stator coupling of an isogeometric machine model.

#### Design/methodology/approach:

First, the authors derive the solution in the air-gap region and then use it to couple the rotor and stator. This coupling is angle dependent and the authors show how to efficiently update the coupling matrices to a different angle, avoiding expensive quadrature. Finally, the resulting time-dependent problem is solved in a space-time setting.

#### Findings:

Spatial discretization using isogeometric analysis is particularly suitable for coupling via the air-gap element, as nonuniform rational B-splines can exactly represent the geometry of the air gap. Furthermore, the model including the air-gap element can be seamlessly transferred to the space-time setting.

#### Originality/value:

The air-gap element is well known in the literature. The originality of this work is the application to isogeometric analysis and space-time.

#### **Keywords:**

Electrical machine, Isogeometric analysis, Space-time finite elements, Domain decomposition, Air-gap element

 $\textbf{Published} \ \ \text{in COMPEL-The international journal for computation and mathematics in electrical and electronic engineering, Vol. 44 No. 5, 2025, ISSN 0332-1649, doi: https://doi.org/10.1108/COMPEL-01-2025-0025 | https://doi.org/10.1108/COMPEL-0$ 

#### An effective interface formulation for electromagnetic shielding using the A-formulation in 3D

Schöbinger Markus, Leumüller Michael, Hollaus Karl $TU\ Wien,\ Austria$ 

#### Purpose:

The purpose of this paper is to present an effective material approach to simulate electromagnetic shields using the A-Formulation in a fully 3D setting with nonlinear materials in the frequency domain. It allows to treat the shield as an interface in the finite element mesh so that only the magnetic vector potential in the surrounding air has to be considered for the solution.

#### Design/methodology/approach:

The jump of the tangential components of the potential across the interface is controlled by an effective material parameter based on a suitable cell problem. This parameter can be efficiently interpolated from a precomputed look-up table.

#### Findings:

The method is able to consider curved shields and holes. A numerical example shows an excellent agreement of the presented method compared to a reference solution both in a global and a local sense.

#### Originality/value:

A novel effective material approach based on numerical solutions of a suitable nonlinear cell problem is presented.

#### **Keywords:**

Electromagnetic shielding, Thin shell model, Effective material, Eddy currents, Electromagnetic fields, Magnetic shielding, Homogenization method

## Relating transmission line overvoltages and lightning location: a machine learning-based procedure

Barmada Sami (1), Brignone Massimo (2), Dodge Shayan (1), Nicora Martino (2), Procopio Renato (2), Tucci Mauro (1)

(1) University of Pisa, Italy(2) University of Genova, Italy

#### Purpose:

This study aims to investigate the use of machine learning—based algorithms in the field of lightning stroke localization. This work is an important step ahead with respect to the research recently started by the authors, i.e. the possibility of locating a lightning discharge from the voltage induced on overhead transmission lines; more in detail it seeks new insights into the inclusion of both first and subsequent return strokes of negative cloud-to-ground flashes.

#### Design/methodology/approach:

This study uses a quantitative approach, using supervised learning techniques for a regression problem (data preprocessing, model selection, training, testing, validation or algorithm optimization). Data are collected from a dedicated lightning-induced overvoltage simulator and analyzed using a specific machine learning—based procedure developed and programmed by the authors.

#### Findings:

The results reveal significant improvements in localization accuracy for both first and subsequent strokes, with respect previous works, indicating that the novel approach is promising for future investigation with more complex power system configurations and the use of experimental data. These findings provide evidence that dedicated models for each type of stroke yield better performance, offering significant implications for the integration of machine learning—based lightning location systems into the existing power infrastructure.

#### Originality/value:

The proposed method is, to the best of the authors' knowledge, entirely new and constitute an innovation with respect to the present literature, both of the same authors and of other research groups. In particular, a new preprocessing procedure of the voltage data is proposed, and the performances of different neural networks are evaluated, both for the first and the subsequent stroke. The application to both first and subsequent stroke is an innovation itself because it has not been proposed before.

#### **Keywords:**

Machine learning, Lightning-induced voltage, Lightning location, Transmission lines

#### Evaluation of a control-oriented single-phase transformer core model

Schwartze Nicolai (1, 2), Moschik Sonja (2), Reichhartinger Markus (1)

(1) Graz University of Technology, Austria (2) OMICRON electronics GmbH

#### Purpose:

This paper aims to address the limitations of existing transformer core models, which often lack applicability in real-time control tasks. The paper investigates properties of a control-oriented transformer core model that is shown to accurately represent the effects of hysteresis, saturation, eddy current losses and leakage flux while at the same time minimizing the computational burden.

#### Design/methodology/approach:

The investigated control-oriented model is mathematically expressed in a state-space form, making it inherently suitable for model-based controller design. This model can be interpreted as an equivalent electric diagram, providing a clear and intuitive representation. The model is experimentally evaluated across various transformers which are selected based on an extensive data analysis aimed at identifying practically relevant representatives. The k-means clustering algorithm is used to ensure that the transformers exhibit fundamentally different characteristics.

#### Findings:

The investigated control-oriented model successfully fulfils its purpose. It effectively replicates the transient current response of various current transformers and generalizes well across a wide range of input signals with minimal computational effort.

#### Originality/value:

Comparing the proposed control-oriented model with the Jiles-Atherton model demonstrates its effectiveness in terms of simulation accuracy and computational efficiency. Therefore, it offers a practical solution for problems commonly found in real-time control applications.

#### **Keywords:**

Control-Oriented model, Hysteresis model, Data analysis, Current transformer

## Computational efficient single component Gibbs sampling for electrical tomography

Neumayer Markus (1), Suppan Thomas (1), Bretterklieber Thomas (1), Wegleiter Hannes (1), Fox Colin (2)

Graz University of Technology, Austria
 University of Otago, New Zealand

#### Purpose:

In Bayesian inversion, the Gibbs sampler draws samples from the multivariate posteriori distribution by sequentially sampling from the conditional distributions of the individual parameters. This makes Gibbs sampling a preferable sampling technique with respect to other Markov chain Monte Carlo (MCMC) methods, e.g. the Metropolis Hastings algorithm, yet the evaluation of the conditional distributions is computationally expensive. This paper aims to present an efficient technique based on the Woodbury matrix identity to evaluate the conditional distributions of electrical tomography problems with an underlying finite element (FE) simulation.

#### Design/methodology/approach:

The approach is based on a modified solution strategy of the used FE sensor simulation model. The computation of the conditional distribution requires the evaluation of the FE model for changes of the electrical material parameter of a single FE. This is formulated as a low rank update of the FE stiffness matrix. Using the modified solution approach, the change of the FE model output can be exactly evaluated by means of the Woodbury matrix identity.

#### Findings:

Simulation results show a computational speed up of a Gibbs sampler with the proposed scheme for an electrical capacitance tomography example by a factor of at least 30 with respect to a standard implementation, i.e. without the Woodbury matrix identity. The algorithm has a short burn in phase and is able to provide independent samples by each sweep over the state vector.

#### Originality/value:

This paper shows a technique for the efficient evaluation of the conditional distribution for electrical tomography problems with an underlying FE simulation model. The derivation and implementation is coherent with the modified sensor simulation approach. The approach can also be applied within other inverse problems or algorithms, e.g. optimization-based techniques.

#### **Keywords:**

Gibbs sampling, ECT, FE simulation, Woodbury matrix identity

## Predicting torque characteristics of synchronous reluctance motors using swin transformer

Nagayama Taisuke, Sasaki Hidenori

Hosei University, Japan

#### Purpose:

The purpose of this study is to propose a novel prediction model for motor characteristics in the topology optimization (TO) of synchronous reluctance motors (SynRMs) using a Swin Transformer (ST) model. It was demonstrated that ST exhibits superior prediction accuracy compared to the convolutional neural network (CNNs) method for SynRMs. The attention mechanism that constitutes ST is employed to visualize the characteristic contribution region of the SynRMs.

#### Design/methodology/approach:

The ST model was trained using datasets generated by TO. These datasets represent the material distributions in the SynRM rotors and their associated torque characteristics. The ST architecture uses a window-based, multihead self-attention mechanism to capture global and local image features. The prediction accuracy of the average torque or peak-to-peak value of the torque was evaluated against the finite element method results, with CNNs serving as the baseline.

#### Findings:

Compared with CNNs, the proposed method improves accuracy by up to 56.8% in terms of the mean square error of the average torque. Furthermore, the visualization method using the attention mechanism of ST effectively captured the material boundary features. The ST model has the potential to make accurate and interpretable predictions.

#### Originality/value:

The proposed method constitutes a novel approach to the application of ST for the prediction of SynRMs. This approach addresses both predictive accuracy and explainability. The proposed method will be applied to TO and will extend the prediction targets to other characteristics of motors.

#### **Keywords:**

Topology optimization, Finite element method, Electrical machine

## Effective material modelling for laminated iron cores with an A-formulation and circuit coupling

Hanser Valentin, Schöbinger Markus, Hollaus Karl $TU\ Wien,\ Austria$ 

#### Purpose:

This study aims to introduce an effective material to efficiently and accurately solve the eddy current problem in laminated iron cores considering circuit coupling.

#### Design/methodology/approach:

In the first step, a representative cell problem is solved to obtain the complex-valued non-linear magnetic reluctivity. In the second step, this effective material is then used in a homogenised static magnetic field formulation and accurately approximates the eddy current losses and the reactive power as well as the corresponding distributions.

#### Findings:

As a representative numerical example, a voltage-driven single-phase transformer is simulated with great success. The eddy current losses and the reactive power of the simulation using the standard finite element method and the simulation using the effective material agree very well and the required simulation time is tremendously reduced.

#### Originality/value:

The presented approach uses an A-formulation with circuit coupling of voltage-driven excitation coils for an effective material to homogenise the core.

#### **Keywords:**

Eddy currents, Material modelling, Magnetic non-linearity, Lamination modelling, Homogenisation method

### Emulation of photovoltaic arrays under non-uniform environmental conditions

#### Dimitrijević Marko, Petronijević Milutin

Faculty of Electronic Engineering, University of Niš, Serbia

#### Purpose:

The purpose of this manuscript is to present a method for emulating photovoltaic (PV) arrays under non-uniform environmental conditions such as illumination, temperature and soiling using a programmable power supply.

#### Design/methodology/approach:

A key element of the emulation method is generating the characteristics of the PV arrays, which is enabled by the software tool developed for this purpose. The software tool inputs are the connected PV modules' current-voltage (I-V) characteristics, obtained through simulation or measurement and the connection topology. The outputs are a PV array's I-V and corresponding power-voltage (P-V) characteristics.

#### Findings:

The P-V characteristics of PV arrays under non-uniform environmental conditions have multiple local maxima. The operation and performance of maximum power point tracking (MPPT) algorithms are evaluated using such characteristics generated with the software tool, showing that multiple local maxima can mislead the MPPT algorithm. Output current distortion during the MPPT process is also measured, revealing changes in the output current spectrum.

#### Originality/value:

This manuscript describes a unique software tool for generating I-V characteristics for emulating PV arrays. The manuscript's value is reflected in the method's applicability and versatility.

#### **Keywords:**

Current-voltage (I-V) characteristic, Photovoltaic (PV) array, PV inverter, PV module, Power-voltage (P-V) characteristic

### Electrical anisotropy of fascicles in a realistic neck model for phrenic nerve stimulation

Wegert Laureen (1), Ziolkowski Marek (1), Hunold Alexander (1, 2), Lange Irene (1), Kalla Tim (1), Haueisen Jens (1)

(1) BMTI, Technische Universität Ilmenau, Ilmenau, Germany (2) neuroConn GmbH, Ilmenau, Germany

#### Purpose:

The purpose of the paper is to analyze and compare a novel three-stage macromeso-micro (M3) modeling framework for simulating phrenic nerve stimulation. This stimulation might be used to improve ventilation in intensive care unit patients. The focus is on a detailed finite element analysis of the first two M3 steps using a realistic neck model.

#### Design/methodology/approach:

A finite element method for stationary electric current flow was used to compute extracellular electric potential distributions along intra-fascicular pathways of the phrenic nerve, essential for nerve activation prediction. A 14-tissue, electrically isotropic realistic neck model was used in the first stage (macro model). Subsequently, in the meso stage, a geometric phrenic nerve model with three electrically anisotropic fascicles representing bundles of axon fibers was analyzed. In this step, the electric potential values calculated in the macro stage were used to define Dirichlet boundary conditions on the nerve surface. The pathways along which the extracellular electric potential was calculated run centrally within the fascicles. To assess the accuracy of the extracellular electric potential calculations, a full macro model including electrically anisotropic fascicles was additionally developed. The potential values calculated based on this model are used for validation and error calculations.

#### Findings:

The results demonstrate changes in the courses of the extracellular electric potential with implemented anisotropic electrical conductivity. Specifically, these changes are larger at the boundaries of the fascicles compared to the center of the fascicles. The use of separate macro- and meso-geometric models can significantly increase computation time. Therefore, it is recommended to use (if computational resources allow) only one, full macro-geometric model that accounts for the electrical anisotropy of fascicles.

#### Originality/value:

Development and comparison of modeling approaches for simulating phrenic nerve stimulation.

#### **Keywords:**

Anisotropy, Electric fields, Finite element analysis, Bioelectromagnetics, Material modeling

### Index of Authors

В	Lytvynenko Victoria V	.0
Baida Yevhen I	•	
Bakondi Tamás56	M	
Barmada Sami	Merkel Melina	
Benkő Péter Tamás	Messaoudene Bouchra	
Berkas Kaouter	Moschik Sonja6	
Bilicz Sándor56	Muetze Annette	
Bretterklieber Thomas	Mušeljić Eniz45, 5	ıU
Brignone Massimo59	N	
С	Nagayama Taisuke 6	32
Chepeliuk Oleksandr O	Neumayer Markus	
Clemens Markus	Nicora Martino	
Cvetkovic Nenad	THOOLG MAD UNIO	,,,
Cvetkovic Neliau4	Р	
D	Pantelyat Michael G	0
Dhakal Pawan Kumar50	Petronijević Milutin6	
Dimitrijević Marko	Procopio Renato 5	
Dodge Shayan59	•	
	R	
F	Reichelt Michael5	
Ferkha Nassira	Reichhartinger Markus6	
Fox Colin	Reinbacher-Köstinger Alice	0
Friedl Katrin	C	
<b>C</b>	S	
G	Sasaki Hidenori	
Gschwentner Andreas	Schmidt Erich	
Gyimóthy Szabolcs	Schwartze Nicolai	
Н	Schöbinger Markus	
Hanser Valentin	Schöps Sebastian	
Haueisen Jens	Schürhuber Robert	
Heidarikani Kourosh50	Sedira Dounia	
Hollaus Karl	Steinbach Olaf	
Hunold Alexander	Suppan Thomas6	ìΤ
Transia Trickandor	Т	
J	Tucci Mauro 5	59
Jauk Benjamin	14001 114410	
Jovanovic Dejan4	U	
	Ulbrich Stefan5	60
K		
Kalla Tim	V	
Kaltenbacher Manfred	Vuckovic Dragan	4
Kenderes Anett	<b>\ \ \ \ \</b>	
Komann Theodor 50	W	
L	Wegert Laureen	
Lackner David A	Wegleiter Hannes6	ıΤ
Large Irene	Z	
o contract of the contract of	Ziolkowski Marek6	:=
Leliuk Mykola A		
Leumüller Michael58	Zivaljevic Dragana	4